Two-dimensional quasi-static delamination in composite laminates under Mode-I and Mode-II conditions

Congzhe WANG

To my parents

Preface

Fiber-polymer composite materials may offer significant advantages over traditional materials in bridge and building construction and therefore are experiencing an increasing use. In their design, delamination in laminates or debonding of face sheets from the core in sandwich structures represent some of the most critical failure modes, which may affect the structural integrity and safety. Delamination and debonding normally start at small defects or imperfections and then may propagate in all directions in a two-dimensional (2D) way. However, delamination and debonding are today investigated and characterized by standardized one-dimensional (1D) fracture mechanics, which does not capture potential 2D effects. After a PhD first thesis, which investigated the (opening) Mode I 2D effects during 2D delamination in laminates and 2D debonding of face sheets, this thesis focuses on (shear) Mode II 2D effects during 2D delamination in laminates. Original 2D experimental set-ups and non-linear numerical models were developed and applied to quantify these 2D effects. The results demonstrate clear differences to the 1D behavior in cases where significant microcracking and fiber bridging occurs.

Lausanne, October 2023

Prof. Dr. Thomas Keller
EPFL-CCLab

Acknowledgements

This thesis marks the culmination of my remarkable four-year journey at CCLab, EPFL, an experience comprising fair share of challenges and triumphs. Throughout these years, the world underwent significant changes, largely influenced by the COVID-19 pandemic, which accompanied the majority of my doctoral study. However, alongside these challenges were countless moments of joy and exhilarating achievements. I consider myself immensely fortunate to have crossed paths with so many extraordinary and kind-hearted people, without whose encouragement and support, I would not have come this far.

Firstly, I would like to express my sincere gratitude to my supervisor, Prof. Thomas Keller, for offering me this invaluable opportunity to pursue a PhD, and for his unwavering support and guidance throughout. Prof. Keller's dedication to research and engineering, coupled with his great wisdom and keen scientific insight, has been an inspiration. Under his guidance, CCLab became an exceptional laboratory with a warm and diligent atmosphere. I must also express my deep appreciation to my co-supervisor, Prof. Anastasios Vassilopoulos, for all those fruitful discussions both within and outside the meetings, and tireless revision of my papers. His insightful suggestions, along with his humor, helped me a lot through my challenging times. I deeply value not only their scientific expertise but also the professional attitudes that I will carry with me throughout my future career.

I would also like to extend my gratitude to the members of the thesis defense committee: who chaired the examination, and Prof. John Botsis, Dr. Andreas Brunner, and Prof. Bent F. Sørensen for dedicating their time and effort to evaluate my thesis and for their invaluable comments. Their involvement in my defense deeply honored me. I must also offer my heartfelt thanks for the unique gift from Dr. Brunner after the oral exam – a special cup glazed with my name, such an honor that few PhD students have the privilege of receiving.

My research involved considerable experimental work, which would not have been possible without the hardworking and patient support of the Structural Engineering Platform (GIS) technician team. I express my sincere gratitude to Gilles for his exceptional program management, his tireless responsiveness to my inquiries, and his ability to swiftly address unexpected issues during experiments; Serge and Luca

provided important assistance in the experimental setups, often making tireless adjustments and clever improvements; Armin and Frédérique executed extensive cutting and machining tasks with precision, even under tight schedules. Special mention also goes to Gérald and François, with whom I did not have many opportunities to work closely, but they were always ready to help.

Studying and working at EPFL was an extremely pleasant experience, allowing me to build friendships with so many lovely and talented people. I'd like to express my heartfelt appreciation to my current and former colleagues at CCLab: Dr. Lulu Liu, who was always my go-to person whenever I encountered difficulties, and her continuous support, in both work and life, left an indelible mark (I vividly recall her warm welcome and guidance on my very first day at EPFL); Dr. Niloufar Vahedi, my energetic officemate, with whom I enjoyed countless engaging discussions; Dr. Ghazaleh Eslami, our "class monitor", who shared her delightful homemade treats with us; Dharun Srinivasan, a warm-hearted and unselfish friend, who brought much joy to the lab; Tara Habibi, like a big sister to us, always impeccably organized; Dr. Mateus Hofmann, a composed and wise presence who provided me with valuable suggestions; Saira Banu Mohamed-Kanani, our dedicated secretary, who ensured seamless administrative support, allowing me to focus on my research; and Shayan Khalooei, a taciturn talent My gratitude also extends to the visiting students: Dr. Lingfeng Zhang, Dr. Yuntong Du, Dr. Shengchen Du, Dr. Ting Li, Guangjian Xiang, Dr. Gisele Góes Cintra, Dr. Viviana Jacqueline Castro Quispe, Dr. Geovane Santos Almeida, Yun Sun, Changyuan Liu and Aloys Dushimimana. A special thank you to Dr. Haifeng Fan, who helped me significantly with my application for this PhD position and during my stay in Switzerland. You all made CCLab feel like home, and I will always cherish the laughter we shared. I extend my best wishes for your continued success in your careers.

I must also express my deep appreciation to Prof. Yu Bai, who is akin to a "legend" among us newer members of CCLab. His remarkable research achievements during his PhD, and even more so in his subsequent academic career, have been a true inspiration. I was so lucky to have shared an office with him for six months during his visit to EPFL in the final year of my doctoral study. He generously imparted a wealth of invaluable scientific insights and experiences that undoubtedly contributed to his remarkable academic success.

I'm grateful to my board-game and hiking companions: Jian Zhan, Xianlin Wang, Dr. He Ji, Dr. Zhiyu Li, Dr. Meng Lin, Dr. Qianhui Yu, Qianqing Wang, Mingxiang Gao,

Jialiang Fan, Dr. Chengmin Li, Dr. Chaoqun Dong, Dr. Xiaotong Du, Dr. Zhiwen Jiang, Wanting Jin, Dr. Haoran Shi, Lixin Yang, Chen Zhang, Ce Wen, Mengyi Wang and Xinling Li. Your companionship added color and joy to my life in Switzerland, making it a truly beautiful experience.

Last, but certainly not least, I want to convey my profound gratitude to my parents. The past four years have been really difficult for them, since I, their only child, could not go back home for even once due to the challenges posed by both the COVID-19 situation and the research difficulties that arose at inopportune times. I can't thank them enough for their boundless love and unwavering support from the day I was born.

Thanks again to all the individuals I've crossed paths with, even if not all of them are mentioned here. A new adventure lies ahead, and I eagerly anticipate what it holds.

Abstract

Fiber-polymer composites consist of a polymer matrix and reinforcing fibers made of various materials. These composites exhibit exceptional properties, such as a high strength-to-weight ratio and excellent corrosion resistance, which has led to their increasing use in diverse engineering fields. Typically featuring a layered structure, they demonstrate different failure modes compared to conventional construction materials like concrete and metals. In particular, the weaker properties in the thickness direction make them prone to the separation between layers, i.e., delamination. The study of delamination failure has been a focal point for researchers in the past decades, prompting the establishment of several test standards to assess the material's resistance to delamination. These tests typically involve one-dimensional (1D) beam specimens with a pre-crack subjected to specific fracture mode or mixed mode conditions. While these approaches are valuable for analysis due to the relative simplicity in the test set-up and the stress state of the specimen, they do not capture the actual delamination behavior of cracks embedded in laminates, which tend to propagate in multiple directions with varying contours. To investigate the delamination fracture behavior of laminates in a more realistic context and uncover potential two-dimensional (2D) effects, in this research, the 2D delamination growth is investigated and compared with traditional 1D fracture tests.

Under the context of Mode-I fracture conditions, previous experiments have preliminarily attributed the main differences between 2D and 1D delamination behaviors to the increasing crack-front length and the membrane forces (stretching) occurring during large plate-deformation. Based on these experimental results, a numerical investigation of the 2D delamination growth was conducted using the cohesive zone method (CZM), exploring the influences of a variety of parameters including the pre-crack shape/area, loading-zone shape/area and fracture resistance.

In the case of 2D Mode-II delamination, experimental investigations were conducted on two groups of plate specimens with central pre-cracks of different sizes. The specimens were subjected to transverse loading and semi-clamped along the edge, allowing in-plane sliding while constraining rotation and out-of-plane movement along the edge. An increase in the crack propagation rate occurred, while the load continued to increase until flexural failure. Under post-inspection with a digital microscope, a long

fracture process zone, including large-scale fiber bridging and hackles reflecting microcracks, was observed.

To further investigate the 2D effects on the fracture mechanisms in the Mode-II experiments, a novel cohesive model, considering both the microcracking and fiber bridging, was employed for finite element analysis (FEA). Although the maximum SERR was similar in 2D and end-loaded split (ELS) experiments, the mean traction stresses over the microcracking zone were notably lower in 2D delamination due to the overall tensile membrane forces induced by large deformation. Practical methods for locating the crack tip of an embedded crack based on surface measurements, such as the curvature and strains, were proposed.

Keywords: two-dimensional delamination, fracture, crack propagation, cohesive zone method, fiber bridging, microcrack, finite element analysis, membrane stress, laminate, fiber-polymer composite.

Résumé

Les composites fibres-polymères se composent d'une matrice polymère et de fibres de renforcement fabriquées à partir de divers matériaux. Ces composites présentent des propriétés exceptionnelles, telles qu'un rapport élevé résistance-poids et une excellente résistance à la corrosion, ce qui a conduit à leur utilisation croissante dans divers domaines de l'ingénierie. Typiquement dotés d'une structure en couches, ils présentent différents modes de défaillance par rapport aux matériaux de construction conventionnels tels que le béton et les métaux. En particulier, les propriétés plus faibles dans la direction de l'épaisseur les rendent sensibles à la séparation entre les couches, c'est-à-dire la délamination. L'étude de la défaillance par délamination a été un point central pour les chercheurs au cours des dernières décennies, ce qui a conduit à l'établissement de plusieurs normes d'essai pour évaluer la résistance du matériau à la délamination. Ces tests impliquent généralement des spécimens de poutre unidimensionnels (1D) avec une pré-fissure soumise à des conditions de mode de fracture spécifiques ou mixtes. Bien que ces approches soient précieuses pour l'analyse en raison de la simplicité relative de la configuration de l'essai et de l'état de contrainte du spécimen, elles ne capturent pas le comportement réel de délamination des fissures incorporées dans les stratifiés, qui ont tendance à se propager dans des directions multiples avec des contours variables. Pour étudier le comportement de rupture par délamination des stratifiés dans un contexte plus réaliste et découvrir d'éventuels effets bidimensionnels (2D), dans cette recherche, la croissance de délamination en 2D est étudiée et comparée aux tests de rupture traditionnels en 1D.

Dans le contexte des conditions de rupture de Mode-I, des expériences précédentes ont attribué préliminairement les principales différences entre les comportements de délamination en 2D et 1D à l'augmentation de la longueur du front de fissure et aux forces membranaires (étirement) se produisant pendant une grande déformation de la plaque. Sur la base de ces résultats expérimentaux, une enquête numérique sur la croissance de la délamination 2D a été réalisée en utilisant la méthode de zone cohésive (CZM), explorant l'influence de divers paramètres, notamment la forme/aire de la pré-fissure, la forme/aire de la zone de chargement et la résistance à la rupture.

Dans le cas de la délamination 2D en Mode-II, des enquêtes expérimentales ont été menées sur deux groupes des spécimens de plaques avec des pré-fissures centrales

de différentes tailles. Les échantillons ont été soumis à une charge transversale et semi-serrés le long du bord, permettant un glissement dans le plan tout en contrôlant la rotation et le mouvement hors du plan le long du bord. Une augmentation de la vitesse de propagation de la fissure s'est produite, tandis que la charge continuait d'augmenter jusqu'à la rupture par flexion. Lors d'une inspection ultérieure au microscope numérique, une longue zone de processus de rupture, comprenant un pontage des fibres à grande échelle et des hackles reflétant des microfissures, a été observée.

Pour approfondir l'étude des effets 2D sur les mécanismes de rupture dans les expériences en Mode-II, un nouveau modèle cohésif, tenant compte à la fois de la microfissuration et le pontage des fibres, a été utilisé pour l'analyse par éléments finis (FEA). Bien que le SERR maximum était similaire dans les expériences 2D et les expériences de flexion à extrémité chargée (ELS), les contraintes de traction moyennes sur la zone de microfissuration étaient nettement plus faibles dans la délamination 2D en raison des forces membranaires globales de traction induites par la grande déformation. Des méthodes pratiques pour localiser la pointe d'une fissure incorporée basée sur des mesures de surface, telles que la courbure et les déformations, ont été proposées.

Mots clés: délamination bidimensionnelle, rupture, propagation de fissure, méthode de zone cohésive, pontage des fibres, microfissure, analyse par éléments finis, contrainte membranaire, stratifié, composite fibre-polymère.

摘要

纤维增强复合材料由聚合物基体及增强纤维组成。这类复合材料具有轻质高强、耐腐蚀等优异的性能，在各类工程领域中得到越来越广泛的应用。与传统建筑材料如混凝土和钢相比，此类复合材料因其层合结构的特点，通常表现出不同的破坏模态，即在性能较弱的厚度方向上发生分层（delamination）。过去几十年来，分层破坏已成为复合材料领域的研究热点，多个层间断裂韧性试验方法相继建立。这类试验通常采用带有预制裂纹的一维（1D）梁试件，在特定断裂模式或混合型断裂模式下加载。此类试验方法设置简单、试件受力清晰，因而便于分析，但是无法表现一般情况下层合板中内嵌裂纹的真实断裂情况，即通常以不断变化的轮廓向多个方向扩展。为了研究复合材料层合板更为真实的分层断裂行为，并揭示潜在的二维（2D）效应，本文研究了 2D 分层扩展，并与 1D 分层断裂试验进行对比。

在 I 型断裂背景下，现有试验研究初步将 2D 分层行为与 1D 分层的差异归因于持续增加的裂纹周长以及板壳大变形导致的薄膜力。基于该试验结果，使用内聚力模型（cohesive zone method, CZM），开展了 2D 分层扩展的数值研究，分析了预制裂纹形状、面积，加装区形状、面积以及断裂韧性等参数的影响。

对于 II 型分层断裂，首先开展了试验研究，设置了两组圆板型试件，内嵌不同大小的中心预制裂纹。试件采用横向力加载，并沿边缘半固定于特制夹具，以限制试件外侧的转动与面外移动，同时允许面内滑动。试验中裂纹扩展速率有所提高，但荷载持续增加，最终发生弯曲破坏。试验后通过显微镜观察发现了较长的断裂过程区（fracture process zone, FPZ），其中包含大规模纤维桥接，以及反应了微裂纹的锯齿形断面。

为进一步研究 II 型分层试验中 2D 效应对断裂机理的影响，考虑微裂纹和纤维桥接的作用，提出了新型内聚力模型，并开展有限元分析。与端部加载劈裂（end-loaded split, ELS）试验结果相比，2D 分层表现出相似的最大能量释放率，但其微裂纹区的平均牵引应力却显著降低，这是由大变形产生的薄膜力导

致的。综合研究成果，提出了基于曲率或应变等表面测量结果定位内嵌裂纹端部的实用方法。

关键词： 2D 分层，断裂，裂纹扩展，CZM，纤维桥接，微裂纹，有限元分析，薄膜力，层合板，纤维/聚合物复合材料。

Table of Contents

List of Figures

Chapter 3 | Mode-II delamination: experimental investigation

Chapter 4 | Mode-II delamination: numerical investigation

Chapter 5 | Conclusions and future work

List of Tables

Chapter 1

Introduction

1.1 Context and motivation

A composite material is composed of two or more constituent materials on a macro-scale, offering an opportunity to harness the best qualities from each component and often resulting in enhanced performance. The historical use of manmade composite materials can be traced back over ten thousand years, where straw-reinforced mudbricks were utilized in construction [1]. In contemporary times, modern composite materials often refer to fiber-polymer composites, which involve arranging fibers in flat configurations within polymer matrices, stacked in multiple layers to form laminated structures. The inception of fiber-polymer composites dates to the early 20th century [2]. Since then, these materials have undergone significant evolution, witnessing the emergence of diverse fiber and matrix types, along with the development of advanced manufacturing techniques. Their outstanding properties, including high strength, stiffness, lightweight nature, and exceptional durability, have positioned them for manufacturing structural components in various sectors such as aerospace, automotive, marine, etc. Of particular note is the growing interest in applying composite materials to civil engineering, leveraging benefits like the potential for prefabrication with quality control, reduced traffic downtime from swift on-site assembly, and decreased maintenance requirements [3,4]. A market report predicts that the glass-fiber composite market alone will expand to a value of 61.3 billion dollars by 2028, with transportation and construction representing major sectors [5].

Across Europe, a multitude of structures have experienced the advantages of composite materials over the past decades, particularly in bridge and building applications [6]. For example, the Ooypoort pedestrian bridge (Fig. 1.1a), opened in 2014 in Nijmegen, Netherlands, was assembled on-site by joining three glass-fiber composite segments, reaching a span of 56 meters while maintaining a slender profile [7]. The remarkable durability of composite materials even permits partial submersion of the bridge during extreme water levels. In 2013, the Pont y Ddraig (the Dragon Bridge, Fig. 1.1b), also known as the Rhyl Harbour Lifting Bridge, was unveiled in Northern Wales, UK. This structure features two spans, each measuring 32 meters,

composed of hybrid glass-fiber and carbon-fiber composites, which significantly reduced energy consumption during lifting cycles [8]. The old one-lane concrete Avançon bridge in Bex, Switzerland was replaced in 2012 by a new two-lane bridge. The replacement utilized a composite sandwich deck adhesively bonded onto steel girders (Fig. 1.1c), without introducing additional loads on the old brick abutments [9,10]. Additional benefits of employing composites included notably reduced bridge closure time. The entrance building at the Novartis Campus (Fig. 1.1d), completed in 2006 in Basel, Switzerland, is covered by a sandwich roof featuring glass-fiber-laminate face sheets. The composite roof integrated structural, building physical and architectural functions while maintaining a light weight, allowing it to be supported solely by the glass facades [11].

Fig. 1.1 Examples of composite constructions: (a) Ooypoort pedestrian bridge [12], (b) Pont y Ddraig [8], (c) Avançon bridge [9] and (d) Novartis Campus entrance building [11].

Composites diverge in behavior from traditional construction materials like concrete and steel due to their laminated structure. Consequently, these materials necessitate distinct fabrication, design, and inspection methods [13]. As a result,

realizing structures in the past generally required additional workload from experiments or calculations due to missing codes and standards [14]. In 2022, following extensive research outcomes and application experiences, Europe finally witnessed the publication of the Technical Specification "Design of fibre-polymer composite structures" [15], which is expected to become a European Standard in two years. This development will certainly contribute to the guidance on future designs and further promote composite constructions.

Harnessing the advantages of composite materials depends on comprehending potential failure modes. One common failure mechanism in composite laminates is delamination, often arising from the relatively lower properties in the thickness direction [16–18]. Delamination can originate from various sources, such as structural discontinuities, manufacturing defects, impact and fatigue loads, moisture, UV radiation, etc. [19]. For damage-tolerant design, a certain extent of stable crack propagation is permissible [15,20], to make full use of the increasing fracture resistance that is reflected in the R-curves of most fiber-polymer composites. Therefore, understanding delamination growth in composite laminates is crucial to ensure their structural integrity.

Once initiated, delamination can grow through various fracture modes within the laminates. For instance, during local buckling, delamination growth may occur under Mode-I (dominant) fracture [21], while during global buckling or bending, Mode II or Mode III may dominate [22]. Although delamination in real structures often involves mixed-mode fracture due to the complex stress state, investigating pure fracture modes remains important for laying the foundation of fracture behavior comprehension.

Over the recent decades, extensive research, e.g., Ref. [23–26], has explored the quasi-static delamination behavior in composite materials using standardized test methods, such as the double cantilever beam test for Mode-I fracture [27], and the end-loaded split test for Mode-II fracture [28]. While the utilization of beam specimens in such tests simplifies the complex stress and fracture conditions present in real structures by confining the crack to propagate in one dimension, such simplification may not be appropriate under some circumstances. In fact, most actual delamination scenarios involve cracks embedded within laminates, propagating in multiple directions and presenting a two-dimensional (2D) pattern. Overlooking this aspect can lead to significant errors in estimating the fracture properties [29]. This topic was addressed in a series of studies conducted by Cameselle-Molares et. al [29–33], who investigated the

two-dimensional (2D) Mode-I crack propagation in composite laminates and sandwich panels by opening an embedded pre-crack in plate specimens. Their findings demonstrated that tensile membrane stresses in the laminates, induced during large deflection, can enhance fiber bridging, resulting in higher fracture resistance.

The aforementioned studies [29–33] focused on the symmetric growth of a circular pre-crack under Mode-I fracture condition. Considering the generality, it is imperative to further explore the influence of different pre-crack and loading-zone configurations on 2D fracture behavior and structural response. Moreover, the differences between 1D and 2D delamination growth under Mode-II fracture conditions remain unclear.

1.2 Objectives

This thesis aims to explore the 2D delamination growth in composite laminates under pure Mode-I and Mode-II fracture conditions. Previous works [29–33] have been analyzed and extended to identify the influence of several important factors on the 2D Mode-I delamination growth. Subsequently, the experimental concepts and numerical methods are adapted and employed for investigating the behavior of 2D Mode-II delamination.

The specific objectives are outlined as follows:

1. Numerical investigation of the influences of pre-crack shape/size, loading-zone shape/size and fracture resistance on 2D delamination behavior and structural response under Mode-I fracture conditions based on previous experimental results.

2. Experimental investigation of the 2D delamination growth under Mode-II fracture condition to identify the similarities and differences with the 1D growth in standardized beam specimens.

3. Numerical investigation of the 1D and 2D Mode-II delamination behavior to estimate the strain energy release rates (SERRs, referring to the work of cohesive traction for consistency with previous publications) and to understand the mechanisms causing the differences between the 1D and 2D cases.

4. Development of practical approaches to locate the embedded crack front through surface measurements.

1.3 Methodology

The methodology used to achieve the objectives described above consists of both experimental and numerical investigations, covering a variety of topics, which are listed as follows:

1.a Establishment of numerical models capable of replicating experimental observations and amenable to parametric investigation under 2D Mode-I fracture condition.

1.b Parametric analysis of the influences of pre-crack shape/size, loading-zone shape/size and fracture resistance on the 2D Mode-I delamination behavior and structural response.

2.a Development of a novel experimental set-up to examine 2D delamination growth in composite plate-specimens under Mode-II fracture condition in the presence of a large-scale fracture process zone.

2.b Comparison of the results from 2D Mode-II experiments with those from 1D experiments using an end-loaded split test set-up.

3.a Development of cohesive models using a semi-experimental approach to explain different mechanisms along the fracture process zone in Mode-II delamination.

3.b Numerial simulation of the experimentally observed 1D and 2D Mode-II delamination behavior, pinpointing the principal mechanisms contributing to the differences between the 1D and 2D cases.

4. Analysis of the curvature and strain results on the plate surface from both experimental and numerical data to determine the location of the embedded crack tip.

1.4 Thesis organization

The thesis encompasses three core chapters that align with the established objectives discussed in Section 1.2. A subsequent chapter summarizes the conclusions drawn from the research and suggests potential future avenues of exploration. The main content of each chapter is summarized as follows:

- Chapter 1: The context and motivation of this research are introduced, followed by a brief explanation of the objectives and methodology.

- Chapter 2: The 2D Mode-I delamination growth in composite laminates is numerically investigated. This chapter features the development of three distinct model types tailored for simulating previous experiments and enabling subsequent parametric studies. The influences of the pre-crack shape/area, the loading-zone shape/area and the fracture resistance on the 2D delamination growth are analyzed, covering the crack initiation, early propagation and steady-state propagation stages.

- Chapter 3: The 2D Mode-II delamination growth in composite laminates is experimentally investigated using a novel set-up. Two sizes of pre-cracks embedded in plate specimens are involved. For comparison, 1D experiments are performed on end-loaded split specimens. After loading, both types of specimens are subjected to microscopic inspection to unravel the mechanisms acting within the fracture process zone.

- Chapter 4: The 1D and 2D Mode-II delamination growth in composite laminates is numerically investigated. New cohesive laws are developed using a semi-experimental approach to describe different fracture mechanisms observed in the experiments. The cohesive parameters are obtained using an iterative fitting process, enabling the derivation of SERRs. The chapter also presents practical methods for locating the embedded crack front based on surface curvature and strain measurements, validated by both experimental and numerical results.

- Chapter 5: A summary of the main conclusions drawn from the conducted research is provided, followed by suggestions of potential future research directions.

The general structure of the main chapters in this thesis is outlined in Table 1.1. The results of this thesis have been published in three journal papers (two accepted, one in review), corresponding to chapters 2-4 (see Table 1.1):

1. Wang C, Vassilopoulos AP, Keller T. Numerical modeling of two-dimensional delamination growth in composite laminates with in-plane isotropy. Engineering Fracture Mechanics. 2021; 250:107787.

2. Wang C, Vassilopoulos AP, Keller T. Experimental investigation of two-dimensional Mode-II delamination in composite laminates. Composites Part A: Applied Science and Manufacturing. 2023; 173:107666.

3. Wang C, Vassilopoulos AP, Keller T. Numerical investigation of two-dimensional Mode-II delamination in composite laminates. (*submitted in August 2023*)

Table 1.1. General organization of thesis main chapters.

Fracture mode	Dimensions	Methodology	Main chapters	Papers	Appendices
Mode I	2D	• Establishment of numerical models • Parametric studies	2	1	
Mode II	1D and 2D	• Development of new experimental set-up • Experimental investigation of 2D delamination • Experimental investigation of 1D delamination	3	2	A1, A2, A3, A4
		• Development of cohesive laws • Numerical simulations	4	3	B1, B2, B3
	2D	• Determination of embedded crack tip using surface measurements	4	3	

Supplementary information for the thesis is provided in eight appendices:

- Appendix A1: Development of 2D Mode-II experimental set-ups.
- Appendix A2: Supplementary results for 2D Mode-II experiments.
- Appendix A3: Determination of parallax error for 2D Mode-II specimens.
- Appendix A4: Flexural damage process in 2D Mode-II specimens.
- Appendix B1: Constitutive relationships of CFM and MD laminates.
- Appendix B2: Iterative fitting of cohesive parameters.
- Appendix B3: Microscopic microcracking behavior in Mode-II delamination.
- Appendix C: Mode-II delamination in mid-crack beam specimens.

References

[1]   Kuijt, I. Finlayson B. Evidence for food storage and predomestication granaries 11,000 years ago in the Jordan Valley. Proc Natl Acad Sci U S A. 2009;106(27):10966–10970.

[2]   Vassilopoulos AP, Keller T. Fatigue of Fiber-reinforced Composites. Springer; 2011.

[3]   Ascione L, Caron JF, Godonou P, van IJselmuijden K, Knippers J, Mottram T, et al. Prospect for New Guidance in the Design of FRP. EUR 27666. Ispra, Italy; 2016.

[4]   Keller T, Schaumann E, Vallée T. Flexural behavior of a hybrid FRP and lightweight concrete sandwich bridge deck. Compos Part A Appl Sci Manuf. 2007;38(3):879–89.

[5]   ReportLinker. GFRP Market Trends and Forecast. https://www.globenewswire.com/news-release/2023/04/27/2656099/0/en/GFRP-Market-Trends-and-ForecastThe-global-GFRP-market-is-expected-to-reach-an-estimated-61-3-million-by-2028-with-a-CAGR-of-3-7-from-2022-to-2028.html (accessed August 6, 2023).

[6]   Keller T, Theodorou NA, Vassilopoulos AP, de Castro J. Effect of Natural Weathering on Durability of Pultruded Glass Fiber–Reinforced Bridge and Building Structures. Journal of Composites for Construction. 2016;20(1):1–9.

[7]   Kendall D. Next generation footbridges in FRP composites. In: Footbridge 2014-Past, Present & Future. London, UK; p. 75–85.

[8]   Royle T. Composites meet Welsh harbour needs. Reinforced Plastics. 2014;58(1):34–8.

[9]   Osei-Antwi M, De Castro J, Vassilopoulos AP, Keller T. FRP-balsa composite sandwich bridge deck with complex core assembly. Journal of Composites for Construction. 2013;17(6):1–9.

[10]   Keller T, Rothe J, De Castro J, Osei-Antwi M. GFRP-balsa sandwich bridge deck: Concept, design, and experimental validation. Journal of Composites for Construction. 2014;18(2):1–10.

[11]   Keller T, Haas C, Vallée T. Structural Concept, Design, and Experimental Verification of a Glass Fiber-Reinforced Polymer Sandwich Roof Structure. Journal of Composites for Construction. 2008;12(4):454–68.

[12]   Janberg N. Ooypoort Footbridge. 2015. https://structurae.net/en/media/237441-ooypoort-footbridge (accessed August 7, 2023).

[13]   Robinson P, Greenhalgh E, Pinho S, editors. Failure mechanisms in polymer matrix composites: Criteria, testing and industrial applications. Cambridge: Woodhead Publishing Limited; 2012.

[14]   Ellingwood BR. Toward Load and Resistance Factor Design for Fiber-Reinforced Polymer Composite Structures. Journal of Structural Engineering. 2003;129(4):449–58.

[15]   CEN/TS 19101:2022. Design of Fibre-Polymer Composite Structures. In: European Committee for Standardization. Brussels; 2022.

[16]   Davies P, Casari P, Carlsson LA. Influence of fibre volume fraction on mode II interlaminar fracture toughness of glass/epoxy using the 4ENF specimen. Compos Sci Technol. 2005;65(2):295–300.

[17]   Toftegaard HL, Sørensen BF. General J integral solution for specimens loaded by moments, axial forces and residual stresses – A unifying stiffness formulation. Eng Fract Mech. 2019;217(July):106500.

[18]   Pappas G, Joncas S, Michaud V, Botsis J. The influence of through-thickness reinforcement geometry and pattern on delamination of fiber-reinforced composites: Part I – Experimental results. Compos Struct. 2018;184:924–34.

[19]   Sridharan S. Delamination Behaviour of Composites. Delamination Behaviour of Composites. 2008. 1–762 p.

[20]   Pascoe JA. Slow-growth damage tolerance for fatigue after impact in FRP composites: Why current research won't get us there. Theoretical and Applied Fracture Mechanics. 2021;116:103127.

[21]   De Cicco D, Taheri F. Delamination Buckling and Crack Propagation Simulations in Fiber-Metal Laminates Using xFEM and Cohesive Elements. Applied Sciences. 2018;8(12):2440.

[22]   Andraju LB, Ramji M, Raju G. Snap-buckling and failure studies on CFRP laminate with an embedded circular delamination under flexural loading. Compos B Eng. 2021;214:108739.

[23]   Brunner AJ. Fracture mechanics testing of fiber-reinforced polymer composites: The effects of the "human factor" on repeatability and reproducibility of test data. Eng Fract Mech. 2022;264:108340.

[24]   Frossard G, Cugnoni J, Gmür T, Botsis J. Mode I interlaminar fracture of carbon epoxy laminates: Effects of ply thickness. Compos Part A Appl Sci Manuf. 2016;91:1–8.

[25]   Blackman BRK, Kinloch AJ, Paraschi M. The determination of the mode II adhesive fracture resistance, GIIC, of structural adhesive joints: An effective crack length approach. Eng Fract Mech. 2005;72:877–97.

[26]   Hashemi S, Kinloch AJ, Williams JG. The Effects of Geometry, Rate and Temperature on the Mode I, Mode II and Mixed-Mode I/II Interlaminar Fracture of Carbon-Fibre/Poly(ether-ether ketone) Composites. J Compos Mater. 1990;24(9):918–56.

[27]   ISO 15024:2001. Fibre-reinforced plastic composites — Determination of mode I interlaminar fracture toughness, Gic, for unidirectionally reinforced materials. 2001.

[28]   ISO 15114:2014. Fibre-reinforced plastic composites — Determination of the mode II fracture resistance for unidirectionally reinforced materials using the calibrated end-loaded split (C-ELS) test and an effective crack length approach. 2014.

[29]   Cameselle-Molares A, Vassilopoulos AP, Renart J, Turon A, Keller T. Numerical simulation of two-dimensional in-plane crack propagation in FRP laminates. Compos Struct. 2018;200(April):396–407.

[30]   Cameselle-Molares A, Vassilopoulos AP, Keller T. Experimental investigation of two-dimensional delamination in GFRP laminates. Eng Fract Mech. 2018;203:152–71.

[31]   Cameselle-Molares A, Vassilopoulos AP, Renart J, Turon A, Keller T. Numerically-based method for fracture characterization of Mode I-dominated two-dimensional delamination in FRP laminates. Compos Struct. 2019;214:143–52.

[32]   Cameselle-Molares A, Vassilopoulos AP, Keller T. Two-dimensional quasi-static debonding in GFRP/balsa sandwich panels. Compos Struct. 2019;215:391–401.

[33]   Cameselle-Molares A, Vassilopoulos AP, Keller T. Two-dimensional fatigue debonding in GFRP/balsa sandwich panels. Int J Fatigue. 2019;125:72–84.

Chapter 2

Mode-I delamination: parametric investigation

2.1 Introduction

Delamination is one of the most common damage mechanisms in fiber-reinforced polymer (FRP) materials, which can lead to premature structural failure [1,2]. Among the different fracture modes occurring in delamination, Mode I has received most attention, since it necessitates the least energy for crack initiation and propagation [3,4]. As the delamination in FRP materials grows under Mode I loading, fiber bridging develops as a toughening mechanism, differentiating the fracture behavior from that of other materials [5]. In the presence of fiber bridging, cohesive zone modeling (CZM) is regarded as an appropriate method and has been used extensively in finite element (FE) simulations [6–9], due to its ability to embed process zone mechanics through traction-separation relationships across the crack faces, thus separating the fracture process zone (FPZ) ahead of the crack tip from the fiber bridging zone behind the tip.

The vast majority of works on delamination conducted experimental investigations on standardized beam-like specimens [10–13]. The double cantilever beam (DCB) is the most widely used standardized specimen form for Mode I fracture tests on FRP composites. Nevertheless, problems have been encountered in its application during recent years. As shown in [14], the crack front in DCB specimens is curved instead of being straight and perpendicular to the specimens' longitudinal direction, implying non-uniformity of the distribution of the strain energy release rate (SERR), G, across the width and resulting in an underestimation of the fracture resistance by conventional methods [15,16]. In order to obtain a consistent SERR along the crack front, Jiang et al. [14] modified the DCB specimens using a curved pre-crack front determined by a first order optimization method, which however required more effort. Moreover, the total SERR was found to be thickness-dependent in laminated specimens exhibiting large-scale bridging (LSB) [17,18], i.e., it changed with the stiffness of the DCB specimen arms [12]. Pappas and Botsis [19] eliminated the stiffness dependence implied in the conventional cohesive law by substituting the crack opening displacement (COD) with the product of the COD and the crack opening angle, yet the new relationship proposed

is load-type dependent and hence still not a universal method for solving the problem concerned.

Although most of the research was conducted on one-dimensional (1D) beam-like specimens, in reality, the propagation of an embedded crack in most cases is not restricted in one direction but spreads all around its contour, thus producing a 2-dimensional (2D) delamination, with inherent characteristics that cannot be captured by conventional DCB experiments. In a general 2D delamination scenario with a non-circular crack front, the width and curvature of the crack front change continuously with crack propagation. Furthermore, the stiffness of the delaminated region of the laminates gradually increases because of the presence of stretching (in-plane tension stresses due to the boundary conditions of an embedded crack) [20]. As a result, the fracture resistance under 2D crack propagation can be significantly higher than that needed for a 1D crack to propagate in the same material [21,22]. Therefore, it is important to carry out investigations on plate-like specimens that resemble actual fracture scenarios, where cracks propagate in two-dimensions.

Researchers showed particular interest in 2D debond/delamination growth induced by buckling [23–27]. In their analyses however, the critical SERR used was still assumed to be identical to that of the standardized 1D beam-like specimens. If LSB was exhibited, such an assumption may lead to erroneous results. Furthermore, owing to the interaction of local buckling of the laminates above the crack and global buckling of the structural component, the crack tip was under a complex mixed-Mode loading condition, and the fracture behavior for each mode remained unclear. Some research omitted to address this problem and assumed a pure Mode I condition at the crack tip [23,26], which led to a notable deviation between numerical/theoretical results and experimental data. In addition, all the aforementioned research work did not include the effect of fiber bridging. In short, significant differences exist between the research assumptions and actual damage mechanisms in the fracture process of FRP composite structures.

Previously, experimental investigations of the 2D Mode I delamination were conducted on glass fiber-reinforced polymer (GFRP) laminates with different reinforcements [20]. Subsequently, the specimens reinforced by long continuous filament mats (CFMs) were specifically studied in [22,28] due to their in-plane isotropy and ability to exhibit a considerable amount of fiber bridging. The specimens exhibited the same circular-symmetric load and geometrical configuration, resulting in identical

crack propagation in all radial directions. In practice, however, the defect shapes may be random, and the opening forces may not be projected to circular areas. Therefore, the crack propagation may lose the symmetry and instead present a more complex pattern. On the other hand, the numerical model employed in [22] has some limitations in terms of the simplification of the constraints. To the best of the authors' knowledge, no other work has discussed the effect of fiber bridging within the framework of 2D delamination.

The objective of this work was the establishment of an improved numerical approach for 2D delamination analysis and the parametric investigation of the 2D delamination behavior of FRP laminates with different pre-crack and loading zone shapes. For this purpose, the experimental data concerning CFM specimens from [20] were used for the model development. Two sizes of plate models were developed using the commercial finite element analysis (FEA) software ABAQUS 6.14-1 under academic license, each composed of several sub-groups with different pre-crack/loading zone configurations and various fracture resistances. Cohesive elements were employed to simulate the fracture behavior considering the effect of fiber bridging.

2.2 Previous experiments

Similarly to [22], the two CFM specimens described in [20] were selected for the numerical model development in this work, i.e., the experimental load-opening displacement and crack length-opening displacement curves were used for the calibration of the cohesive law. The experimental set-up and results are therefore summarized in the following for clarification purposes.

The two specimens, referred to as CFM1 and CFM2, contained six layers of CFM reinforcement with a laminate thickness of 7.50 mm and 6.99 mm respectively. As shown in Fig. 2.1b, a 13-μm-thick Teflon film with a diameter of 180 mm was placed at the center to create an embedded pre-crack, and a pair of 1.2-mm-thick steel inserts with a diameter of 100 mm, located on the upper and lower sides of the Teflon film, were used to distribute the opening load transferred by a set of steel bolts at the loading line (with a diameter of 70 mm) and a pair of external steel blocks. The experiments were performed under displacement control at a rate of 1.5 mm/min using a W+B electromechanical machine of 50-kN capacity. The load and opening displacement were obtained directly from the machine. The crack front was monitored, thanks to the

transparency of the material, in different directions by three measuring systems, i.e., a 3D Digital Image Correlation System (DIC), a digital camera and visual measurements. In addition, four Linear Variable Differential Transducers (LVDTs) were placed at the plate corners to monitor the corresponding displacements. Full details of the material properties, specimen configuration, infusion process and experimental set-up can be found in [20].
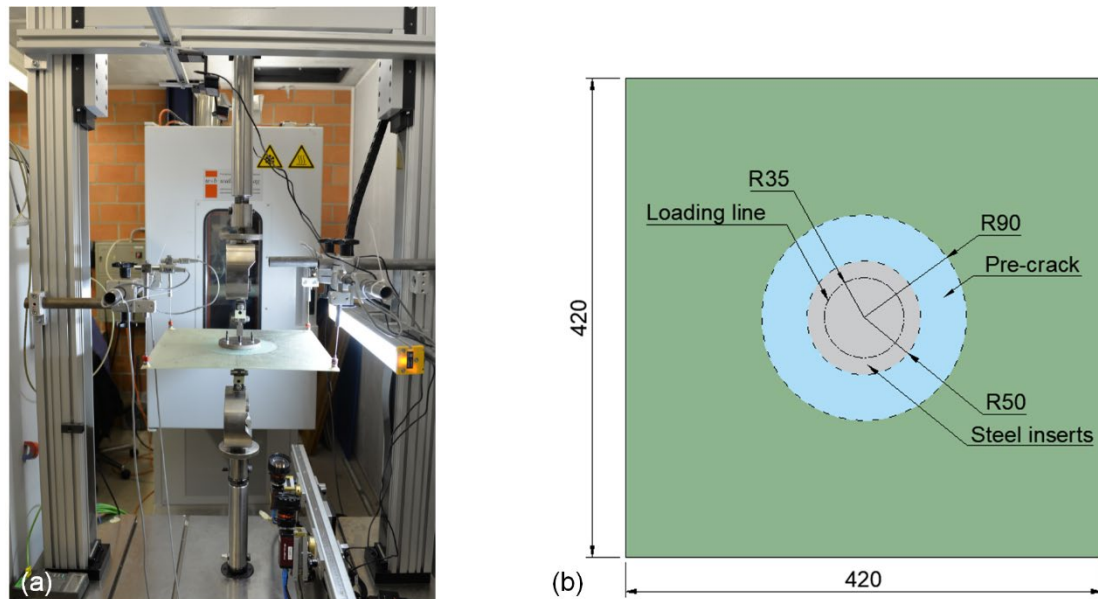
Fig. 2.1. Experimental set-up: (a) overview; (b) specimen configuration (units in mm) [20].
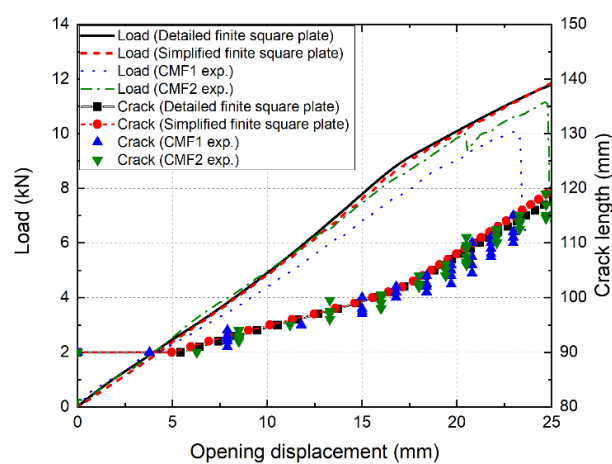
Fig. 2.2. Experimental and numerical load and crack length vs opening displacement curves.

The experimental load-opening displacement curves of CFM1 and CFM2 are presented in Fig. 2.2, along with the points denoting the crack lengths, i.e., the radial distance from the plate center to the crack front. At each recorded displacement level, a total of seven points were obtained in seven directions, see Fig. 2.3. Increasing loads, even after crack initiation, were observed as a result of a continuously increasing crack front width and a consequently disproportionate increase in the propagation area. The crack remained in the mid-plane and propagated in a circular symmetric manner as expected for an in-plane isotropic reinforcement, as shown Fig. 2.3.
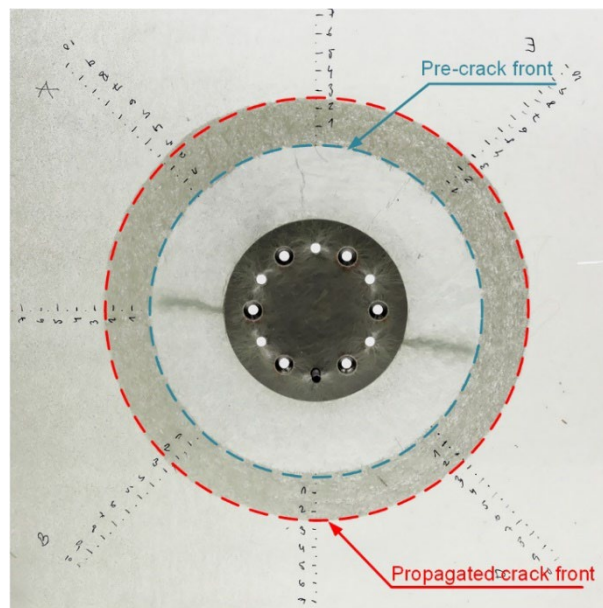
Fig. 2.3. Typical crack propagation pattern (CFM2).

2.3 Numerical models and parameters

Based on the CFM specimens described above, three models were developed successively: the first one, a detailed finite square plate model, intended for the simulation of the experiments and determination of the cohesive law; the second one, a simplified finite square plate model, intended for the investigation of the 2D fracture behavior at the initiation and early propagation stages; and the third one, a simplified semi-infinite circular plate model, intended for the investigation of the 2D fracture behavior after a certain degree of propagation.

2.3.1 Detailed finite square plate model and cohesive law

The detailed finite square plate model is shown in Fig. 2.4a, which had the same dimensions as specimen CFM1 ($420 \times 420 \times 7.5$ mm). In this model, the loading system, i.e., the inserts and bolts, were simulated explicitly. Geometrical nonlinearity was considered to take into account large deformation effects, and the plasticity of the steel inserts was included due to the large plastic deformation observed in the experiments. Considering the symmetry, only one quarter of the plate cut by the diagonal planes was modeled, with symmetric boundary conditions applied accordingly. The external boundary conditions were applied to the bolts, i.e., all degrees of freedom were constrained, as in the experiments. The bolts were modeled as rigid bodies for simplicity, and the contact between the bolts, inserts and laminates was simulated as "hard contact". The laminate was discretized at the cracking plane, i.e., the mid-plane, into two halves, each meshed with three layers of eight-node continuum shell elements with reduced integration (CS8R) for most regions except for the central part, where the insert replaced the innermost layer. Six-node continuum shell elements with reduced integration (CS6R) were used for the inserts and the central part of the laminates in contact with them in order to achieve comparable element size in this fan-shaped region. A single zero-thickness layer of eight-node 3D cohesive elements (COH3D8) was placed at the mid-plane to connect the uncracked region of the plate and simulate the fracture behavior, with a radial dimension of 1 mm in the crack-propagation region and a larger size beyond, which guaranteed a minimum of 10 elements in the cohesive zone length throughout the analysis in order to capture the correct distribution of tractions [29]. In total, the model comprised 55,766 nodes and 48,120 elements. Table 2.1 lists the elastic properties of the laminates, which were derived analytically and then calibrated with experimental data from DCB tests (see [22]). The inserts (stainless steel 304L) were simulated using the Ramberg–Osgood model [30] with material properties taken from [31]. A vertical displacement of up to 25 mm (the approximate experimental ultimate displacement) was applied to the upper bolts to perform the loading process.

Table 2.1. Engineering constants of laminated plates

$E_1 = E_2$	E_3	G_{12}	$G_{23} = G_{31}$	v_{12}	$v_{23} = v_{31}$
8.64 GPa	4.68 GPa	3.25 GPa	1.54 GPa	0.33	0.30
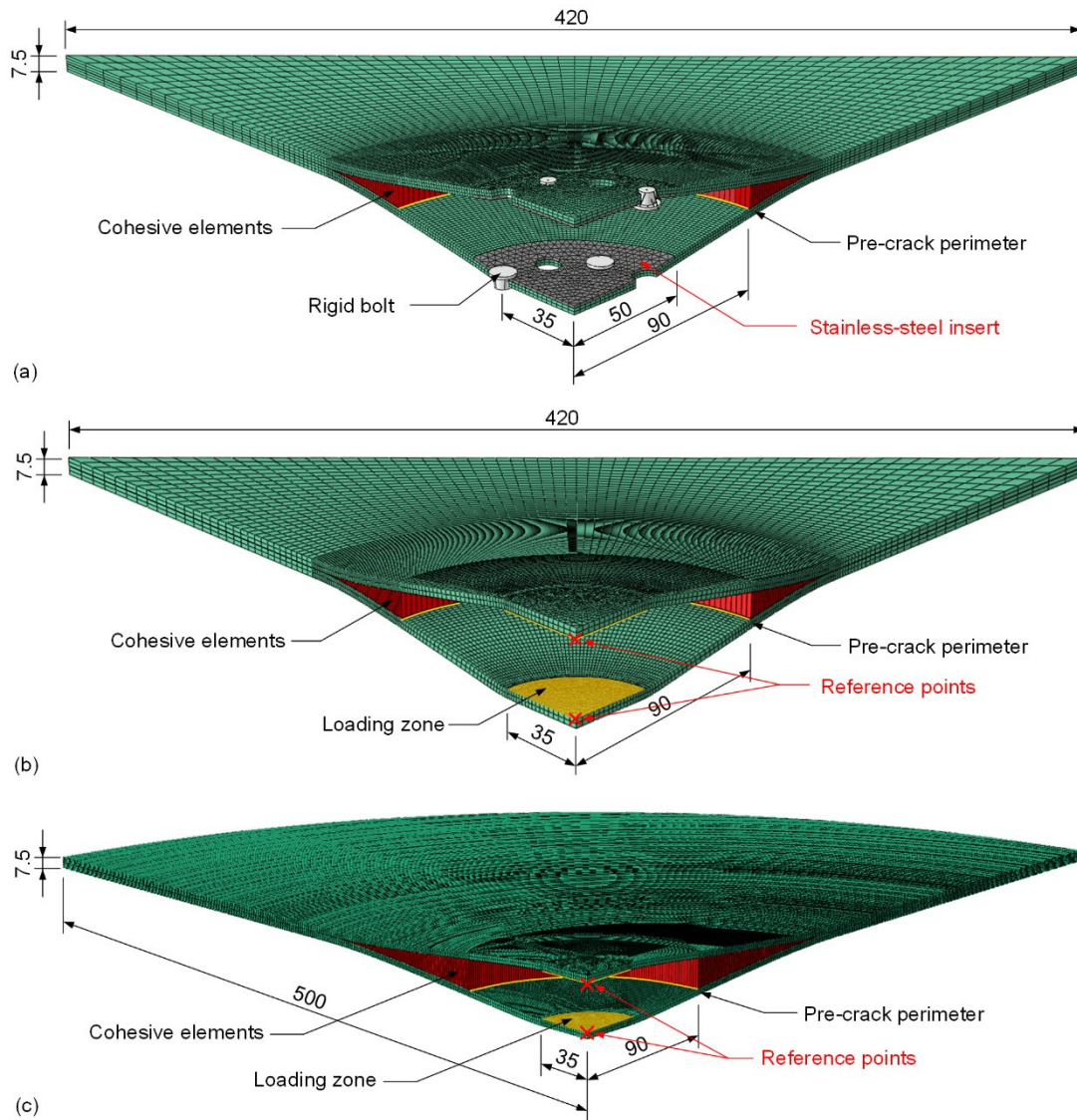
Fig. 2.4. FE models after some deformation with undeformed dimensions: (a) detailed finite square plate model; (b) simplified finite square plate model; (c) simplified semi-infinite circular plate model (units in mm).

A cohesive law that is able to consider LSB, as described in Fig. 2.5 [22,32], was employed by means of a user material subroutine (VUMAT) written in FORTRAN programming language [33]. The softening part can be divided into two segments: (1) the linear softening segment, which corresponds to the small FPZ ahead of the crack tip, and (2) the exponential softening segment, which corresponds to the fiber bridging zone. Accordingly, the total SERR for crack propagation, G_{tot}, can be split into G_{tip}, the SERR at the crack tip (i.e., the SERR required for crack initiation), and G_{br}, the SERR due to fiber bridging, respectively. Among the cohesive parameters, K_0 (the penalty stiffness), σ_c (the interfacial strength), σ_{max} (the maximum bridging traction) and G_{tip}

were taken directly from [22], since the former two serve mainly computational purposes, i.e., saving computational effort and reducing potential error, and the latter two are material properties [6,18,29]. The virtual separation at bridging onset, δ_1, was subsequently derived by using the area relationship between G_{tip} and the other parameters. Thus, two remaining parameters required to define the cohesive law, δ_f (the maximum separation) and Υ (rate factor of damage evolution), were estimated by iterative FEA to achieve a best fit of the numerical load-opening displacement and crack length results with the experimental data. The full set of parameters obtained is summarized as follows: $G_{\text{tot}} = 2.8$ kJ/m², $G_{\text{tip}} = 0.4$ kJ/m², $G_{\text{br}} = 2.4$ kJ/m², $K_0 = 100,000$ MPa/mm, $\sigma_c = 25.2$ MPa, $\sigma_{\text{max}} = 5$ MPa, $\delta_1 = 0.027$ mm, $\delta_f = 1.58$ mm and $\Upsilon = 0.137$. The numerical load-opening displacement and stiffness-opening displacement curves showed overall good agreement with the experimental results in terms of the load levels, crack length evolutions, the turning points on the curves at an opening displacement of around 17.5 mm, and the slopes of the load-opening displacement curves after the turning points, as shown in Fig. 2.2. The slight deviation in the second half of the curves was due to the absence of intralaminar damage simulation. Indeed, local damage was observed in the experiments in laminates around the bolt holes and inside the pre-crack region (see Fig. 2.3). It is possible to include such damage through improvement of the constitutive relationship and adding extra damage criteria in the bulk material with a new set of material tests. However, considering that the main objective of this work was the numerical investigation of the 2D fracture behavior rather than the accurate simulation of a specific experiment, intralaminar damage was omitted in the FEA.

$$\sigma_{br}(\delta) = e^{-\Upsilon\sqrt{\delta-\delta_1}}\sigma_{\text{max}}\left(1-\sqrt{\frac{\delta-\delta_1}{\delta_f-\delta_1}}\right), \delta_1 \leq \delta \leq \delta_f$$
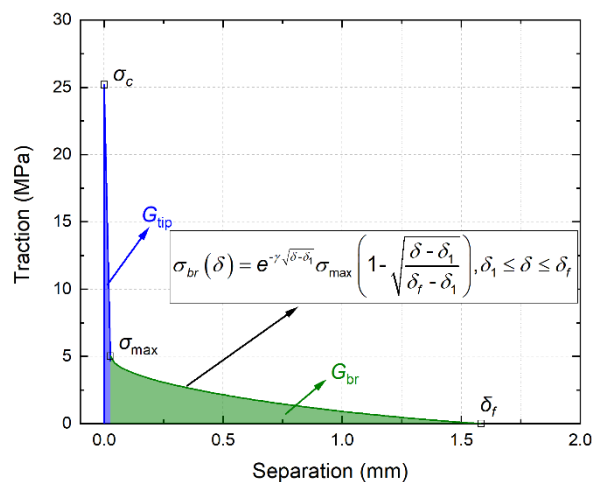
Fig. 2.5. Traction-separation law (according to [22]).

2.3.2 Simplified finite square plate model and parameters

After determination of the CZM parameters, the detailed finite square model was simplified in terms of the loading system in order to alter the pre-crack and loading zone shapes for the following parametric investigations. The new model, hereafter referred to as "simplified finite square plate model", is presented in Fig. 2.4b. In this model, the loading system was not established explicitly, but instead simulated by applying semi-rigid constraints to the pre-crack surfaces inside the bolting line, i.e., the loading zone. Specifically, the vertical displacement and all rotational displacements of the nodes on the surfaces were coupled with two reference points, while in-plane deformation was allowed. Boundary conditions were applied directly to the reference points, constraining all degrees of freedom with a 25-mm vertical displacement on the upper point. Two layers of CS8R elements were generated for each of the half-plates (CS6R elements were used inside the range of the loading zone instead), which proved to be sufficient after a sensitivity analysis. The other simulation techniques were taken from the detailed finite square plate model. The simplified model comprised 43,997 nodes and 35,780 elements. The load-opening displacement and crack length-opening displacement curves, shown in Fig. 2.2, were compared with those of the detailed model and experiments. The results from the simplified model were similar to those of the detailed model and also agreed well with the experimental results.

Up to this point, the models were used to reproduce the experiments, from which circular symmetry was always observed due to the symmetric set-up and the in-plane isotropy of the material. This is however not representative of a general delamination scenario, where the defect might be of random shape and the opening forces do not necessarily act on a circular loading zone. Therefore, based on the simplified finite square plate model, four more plates of the same dimensions as specimen CFM1 were modeled with altered pre-crack shape or loading zone shape to investigate the effect of these two parameters on the 2D delamination growth. The total of five simplified finite square plates were sorted into two groups, as shown in Fig. 2.6. In the first group, the specimens' pre-crack shapes vary from a circle to ellipses of different aspect ratios while maintaining equal circumference, which is regarded as an analogy of the pre-crack width in beam-like specimens. In the second group, different loading zone shapes were selected with the same area in order to achieve an equivalent loading condition in terms of the distributed opening loads, and the same circular pre-crack was maintained.

Group	Reference model	Model variations	
Different pre-crack shapes (same circumference)	C90-C35-S	E2/1-C35-S	E3/1-C35-S
Different loading zone shapes (same area)	C90-C35-S	C90-E2/1-S	C90-E3/1-S
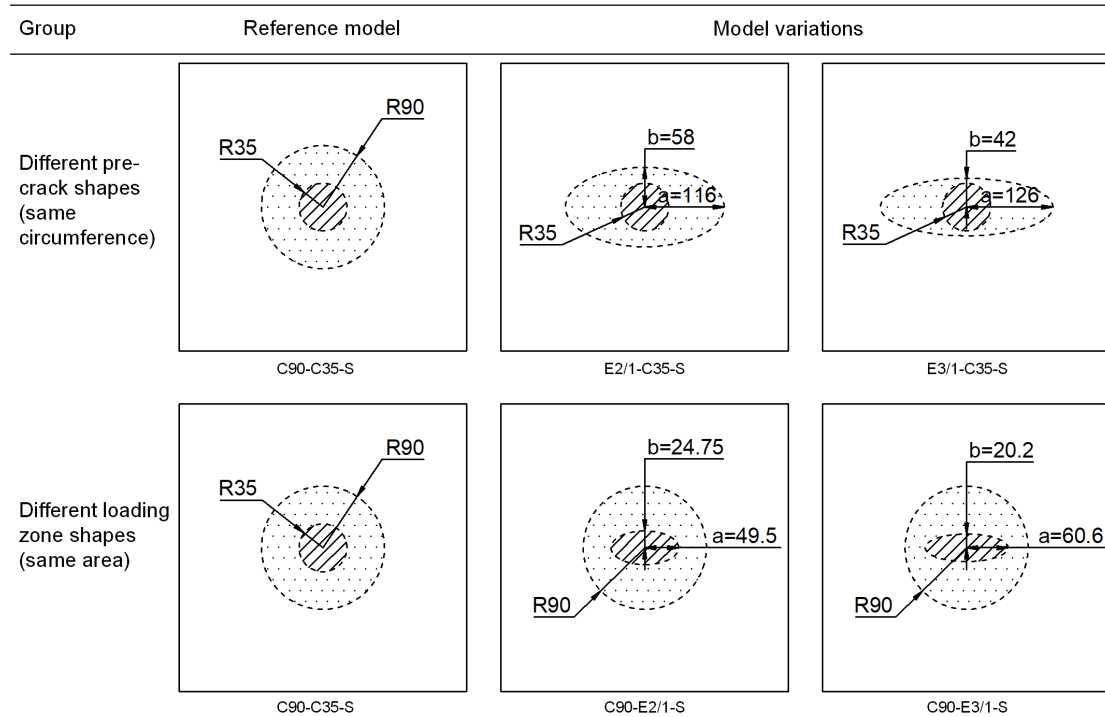
Fig. 2.6. Model list of simplified finite square plates (dashed area indicates loading zone, and dotted area indicates pre-crack).

In Fig. 2.6, the first component of the labels indicates the pre-crack shape of the specimen, e.g., "C90" denotes a circular pre-crack with a radius of 90mm, while "E2/1" denotes an elliptical pre-crack with an aspect ratio of 2:1; the second component indicates the loading zone shape; and the last component, "S", denotes "simplified finite square plates".

2.3.3 Simplified semi-infinite circular plate model and parameters

In some of the simplified finite square plates fiber bridging was not fully developed in all directions at the end of the loading process. Indeed, the delamination growth was limited by the plate size and shape, as was also the case in the experiments described in [20]. To be specific, if the loading proceeded further, the plate edges would start to have an impact, i.e., the crack would propagate too close to the edges, and the outer intact part of the plate would no longer be able to sustain the circumferential compression forces induced by stretching, leading to unstable crack propagation. On the other hand, if the plate sizes were enlarged without other modifications, stability problems would soon occur due to the circumferential compression in the laminates. Therefore, a new circular plate model was developed from the simplified finite square plate model with

an enlarged size, reaching a diameter of 1000 mm while maintaining the same nominal thickness (7.5 mm), as shown in Fig. 2.4c. Based on this model, hereafter referred to as "simplified semi-infinite circular plate model", different combinations of pre-crack shape/area, loading zone shape/area and G_{tot} were considered in order to investigate the influences of defect geometry, loading patterns and fiber bridging extent respectively. In addition, the elastic moduli employed were increased to ten times those of the previous models in order to delay the occurrence of instability. The enlarged moduli were chosen so that they are sufficiently high to provide a notable delay in buckling but not too high in case the delamination growth behavior changes (since G_{tot} is still within its original magnitude), which will be examined below. Approximately 323,000 nodes and 282,000 elements were generated for each model, and an opening displacement of up to 100 mm was applied.

In order to comprehensively investigate the effects of the different parameters, several groups of simplified semi-infinite circular plates were established, as shown in Fig. 2.7. In the first group, the plates have different pre-crack shapes of equal circumference (the first row in Fig. 2.7). In the second group, the pre-crack shapes also vary, but maintaining the same area, A_p, instead of circumference (the second row in Fig. 2.7), considering that the crack area is one of the basic physical variables in fracture mechanics. In the third group, the plates again have different pre-crack shapes of the same area, but this time the area is twice the previous value, i.e., $2A_p$ (the third row in Fig. 2.7). In the fourth group, different loading zone shapes with the same area, A_l, were selected while maintaining the same circular pre-crack (the fourth row in Fig. 2.7). And in the fifth group, the plates also have different loading zone shapes of the same area, but this time the area is twice the previous value, i.e., $2 A_l$ (the fifth row in Fig. 2.7). Additional groups were developed by changing the fracture resistance of the group of different loading zone shapes with the same basic area from the basic value (G_{tot}=2.8 kJ/m^2) to other levels (i.e., 1.4 kJ/m^2 and 4.2 kJ/m^2, which are 0.5 and 1.5 times the basic value respectively). Extra levels of fracture resistance (i.e., 0.42 kJ/m^2, 0.7 kJ/m^2 and 5.6 kJ/m^2, which are 0.14, 0.25 and 2.0 times the basic value respectively) were also assigned to the plate that has a circular pre-crack and an elliptical loading zone with an aspect ratio of 3:1. Variations of G_{tot} were achieved by modifying the two bridging parameters, δ_f and Υ in Fig. 2.5, and thus the initiation part of the cohesive law remained unchanged.

22

Group	Reference model	Model variations
Different pre-crack shapes (same circumference)	R90, R35 — C90-C35-1.0G	b=58, a=116, R35 — E2/1-C35-1.0G; b=42, a=126, R35 — E3/1-C35-1.0G
Different pre-crack shapes (same basic area, A_p)	R90, R35 — C90-C35-1.0G	b=63.6, a=127.3, R35 — E'2/1-C35-1.0G; b=52, a=156, R35 — E'3/1-C35-1.0G
Different pre-crack shapes (same doubled area, $2A_p$)	R127.3, R35 — 2C90-C35-1.0G	b=90, a=180, R35 — 2E'2/1-C35-1.0G; b=73.5, a=220.5, R35 — 2E'3/1-C35-1.0G
Different loading zone shapes (same basic area, A_l)	R90, R35 — C90-C35-0.5G / C90-C35-1.0G / C90-C35-1.5G	b=24.7, a=49.5, R90 — C90-E2/1-0.5G / C90-E2/1-1.0G / C90-E2/1-1.5G; b=20.2, a=60.6, R90 — C90-E3/1-0.14G / C90-E3/1-0.25G / C90-E3/1-0.5G / C90-E3/1-1.0G / C90-E3/1-1.5G / C90-E3/1-2.0G; b=17.5, a=70, R90 — C90-E4/1-1.0G
Different loading zone shapes (same doubled area, $2A_l$)	R90, R49.5 — C90-2C35-1.0G	b=35, a=70, R90 — C90-2E2/1-1.0G; b=28.6, a=85.8, R90 — C90-2E3/1-1.0G

Fig. 2.7. Model list of simplified semi-infinite circular plates (dashed area indicates loading zone, and dotted area indicates pre-crack).

Regarding nomenclature, the first two components of the label follow the same rule as for the simplified finite square plates, i.e., they indicate the pre-crack shape and loading zone shape, respectively. A prime symbol, " ' ", was placed after "E (elliptical)" in the first component for the groups that have different pre-crack shapes of the same area (the second and third groups) in order to differentiate them from the plates with different pre-crack shapes of the same circumference (the first group). The additional "2" before "C (circular)" or "E (elliptical)" in the first component indicates the doubled pre-crack area for the corresponding plates (the third group). And likewise, the additional "2" before "C" or "E" in the second component indicates the doubled loading

zone area. The third component denotes the fracture resistance, i.e., "1.0G" refers to the basic value of 2.8 kJ/m^2, and correspondingly, "0.14G", "0.25G", "0.5G", "1.5G" and "2.0G" refer to 0.42 kJ/m^2, 0.7 kJ/m^2, 1.4 kJ/m^2, 4.2 kJ/m^2 and 5.6 kJ/m^2 respectively. In total, 23 simplified semi-infinite circular plate models were derived.

2.4 Numerical results and discussion

2.4.1 Effect of pre-crack shape

To better describe the 2D delamination growth in the plates with elliptical pre-crack or loading zone, two orthogonal directions were selected for investigation, i.e., the major-axis direction and the minor-axis direction. Accordingly, the crack lengths in these directions, calculated radially from the plate center to the delamination front, are denoted as a_x and a_y respectively, as shown in Fig. 2.8.
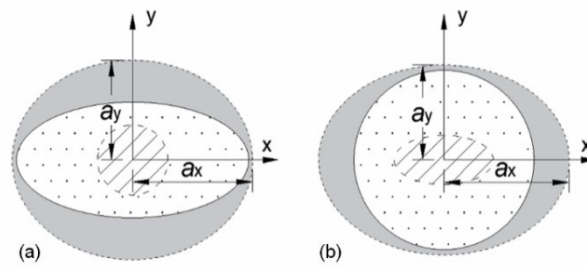
Fig. 2.8. Description of directions for crack length calculation: (a) plates with elliptical pre-crack and circular loading zone; (b) plates with circular pre-crack and elliptical loading zone.

The load-opening displacement and crack length-opening displacement curves for different pre-crack shapes at the initiation and early propagation stages are presented in Fig. 2.9 (results from simplified finite square plate models C90-C35-S, E2/1-C35-S and E3/1-C35-S). The evolution of a_x and a_y can be regarded as the upper and lower bounds of the entire crack propagation, i.e., the curves for other directions will always lie in between (i.e., the solid area in Fig. 2.9). In addition, the points indicating the crack initiation (i.e., G reaches G_{tip}) and full fiber bridging (i.e., G reaches G_{tot}) for the orthogonal directions are also shown on the corresponding crack length-opening displacement curves. Correspondingly, four specific fracture states can be identified in terms of 2D delamination growth as follows:

(1) Crack initiation in one direction, i.e., G of the first point on the pre-crack perimeter reached G_{tip};

(2) Crack initiation in all directions, i.e., G of the last point on the pre-crack perimeter reached G_{tip};

(3) Full fiber bridging in one direction, i.e., G of the first point on the pre-crack perimeter reached G_{tot};

(4) Full fiber bridging in all directions, i.e., G of the last point on the pre-crack perimeter reached G_{tot}.

For plates with elliptical pre-crack/loading zone, "the first point" refers to that in the direction with the shortest distance between the pre-crack front and the loading zone edge, i.e., y direction in Fig. 2.8a and x direction in Fig. 2.8b, and "the last point" refers to that in the direction with the longest distance between the pre-crack front and the loading zone edge, i.e., x direction in Fig. 2.8a and y direction in Fig. 2.8b. Note that the sequence of the states was determined by the model's geometry configuration. For instance, for model C90-C35-S, states (1) and (2) overlapped due to circular symmetry, as did states (3) and (4); for model E2/1-C35-S and E3/1-C35-S, state (3) occurred prior to state (2) (see the displacement levels of the marked points in Fig. 2.9), and state (4) was not yet reached at the end of the loading process due to the limited propagation.
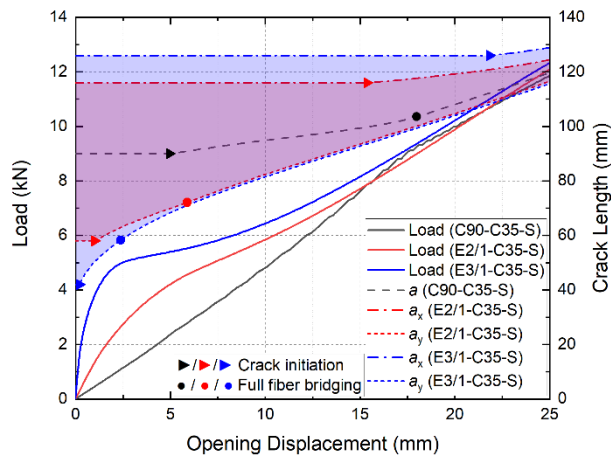
Fig. 2.9. Load and crack length vs opening displacement curves during crack initiation and early propagation for different pre-crack shapes (simplified finite square plate results).

It can be observed from Fig. 2.9 that as the pre-crack shape varied from a circle to a flat ellipse, the initial stiffness distinctly increased. This difference was attributed to

the geometrical configurations of the plates. Specifically, the shortest distance between the pre-crack front and the loading zone edge decreased rapidly from 55 mm for model C90-C35-S to around 7 mm for model E3/1-C35-S, which made the major contribution to the overall stiffness of the whole structure at the beginning of the loading. As the loading continued, the three load-opening displacement curves began to converge. At the end of the loading process, they became almost parallel with equal stiffness, showing that the differences in structural response caused by different pre-crack shapes were disappearing. A similar conclusion can be drawn from the crack length-opening displacement curves. The a_x and a_y curves were converging after the crack initiated in all directions, indicating that the delamination shape was changing towards a circle, i.e., the shape of the loading zone, and the effect of the pre-crack shape was waning. By subtracting the crack length at crack initiation (i.e., the pre-crack length) from that at full fiber bridging, the initial bridging lengths in the orthogonal directions can be obtained respectively. It was found that the initial bridging lengths differed in different configurations of this group.
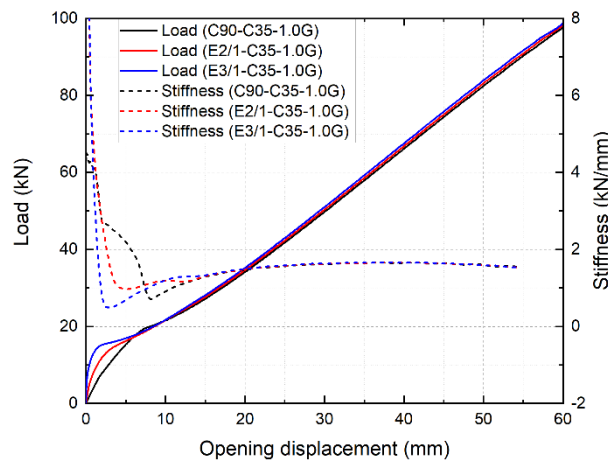
Fig. 2.10. Load and stiffness vs opening displacement curves during crack initiation and propagation for different pre-crack shapes (simplified semi-infinite circular plate results).

The load-opening displacement and stiffness-opening displacement curves for the different pre-crack shapes now including crack propagation were plotted in Fig. 2.10 (results from simplified semi-infinite circular plate models C90-C35-1.0G, E2/1-C35-1.0G and E3/1-C35-1.0G, with the latter curves being the first derivate of the former ones). The load curves were plotted up to an opening displacement of 60 mm, after

which instability occurred generally. In the simulations, the stability status was tracked by the vertical displacement of the plate edges. The stiffness curves, which are more sensitive to the stability of the plates, were only plotted up to a vertical line that marks the opening displacement level where the edge of the first plate in the group failed to remain horizontal (at 54 mm in this case).

The shapes of the curves at the initiation and early propagation stages are similar in Fig. 2.9 and Fig. 2.10 (although the load levels in the latter case are several times higher), indicating similar fracture behaviors. It is thus logical to assume that the fracture behavior of the simplified semi-infinite circular plates, after a certain extent of propagation, will also be similar, i.e., representative, despite the artificially enlarged moduli. As the models allowed larger displacements before any instability problems arose, it was feasible to achieve full fiber bridging in all directions.

The structural response can be better understood from the stiffness-opening displacement curves. All three plates went through an initial rapid softening stage, followed by a general mildly stiffening stage, and finally reached a state where stiffness remained constant. Three main different mechanisms affecting the specimens' stiffness could be distinguished, i.e., stretching, fiber bridging and crack propagation, with the first two being stiffening mechanisms and the third being a softening mechanism. The softening mechanism prevailed down to the minimum points of the stiffness curves, and then on the upward part of the curves the stiffening mechanisms became dominant until the constant-stiffness state was reached. The final constant stiffness indicates the balance between the stiffening and softening mechanisms. For the circular pre-crack shape (model C90-C35-1.0G), the minimum point (at opening displacement of 7.7 mm) corresponded to the onset of full fiber bridging in all directions. For the models with elliptical pre-crack, on the other hand, the minimum points correspond to none of the aforementioned fracture states. After full fiber bridging was reached in all directions, all three stiffness curves matched, which shows that the pre-crack shape has only a minor effect on the final constant stiffness of the system.

The G values along the pre-crack perimeter at the above-defined four specified fracture states (i.e., (1) crack initiation in one direction (red), (2) crack initiation in all directions (blue), (3) full fiber bridging in one direction (green), and (4) full fiber bridging in all directions (orange)) were normalized over G_{tot} (i.e., 2.8 kJ/m^2) and plotted in a polar coordinate system for both simplified finite square plates and simplified semi-infinite circular plates with elliptical pre-crack, as shown in Fig. 2.11.

Results from models E2/1-C35-S (solid lines) and E2/1-C35-1.0G (dashed lines) were summarized together in Fig. 2.11a, since they both have the same pre-crack and loading zone configuration, and likewise models E3/1-C35-S and E3/1-C35-1.0G in Fig. 2.11b. The corresponding opening displacement levels at which the states were reached are also presented in the legends. Thus, the *G*-level on the pre-crack perimeter in any direction can be radially read from the curve for the fracture states concerned (e.g., a value of 1.0 signifies that full fiber bridging had developed in this direction). In addition, the propagated crack shapes in model E3/1-C35-1.0G at states (2), (3) and (4) are shown in Fig. 2.12a (using the same colors as in Fig. 2.11).

The shapes of the *G*-distribution curves of the simplified finite square plate and the simplified semi-infinite circular plate of the same configuration are very similar, with the *G*-distribution from the latter model being more uniform and the states appearing at lower opening displacement levels, which is logical considering the much higher laminate stiffness. Thus, the fracture behavior is consistent in both models.
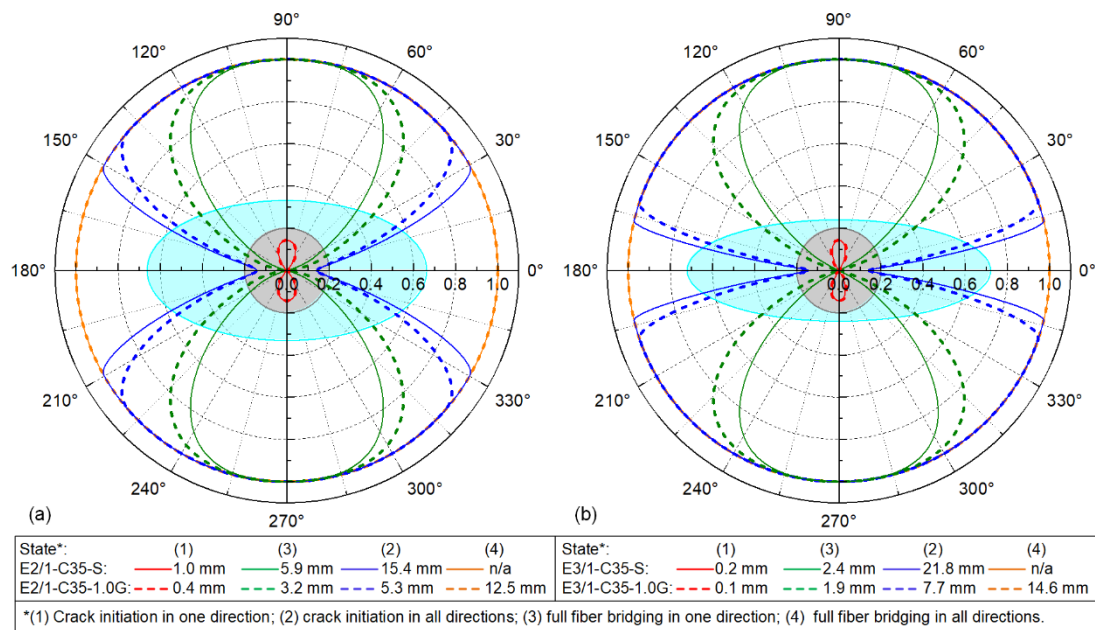
Fig. 2.11. Normalized *G*-distribution curves along pre-crack perimeter in plates with elliptical pre-crack at different fracture states: (a) E2/1-C35-S and E2/1-C35-1.0G; (b) E3/1-C35-S and E3/1-C35-1.0G.
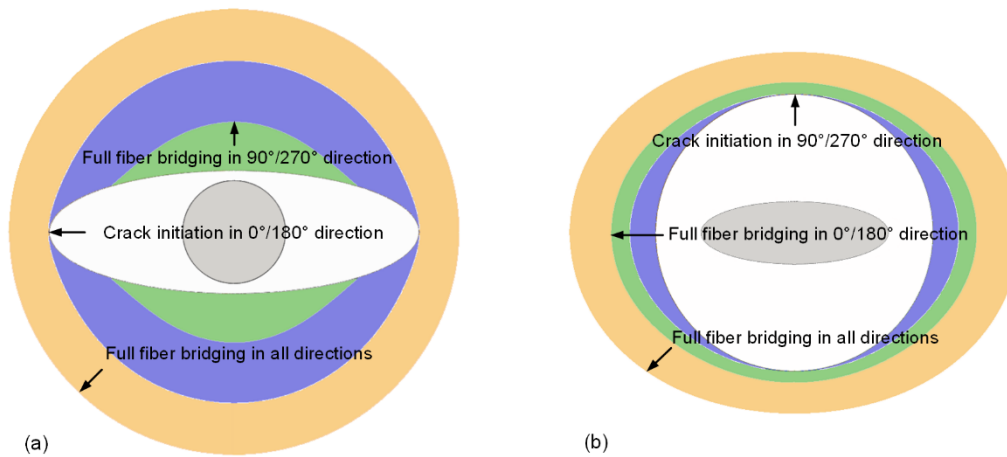
Fig. 2.12. Crack shapes at different fracture states: (a) E3/1-C35-1.0G; (b) C90-E3/1-1.0G.

In both cases, the cracks initiated and propagated firstly in the 90°/270° direction, since in this direction the distance between the pre-crack front and the loading zone edge was the shortest. As the loading continued, the crack progressively initiated and propagated in each direction and finally reached full fiber bridging in all directions. Due to the large variation in the distance between the pre-crack front and the loading zone edge, the *G*-distribution along the pre-crack perimeter showed notable non-uniformity. For instance, when full fiber bridging appeared in the 90°/270° direction in model E3/1-C35-1.0G (Fig. 2.11b), crack initiation in the 0°/180° direction, within a range of around ±15°, did not yet occur (see the green dashed curve in Fig. 2.11b and the green region in Fig. 2.12a). Comparing Fig. 2.11b to Fig. 2.11a, it was found that as the shortest distance between the pre-crack front and the loading zone edge became shorter, crack initiation in one direction and full fiber bridging in one direction appeared at a lower opening displacement; as the longest distance between the pre-crack front and the loading zone edge became longer, crack initiation in all directions and full fiber bridging in all directions appeared at a larger opening displacement; the *G*-distribution along the pre-crack front became generally less uniform.

In order to describe the overall shape evolution of the delamination in a simpler way, the crack length ratio (CLR), defined as the ratio of the crack length in the elliptical major-axis direction to that in the minor-axis direction (i.e., a_x/a_y in Fig. 2.8), is shown in Fig. 2.13 during the first 45 mm of loading. The CLR of model C90-C35-1.0G equaled a constant value of 1.0 due to its circular symmetry, denoting a circular delamination shape throughout the loading process, as was also observed in the CFM

experiments. The CLRs of the plates with elliptical pre-crack dropped rapidly from the original values (i.e., the aspect ratio of the elliptical pre-crack) to approximately 1.0 as full fiber bridging developed in all directions, i.e., the delamination shape changed from the original ellipse to a circle (the shape of the loading zone), as also shown Fig. 2.12a. This observation confirms that the pre-crack shape has only a minor effect on the final crack shape after a certain extent of crack propagation. Note that in the early stages, especially before crack initiation occurred in all directions, the delamination shape of the plates was irregular instead of elliptical due to different delays in crack initiation in different directions, see Fig. 2.12a.
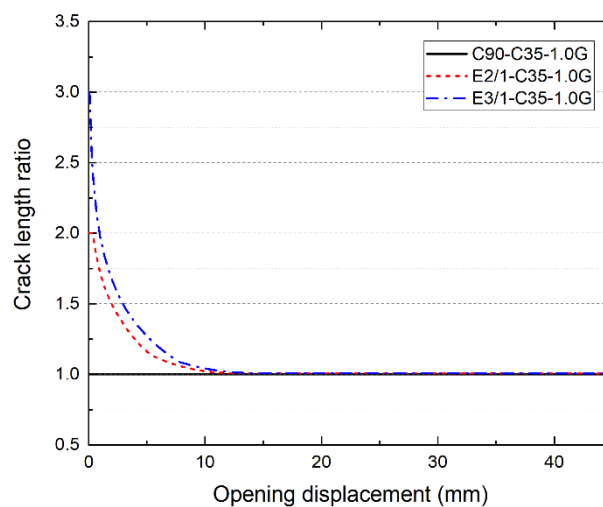
Fig. 2.13. Crack length ratio vs opening displacement curves for different pre-crack shapes.

2.4.2 Effect of pre-crack area

The load-opening displacement and stiffness-opening displacement curves during crack initiation and propagation for the basic and doubled pre-crack areas are shown in Fig. 2.14 (results from simplified semi-infinite circular plate models C90-C35-1.0G, 2C90-C35-1.0G, 2E'2/1-C35-1.0G and 2E'3/1-C35-1.0G). Since the difference between the pre-crack dimensions in the group of the same pre-crack circumference and the group of the same basic pre-crack area was small, models E'2/1-C35-1.0G and E'3/1-C35-1.0G behaved similarly to E2/1-C35-1.0G and E3/1-C35-1.0G in all respects. Hence, their results are not presented and can be referred to in the previous section (Fig. 2.10). The results in the group of doubled pre-crack area followed similar rules as in the group of the same pre-crack circumference, except that convergence of the curves occurred

later due to the increased distances between the pre-crack front and the loading zone edge. Compared with model C90-C35-1.0G, the larger pre-crack area in 2C90-C35-1.0G resulted in smaller new crack surfaces created at the same opening displacement, and consequently led to less energy being consumed, as reflected in its slightly lower load level throughout the loading process. All models with doubled pre-crack area still had the same constant stiffness as the basic reference model (C90-C35-1.0G), confirming that the constant stiffness is independent of the pre-crack area. It is worth mentioning that, unlike the other models, 2C90-C35-1.0G did not experience softening in the beginning. On the contrary, it almost maintained the initial stiffness until crack initiation due to its special pre-crack/loading zone configuration. Indeed, the latter was not only circularly symmetric but also exhibited a distance between the pre-crack front and the loading zone edge large enough to allow a certain amount of deformation before crack initiation. After crack initiation, fiber bridging was activated, and the plate entered a short stiffening stage. Then, the softening mechanism, i.e., crack propagation, prevailed over the stiffening mechanisms, i.e., fiber bridging and stretching, until full fiber bridging developed in all directions (the minimum point on the stiffness curve).
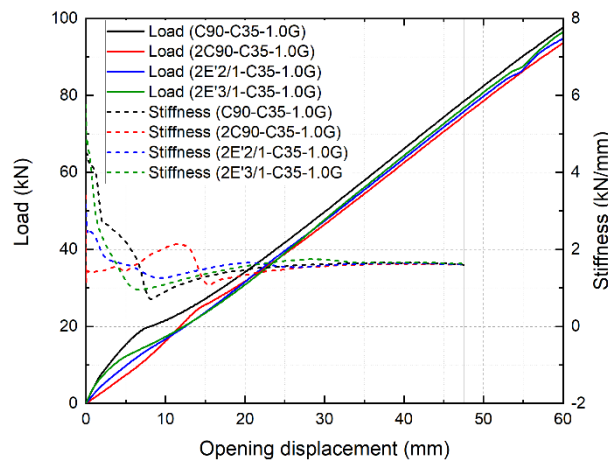
Fig. 2.14. Load and stiffness vs opening displacement curves during crack initiation and propagation for different pre-crack areas (simplified semi-infinite circular plate results).

The CLR-opening displacement curves from the group of the same basic pre-crack area and the group of the same doubled pre-crack area are shown in Fig. 2.15. As previously discussed, the increase in the distances between the pre-crack front and the loading zone edge resulted in a delay in the occurrence of the defined fracture states.

Therefore, the CLR curves for the doubled pre-crack area were smoother and reached a constant value at larger displacements. The constant CLR values for elliptical pre-cracks are very close to 1.0, i.e., the aspect ratio of the loading zone (a circle), but a slight deviation was observed, which increased as the pre-crack area and pre-crack aspect ratio increased, indicating a greater difference in the energy consumed in different directions. Essentially, different energy consumption histories in different directions finally led to slightly noncircular crack shapes at the constant-stiffness state.
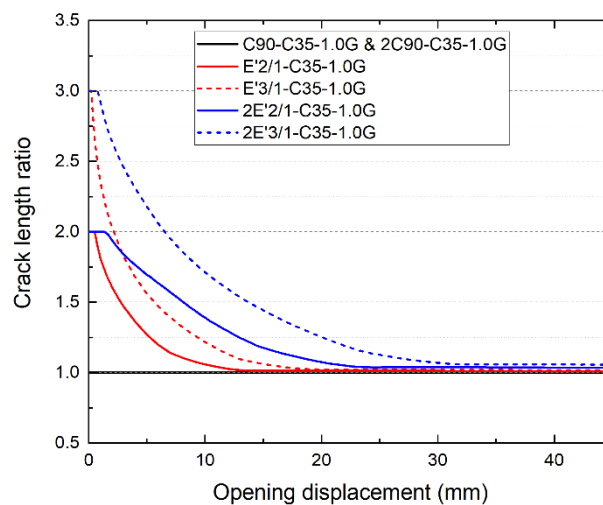
Fig. 2.15. Crack length ratio vs opening displacement curves for different pre-crack areas.

2.4.3 Effect of loading zone shape

The load-opening displacement and the crack length-opening displacement curves during crack initiation and early propagation for different loading zone shapes are presented in Fig. 2.16 (results from simplified finite square plate models C90-C35-S, C90-E2/1-S and C90-E3/1-S). As the aspect ratio of the loading zone increased from 1 to 3 (i.e., from a circle to a flat ellipse), the initial stiffness of the system also increased although not significantly. The shortest distance between the pre-crack front and the loading zone edge decreased from 55 mm for model C90-C35-S to around 29.4 mm for model C90-E3/1-S, which is considered the main factor causing the differences in initial stiffness. Full fiber bridging in all directions developed in all three plates, after which the three load-opening displacement curves converged and became parallel. Although different crack shapes were formed at the end of the loading, as reflected in the crack length curves, the stiffness and load levels of the three plates were very similar. This is

32

attributed to the equal areas of the loading zones of the plates, which can be regarded as the dominant factor controlling the structural response for the cases investigated. The initial bridging lengths in the orthogonal directions, calculated from the crack length-opening displacement curves, were found to be approximately equal (~13.6 mm) not only within each plate but also among all three plates.
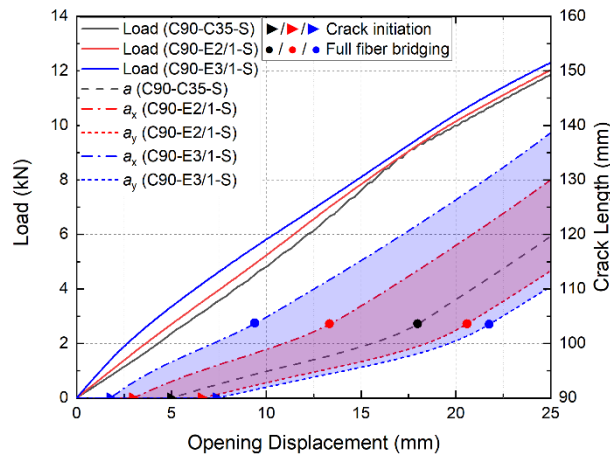
Fig. 2.16. Load and crack length vs opening displacement curves during crack initiation and early propagation for different loading zone shapes (simplified finite square plate results).
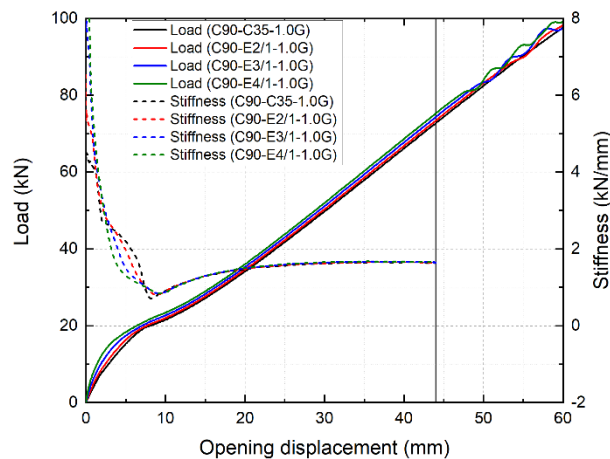
Fig. 2.17. Load and stiffness vs opening displacement curves during crack initiation and propagation for different loading zone shapes (simplified semi-infinite circular plate results).

The load-opening displacement and stiffness-opening displacement curves during crack initiation and propagation for the different loading zone shapes were plotted in Fig. 2.17 (results from simplified semi-infinite circular plate models C90-C35-1.0G,

C90-E2/1-1.0G, C90-E3/1-1.0G and C90-E4/1-1.0G). All four load-opening displacement curves converged after full fiber bridging in all directions with the same stiffness and a similar load level, in spite of different loading zones. All four plates experienced an initial rapid softening, followed by mild stiffening, and finally reached the constant-stiffness state, indicating the balance between the stiffening and softening mechanisms. The minimum points on the stiffness curves, appearing at a similar displacement level (~9.0 mm), corresponded to the onset of full fiber bridging in all directions, after which the curves overlapped, showing identical behavior. This shows that the loading zone shape also has a minor effect on the final constant stiffness of the system, provided that the areas of the loading zones are the same.

State*:	(1)	(2)	(3)	(4)	State*:	(1)	(2)	(3)	(4)
C90-E2/1-S:	—— 3.0 mm	—— 6.6 mm	—— 13.3 mm	—— 20.6 mm	C90-E3/1-S:	—— 1.7 mm	—— 7.4 mm	—— 9.4 mm	—— 21.8 mm
C90-E2/1-1.0G:	– – – 1.0 mm	– – – 2.3 mm	– – – 5.8 mm	– – – 8.8 mm	C90-E3/1-1.0G:	– – – 0.6 mm	– – – 2.5 mm	– – – 4.4 mm	– – – 9.2 mm

*(1) Crack initiation in one direction; (2) crack initiation in all directions; (3) full fiber bridging in one direction; (4) full fiber bridging in all directions.
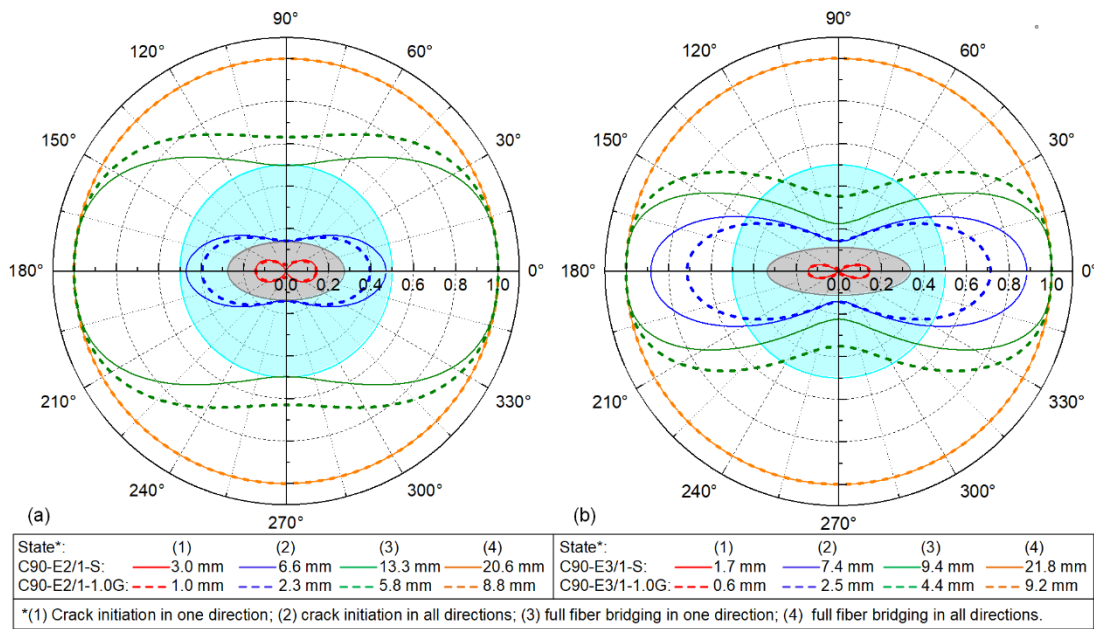
Fig. 2.18. Normalized *G*-distribution curves along pre-crack perimeter in plates with elliptical loading zone at different fracture states: (a) model C90-E2/1-S and C90-E2/1-1.0G; (b) model C90-E3/1-S and C90-E3/1-1.0G.

The normalized *G*-distribution along the pre-crack perimeter at the four specified fracture states, along with their corresponding displacement levels, are presented in Fig. 2.18 for both simplified finite square plates and simplified semi-infinite circular plate models with elliptical loading zone (C90-E2/1-S, C90-E3/1-S, C90-E2/1-1.0G and C90-E3/1-1.0G). The crack shapes in model C90-E3/1-1.0G at the last three fracture states are further illustrated in Fig. 2.12b. The shapes of the curves of the two models with the same configuration are similar, with the *G*-distribution of the simplified semi-

infinite circular plate being more uniform and the states appearing at lower opening displacement levels due to the increased moduli.

Crack initiation in all directions occurred earlier in these plates than full fiber bridging in all directions. The crack also initiated and propagated firstly from the direction with the shortest distance between the pre-crack front and the loading zone edge, and the relationship between the opening displacement levels of the fracture states and the shortest/longest distance followed the same rule as discussed in the previous section, whereas in these plates, the G-distribution along the pre-crack perimeter was much more uniform. For instance, when full fiber bridging occurred in the 0°/180° direction in model C90-E3/1-1.0G, the crack had also propagated to a small extent in the 90°/270° direction (see the green dashed curve in Fig. 2.18b and the green region in Fig. 2.12b); and the crack shapes at early stages in Fig. 2.12b are more rounded instead of irregular as in Fig. 2.12a, indicating less delay in crack initiation and early propagation in different directions. Within each group of models (simplified finite square plates or simplified semi-infinite circular plates), the displacement levels of each state are fairly close between the two loading zone configurations, implying that the equivalence of the loading zone by area cannot only lead to an identical stiffness response after full fiber bridging developed in all directions, but also result in a similar fracture response in the early stages, which was also reflected in the equal bridging lengths in the simplified finite square plates (Fig. 2.16).

The CLR-opening displacement curves for plates with different loading zone shapes of the same basic area (results from simplified semi-infinite circular plate models C90-E2/1-1.0G, C90-E3/1-1.0G and C90-E4/1-1.0G) are presented in Fig. 2.19 (red curves). The CLRs rose sharply from 1.0 (denoting the original circular pre-crack), then slowed after the crack propagated in all directions, and reached a peak before full fiber bridging in all directions. The curves then declined slowly until they entered a plateau with a constant value above 1.0, which corresponded to the constant-stiffness state introduced above, indicating that the balance between the stiffening mechanisms and the softening mechanism was achieved in each direction after different energy consumption histories, so that the circumferential curvature of the half-laminate finally remained constant. The peaks of the CLR curves do not correspond to any specified fracture states. However, all three curves reached the peak at around the same opening displacement, indicated by a vertical red line. A higher aspect ratio of the loading zone, i.e., a flatter elliptical loading zone, resulted in a higher CLR, i.e., a flatter elliptical

crack, throughout the loading, but the crack shape was generally much closer to a circle than the original shape of the loading zone. The CLR evolution corresponded to the delamination shape variation as follows: the crack propagated rapidly from the circular pre-crack in the a_x direction, until initiation occurred along the whole pre-crack front. Subsequently, the growth rates in different directions became more and more balanced and the elliptical crack more and more rounded during propagation. Eventually the constant-stiffness state was reached, where the delamination grew in an elliptical shape with constant aspect ratio.
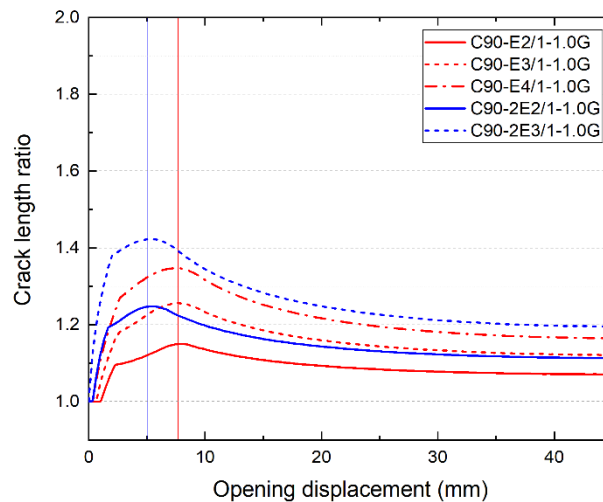
Fig. 2.19. Crack length ratio vs opening displacement curves for different loading zone shapes and areas.

2.4.4 Effect of loading zone area

The load-opening displacement and stiffness-opening displacement curves during crack initiation and propagation for the basic and doubled loading zone areas are shown in Fig. 2.20 (results from simplified semi-infinite circular plate models C90-C35-1.0G, C90-2C35-1.0G, C90-2E2/1-1.0G and C90-2E3/1-1.0G). The results in the group of the same doubled loading zone area are quite similar to those from the group of the same basic area (Fig. 2.17), and thus will not be discussed again here. By comparing the results from models C90-C35-1.0G and C90-2C35-1.0G, it can be concluded that doubling the loading zone area increased the load levels throughout the loading process. Regarding the stiffness response, a larger loading zone area also increased the initial stiffness considerably due to shorter distances between the pre-crack front and the loading zone edge, and caused full fiber bridging in all directions to occur at a lower

opening displacement level (the minimum point on the stiffness curve). Following full fiber bridging in all directions, the stiffening mechanisms of the systems prevailed over the softening mechanism for both plates until a final balance was reached, which marked the constant-stiffness state. The constant stiffness also increased slightly as the loading zone area doubled.
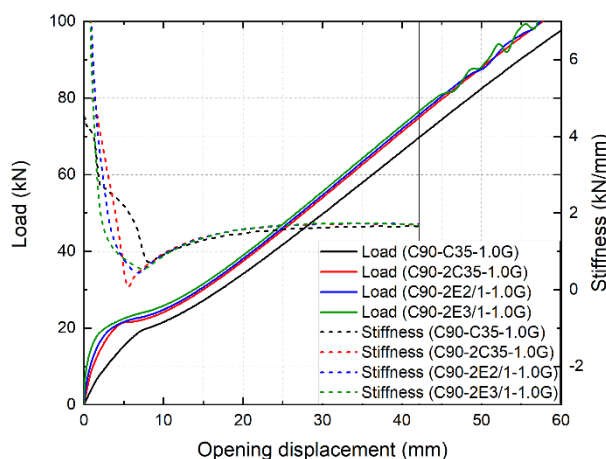
Fig. 2.20. Load and stiffness vs opening displacement curves during crack initiation and propagation for different loading zone areas (simplified semi-infinite circular plate results).

The CLR-opening displacement curves of models C90-2E2/1-1.0G and C90-2E3/1-1.0G are presented in Fig. 2.19 (blue curves). Comparing them with the red curves revealed that the general trends of the curves are very similar. However, the CLR increased as the loading zone area doubled throughout the loading process. The increase of the CLRs at the constant-stiffness state indicated that, as the loading zone area doubled, the final crack shape became slightly closer to the loading zone shape, i.e., flatter and less rounded. Doubling the loading zone area also caused the peaks to appear at a lower opening displacement level, which proved that the opening displacement level of the peak was independent of the loading zone shape (i.e., the aspect ratio) but dependent on the loading zone area.

2.4.5 Effect of fracture resistance

The load-opening displacement and stiffness-opening displacement curves during crack initiation and propagation for the plates with the same pre-crack/loading zone configuration but different facture resistances are shown in Fig. 2.21. As the fracture

resistance was increased to twice the basic value (5.6 kJ/m^2 for model C90-E3/1-2.0G), the buckling of the plate occurred at a low opening displacement level of around 34 mm, indicated by a vertical black line in the figure, and all stiffness evolutions after this level were not presented. Since the initiation components of the cohesive laws were identical, all models had the same initial stiffness and load response. As soon as the crack started to propagate, both the load and the stiffness curves deviated significantly. Higher fracture resistance resulted in higher stiffness and higher load levels throughout the loading process. In addition, increasing the fracture resistance also caused the four specified fracture states to appear at higher opening displacement levels; if the fracture resistance was high enough, all four states could be clearly identified from the stiffness curves (see the stiffness curve of model C90-E3/1-2.0G for example).
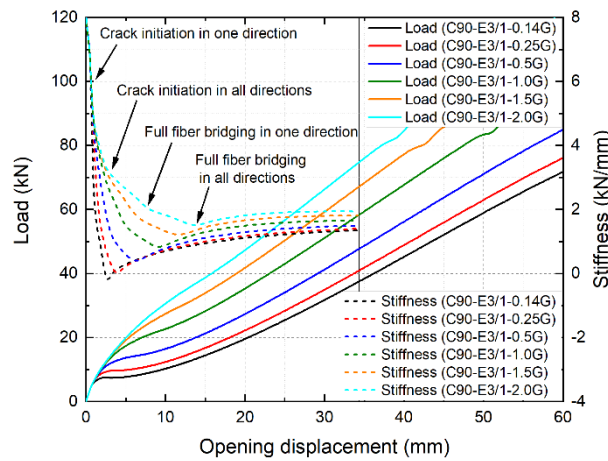
Fig. 2.21. Load and stiffness vs opening displacement curves during crack initiation and propagation for different fracture resistances (simplified semi-infinite circular plate results).

To further investigate the effect of fracture resistance on the final state of the plates, the ascending segments of the stiffness curves (the part after full fiber bridging developed in all directions) in Fig. 2.21 were fitted with exponential functions to extract the constant stiffness values at infinite opening displacement for this specific pre-crack/loading zone configuration. These values were then plotted against the corresponding G_{tot} value of the plate in Fig. 2.22. A linear relationship between the constant stiffness and G_{tot} was observed, confirming the conclusions in [28].
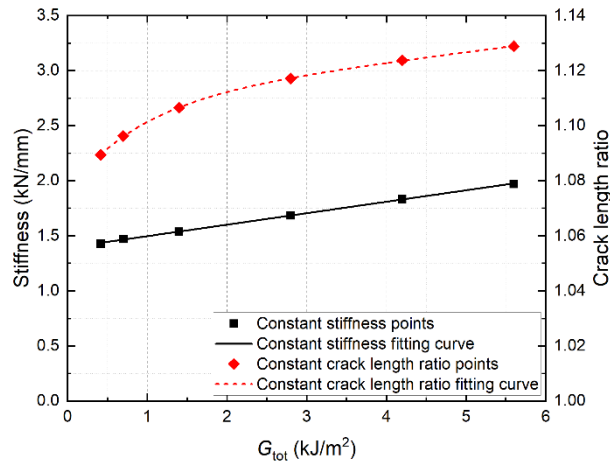
Fig. 2.22. Constant stiffness and crack length ratio at constant-stiffness state vs G_{tot} for C90-E3/1- configuration.
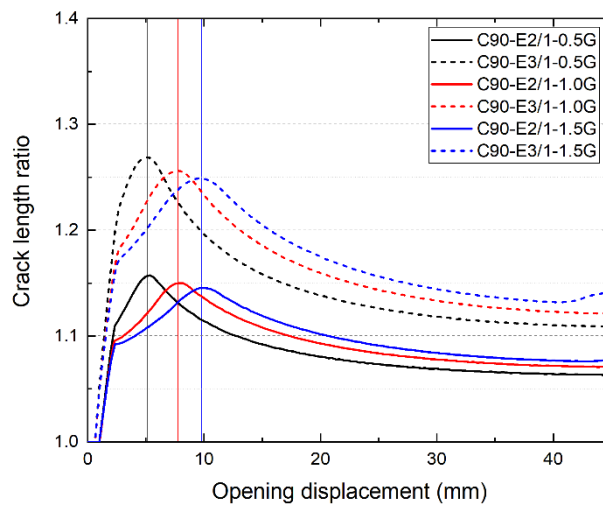
Fig. 2.23. Crack length ratio vs opening displacement curves for different loading zone shapes and fracture resistances.

The CLR-opening displacement curves were plotted in Fig. 2.23 for plates of two circular pre-crack/elliptical loading zone configurations with three different fracture resistances. As the fracture resistance increased, the CLR at the constant-stiffness state also increased slightly (i.e., the final delamination shape turned to a flatter ellipse), and the appearance of the peaks (marked with vertical lines) of the curves were delayed to a higher opening displacement level.

The CLR at constant-stiffness state was extracted by exponential fitting of the descending segments of the CLR-opening displacement curves for plates with elliptical loading zone. The CLRs at constant-stiffness state of the plates with the C90-E3/1- configuration were then plotted against the corresponding G_{tot} in Fig. 2.22 to show the

relationship between the final crack shape and fracture resistance. The CLR at constant-stiffness state was found to increase nonlinearly with G_{tot}, signifying that improvement of the fracture resistance made the final crack shape more similar to the loading zone shape (less rounded), but the effect became weaker as the resistance further improved.

2.4.6 Comparison of effects

By comparing the results in Section 4.1 and 4.3, it could be concluded that the pre-crack shape had a much stronger effect on the structural stiffness at the initiation and early propagation stages than the loading zone shape. The variation of the distances between the pre-crack front and the loading zone edge (similar to the effect of the pre-crack length in DCBs) is considered the main factor causing such differences in initial stiffness and also the G-distribution along the pre-crack perimeter. The G-distribution along the pre-crack perimeter was found to be more uniform in the plates with elliptical loading zone than those with elliptical pre-crack. Consequently, the bridging lengths in different directions at the onset of full fiber bridging in all directions are approximately the same in the former plates, but clearly differed in the latter plates.

As soon as full fiber bridging developed in all directions, the influence of both the pre-crack shape and area and the loading zone shape on the stiffness became minor. Doubling the loading zone area increased the constant stiffness, but the effect was weak. For the cases investigated, the most relevant parameter affecting the constant stiffness is the fracture resistance, and a linear relationship between them was observed. Regarding load levels, both the pre-crack area and the loading zone area had a slight influence, with the former contributing mainly through the amount of energy consumed during crack propagation, i.e., a larger pre-crack area led to smaller new crack surfaces created at the same opening displacement level.

To investigate the effect of the loading zone shape/area and the fracture resistance on the final crack shape, the CLR at the constant-stiffness state was plotted against the loading-zone aspect ratio for the plates with specific loading zone and fracture resistance combinations, as shown in Fig. 2.24. The sample points were augmented by simply inversing the CLR at the constant-stiffness state and the aspect ratio, meaning a 90° rotation in the calculation direction (from a_x/a_y to a_y/a_x, see Fig. 2.8) for each model. Subsequently, the points were sorted into three groups according to the models' loading zone area and G_{tot}, and fitted with a power function respectively, revealing a nonlinear relationship. The results show that although a higher loading zone aspect ratio (i.e., a

flatter elliptical loading zone) will lead to a higher CLR (a flatter elliptical crack shape), the influence of the loading zone shape is somewhat limited. An aspect ratio of e.g., 4 only led to a CLR at the constant-stiffness state of 1.16 for model C90-E4/1-1.0G. From the fitting curves it can be concluded that the CLR at the constant-stiffness state is less sensitive to G_{tot}, as doubling the G_{tot} value only caused a slight change (also corroborated in Fig. 2.22 for the C90-E3/1- configuration), whereas doubling the area caused a more obvious deviation of the curves.
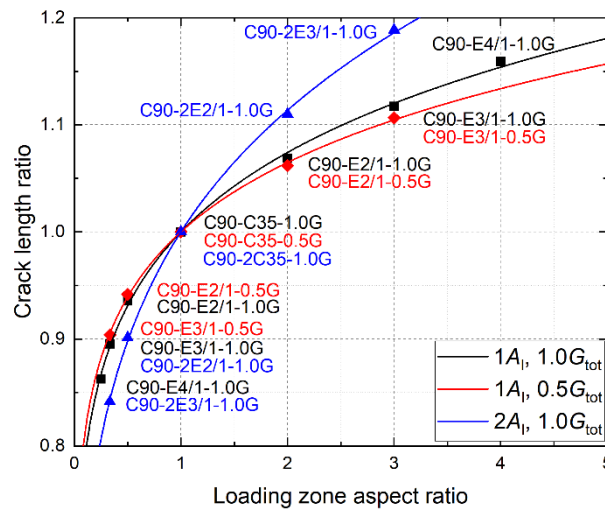
Fig. 2.24. Crack length ratio at constant-stiffness state vs loading zone aspect ratio for different loading zone areas and fracture resistances.

2.5 Conclusions

A numerical investigation of the 2D delamination growth in glass fiber-reinforced polymer laminates using cohesive zone modeling was carried out. The influences of the pre-crack shape/area, the loading zone shape/area and the fracture resistance on the 2D fracture behavior at crack initiation and early propagation stages and after a certain extent of crack propagation were parametrically studied, based on three types of models, i.e., a detailed finite square plate model, a simplified finite square plate model and a simplified semi-infinite circular plate model. The following conclusions could be drawn:

- Generally speaking, the plates investigated underwent an initial rapid softening stage and a slow stiffening stage under opening loads. Finally, the plates entered a state where the stiffness and crack shape became constant.
- The pre-crack shape had a strong effect on the structural stiffness and the strain energy release rate distribution along the pre-crack perimeter during crack

initiation and early propagation, i.e., a flatter elliptical pre-crack resulted in a higher initial stiffness and a less uniform distribution. Therefore, the pre-crack shape in laminates plays an important role in designs where no crack propagation or only limited crack propagation is allowed, since small variations in the pre-crack shape can result in large differences in the initial stiffness and initiation load (displacement).

- A larger pre-crack area reduced the initial stiffness and load level throughout the loading process. It also delayed crack initiation and propagation.

- The loading zone shape mainly affected the crack shape during propagation, and had a moderate effect on the initial stiffness of the structure. Thus, the loading zone shape should be specifically designed according to the actual opening effects on the delamination instead of selected arbitrarily during analyses and simulations.

- After full fiber bridging in all directions, the structural stiffness became independent of the pre-crack shape/area and loading zone shape.

- Increasing the loading zone area led to slightly higher constant stiffness after full fiber bridging developed in all directions and resulted in a final crack shape more closely resembling the shape of the loading zone.

- The constant structural stiffness after full fiber bridging developed in all directions increased linearly with the fracture resistance. Higher fracture resistance also caused the final crack shape to more closely resemble the shape of the loading zone.

In the present work, a uniform cohesive law was used for the laminates in all directions throughout the loading process despite the different pre-crack/loading zone configurations. In fact, G_{br} should vary slightly among different directions and at different loading states (around ±20% according to initial estimations) due to the changing arm curvatures, which affect the pull-out behavior of single fibers/fiber bundles at the crack surfaces and consequently lead to slightly different fiber bridging behaviors. However, the disregard of the variation in G_{br} was considered acceptable and did not significantly affect the validity of the conclusions, since the stiffness and crack shape were not very sensitive to the change in the fracture resistance. The methodology of the present work is also applicable for orthotropic materials as long as appropriate cohesive laws in the different material directions are available.

References

[1]   Bolotin V V. Delaminations in composite structures: Its origin, buckling, growth and stability. Compos Part B Eng 1996;27:129–45.

[2]   Wisnom MR. The role of delamination in failure of fibre-reinforced composites. Philos Trans R Soc A Math Phys Eng Sci 2012;370:1850–70.

[3]   Rhead AT, Butler R. Compressive static strength model for impact damaged laminates. Compos Sci Technol 2009;69:2301–7.

[4]   Naya F, Pappas G, Botsis J. Micromechanical study on the origin of fiber bridging under interlaminar and intralaminar mode I failure. Compos Struct 2019;210:877–91.

[5]   Canal LP, Pappas G, Botsis J. Large scale fiber bridging in mode I intralaminar fracture. An embedded cell approach. Compos Sci Technol 2016;126:52–9.

[6]   Sorensen L, Botsis J, Gmür T, Humbert L. Bridging tractions in mode I delamination: Measurements and simulations. Compos Sci Technol 2008;68:2350–8.

[7]   Shahverdi M, Vassilopoulos AP, Keller T. Modeling effects of asymmetry and fiber bridging on Mode I fracture behavior of bonded pultruded composite joints. Eng Fract Mech 2013;99:335–48.

[8]   Zhao L, Gong Y, Zhang J, Chen Y, Fei B. Simulation of delamination growth in multidirectional laminates under mode I and mixed mode I/II loadings using cohesive elements. Compos Struct 2014;116:509–22.

[9]   Soto A, González E V, Maimí P, Turon A, Sainz de Aja JR, de la Escalera FM. Cohesive zone length of orthotropic materials undergoing delamination. Eng Fract Mech 2016;159:174–88.

[10]   Brunner AJ. Experimental aspects of Mode I and Mode II fracture toughness testing of fibre-reinforced polymer-matrix composites. Comput Methods Appl Mech Eng 2000;185:161–72.

[11]   Shahverdi M, Vassilopoulos AP, Keller T. Mixed-mode quasi-static failure criteria for adhesively-bonded pultruded GFRP joints. Compos Part A Appl Sci Manuf 2014;59:45–56.

[12]   Manshadi BD, Farmand-Ashtiani E, Botsis J, Vassilopoulos AP. An iterative analytical/experimental study of bridging in delamination of the double cantilever beam specimen. Compos Part A Appl Sci Manuf 2014;61:43–50.

[13]   Senthil K, Arockiarajan A, Palaninathan R. Experimental determination of fracture toughness for adhesively bonded composite joints. Eng Fract Mech 2016;154:24–42.

[14]   Jiang Z, Wan S, Keller T, Fang Z, Vassilopoulos AP. Influence of curved delamination front on R-curve of DCB specimen. Compos Struct 2019;227:111311.

[15]   Davidson BD. An Analytical Investigation of Delamination Front Curvature in Double Cantilever Beam Specimens. J Compos Mater 1990;24:1124–37.

[16]   Jiang Z, Wan S, Zhong Z, Li S, Shen K. Effect of curved delamination front on mode-I fracture toughness of adhesively bonded joints. Eng Fract Mech 2015;138:73–91.

[17]   Manshadi BD, Vassilopoulos AP, Botsis J. A combined experimental/numerical study of the scaling effects on mode I delamination of GFRP. Compos Sci Technol 2013;83:32–9.

[18]   Canal LP, Alfano M, Botsis J. A multi-scale based cohesive zone model for the analysis of thickness scaling effect in fiber bridging. Compos Sci Technol 2017;139:90–8.

[19]   Pappas GA, Botsis J. Towards a geometry independent traction-separation and angle relation due to large scale bridging in DCB configuration. Compos Sci Technol 2020;197:108172.

[20]   Cameselle-Molares A, Vassilopoulos AP, Keller T. Experimental investigation of two-dimensional delamination in GFRP laminates. Eng Fract Mech 2018;203:152–71.

[21]   Kumar P, Reddy SR. Experimental determination of interlaminar GIc using a fully embedded centre-cracked specimen. Eng Fract Mech 1998;59:183–9.

[22]   Cameselle-Molares A, Vassilopoulos AP, Renart J, Turon A, Keller T. Numerical simulation of two-dimensional in-plane crack propagation in FRP laminates. Compos Struct 2018;200:396–407.

[23]   Kwon H, Kim H. Buckling and debond growth of partial debonds in adhesively bonded composite splice joints. Compos Struct 2007;79:590–8.

[24]   Riccio A, Raimondo A, Di Caprio F, Scaramuzzino F. Delaminations buckling and growth phenomena in stiffened composite panels under compression. Part II: A numerical study. J Compos Mater 2014;48:2857–70.

44

[25] Haselbach PU, Branner K. Initiation of trailing edge failure in full-scale wind turbine blade test. Eng Fract Mech 2016;162:136–54.

[26] Rhead AT, Butler R, Hunt GW. Compressive strength of composite laminates with delamination-induced interaction of panel and sublaminate buckling modes. Compos Struct 2017;171:326–34.

[27] Senthil K, Arockiarajan A, Palaninathan R. Numerical study on the onset of initiation of debond growth in adhesively bonded composite joints. Int J Adhes Adhes 2018;84:202–19.

[28] Cameselle-Molares A, Vassilopoulos AP, Renart J, Turon A, Keller T. Numerically-based method for fracture characterization of Mode I-dominated two-dimensional delamination in FRP laminates. Compos Struct 2019;214:143–52.

[29] Turon A, Dávila CG, Camanho PP, Costa J. An engineering solution for mesh size effects in the simulation of delamination using cohesive zone models. Eng Fract Mech 2007;74:1665–82.

[30] Ramberg W, Osgood WR. Description of stress-strain curves by three parameters. Natl Advis Comm Aeronaut 1943.

[31] Desu RK, Nitin Krishnamurthy H, Balu A, Gupta AK, Singh SK. Mechanical properties of Austenitic Stainless Steel 304L and 316L at elevated temperatures. J Mater Res Technol 2016.

[32] Frossard G, Cugnoni J, Gmür T, Botsis J. Mode I interlaminar fracture of carbon epoxy laminates: Effects of ply thickness. Compos Part A Appl Sci Manuf 2016;91:1–8.

[33] Turon A, Camanho PP, Costa J, Renart J. Accurate simulation of delamination growth under mixed-mode loading using cohesive elements: Definition of interlaminar strengths and elastic stiffness. Compos Struct 2010;92:1857–64.

Chapter 3

Mode-II delamination: experimental investigation

3.1 Introduction

Composite laminates have been widely used in recent decades in various industries including aerospace, automobile, energy and civil engineering thanks to their light weight and favorable in-plane mechanical properties. On the other hand, their much lower through-thickness performance is regarded as the main weakness [1]. Specifically, interlaminar tension and shear tend to induce separation between adjacent layers (i.e., delamination), significantly reducing structural integrity [2]. It is therefore essential to have an in-depth understanding of this phenomenon, in particular by means of experimental investigations [3]. Traditional delamination experiments favor beam-like specimens that confine the fracture behavior to one dimension, i.e., the crack propagates along the longitudinal direction with fixed crack width (beam width) under a certain fracture mode, e.g., double cantilever beam (DCB) tests for Mode I, end-loaded spilt (ELS) tests and end-notched flexure (ENF) tests for Mode II, and mixed-mode bending (MMB) tests for mixed-Mode. The above-mentioned experimental methods have been well established in several standards [4–6] and adopted in numerous works [7–9]. However, delamination in real structures, e.g., composite bridge decks and wing boxes in airplanes, will likely grow in multiple or even all directions in the delamination plane depending on the loading condition, thus presenting a two-dimensional (2D) pattern. In fact, even the traditional beam experiments, which are supposedly simple, are not strictly one-dimensional (1D), since the crack front can become curved during initiation and propagation, leading to inaccurate estimations of the strain energy release rate (SERR) [10].

Experiments on composites that contain embedded cracks propagating in two dimensions can be found in a large number of works, many of which fall into the category of delamination (debond) buckling [11–14]. Corresponding analytical [13,15] and numerical [12,14,16] investigations have also been carried out in this domain, covering various delamination shapes (i.e., elliptical or rectangular), buckling modes (i.e., local, global or mixed buckling) and loading conditions (i.e., in-plane compression or flexure). In most of the studies, however, the main objectives were to determine the

critical load and understand the interaction between delamination growth and post-buckling behavior, thus leaving the effect of the 2D condition on the fracture performance and the relevant phenomena unexplored. Indeed, in such analyses, the critical SERR was typically assumed to be identical to that measured from 1D beam-like specimens [13,14,16]. In addition, the crack front in the buckled structures is generally under a mixed-Mode (usually Mode-I dominant) fracture condition due to the complex stress state, which adds more difficulties to the understanding of the delamination behavior owing to insufficient knowledge of each individual mode in two dimensions. To complicate matters further, the mode mixity ratio is likely to vary along the delamination front and change during loading. Chai and Babcock [15] and Rhead et al. [13] omitted this problem and took Mode-I critical SERR, G_{Ic}, as the crack propagation criterion for a conservative estimation, while Nilsson et al. [12] assumed a constant and uniform mode mixity distribution along the delamination front for the sake of simplification.

Another research area frequently involving 2D delamination is (low-velocity) impact delamination, where drop-weight tests are commonly employed [17]. In the experiments, an impactor is dropped onto circular or rectangular plate specimens horizontally supported and clamped along the edge, inducing Mode-II dominant delamination accompanied by other damage mechanisms such as fiber breakage and matrix cracking [18]. Davies et al. [19] and Davies and Zhang [20] developed a strategy for damage prediction in carbon fiber laminates subjected to low velocity impact, relating the critical impact force for instant delamination to the Mode-II critical SERR, G_{IIc}. Based on this relation, Cartié and Irving [21] further suggested impact experiments as an alternative (2D) method for the determination of G_{IIc} using the measured impact force. The resulting G_{IIc} values showed reasonable agreement with those obtained from standardized beam tests for all four types of carbon fiber laminates investigated. In fact, impact delamination is difficult for analyses in the context of fracture mechanics, since it usually occurs at multiple interfaces of different depths with the presence of other damage mechanisms, not to mention the rate-dependency of SERR and the force signal oscillations in the experiments [2]. Efforts have been made at the prediction of impact response through quasi-static tests using the identical set-up to the impact tests. Good approximation was achieved regarding the onset of delamination and dynamic force-deflection behavior at low to medium incident energies/displacements, especially for thick laminates [22]. Some researchers continued to perform Compression after Impact

(CAI) experiments [21,23], and then the problem essentially reverts to delamination buckling again.

Other types of 2D shear-Mode delamination experiments were carried out in [24,25]. Chatterjee et al. [24] performed a series of three-point bending tests on wide beams with embedded elliptical pre-cracks in both half-spans. G_{IIc} obtained from traditional beam specimens was applied to the crack propagation criterion, although the delamination was under a mixed-Mode II/III fracture condition with varying mixity ratios along the periphery. Consequently, the predicted failure loads were generally lower than experimental results. Edge delamination in circular plates under uniform water pressure with the edge clamped was experimentally investigated in [25]. Unstable delamination growth was observed, leading to instant failure.

Despite a large number of direct or indirect investigations of 2D fracture in the literature, few specifically aimed at the differences from 1D cases. Kumar and Reddy [26] conducted 2D debonding experiments by opening a central circular pre-crack in circular bonded-plexiglass plates. The G_{Ic} estimated through analytical solution without considering geometrical nonlinearity was found to be 33% less than that obtained from DCB specimens. However, contradictory conclusions were drawn for 2D delamination in composite laminates in the presence of large-scale fiber bridging, according to the more recent works by Cameselle-Molares et al. [27–29] and the authors [30]. In these works, an experimental set-up similar to that in [26] was employed, where square plates were loaded transversely on both surfaces of the embedded circular pre-crack. It was found that the load continued to rise even after crack propagation, and more importantly, the 2D G_{Ic} value fitted by nonlinear numerical simulations was 40-50% higher than that from DCB experiments due to more extensive fiber bridging. In short, Ref. [26–30] are limited to pure Mode-I fracture conditions only. To the best of the authors' knowledge, no relevant literature covering the characterization of 2D Mode-II delamination is available.

This paper aims to experimentally investigate the 2D Mode-II delamination growth in composite laminates, especially in those exhibiting a large-scale fracture process zone (FPZ), and identify the similarities and differences with 1D cases represented by standard beam experiments. For this purpose, a novel experimental set-up was developed, where circular laminated plates with two different sizes of embedded circular pre-cracks were loaded transversely at the center while semi-clamped along the edge with free in-plane movement to achieve circular-symmetric Mode-II delamination

growth. The load, deflection and crack propagation were recorded throughout the experiments, with additional measurements from a 3D digital image correlation system (DIC) and fiber optics. A digital microscope was employed for post-inspection of the specimens to investigate the FPZ including large-scale fiber bridging and micro-cracking. The experimental results were further compared with 1D experiments on the same material using an ELS set-up.

3.2 Experimental program

3.2.1 Material description and specimen preparation

Both 1D and 2D experiments used specimens with the same laminate layup (Fig. 3.1a), which contained two types of reinforcements, i.e., long continuous filament mats (CFM) made of E-CR glass ("Electrical" grade "Corrosion Resistant" glass) with an area density of 600 g/m^2 and without binder or stitching (Fig. 3.1b), provided by Owens Corning, United States, and E-glass multidirectional (quadriaxial 0/±45°/90°) sewed fabrics (MD) with an area density of 800 g/m^2 (Fig. 3.1c), supplied by Swiss-Composite, Switzerland. Epoxy resin, SikaBiresin CR83, was selected as the matrix. The properties of the fibers and resin can be found in [27]. The combination of the chosen materials achieved good translucency allowing direct visual observation of the crack, which was particularly beneficial, given that non-destructive in-situ detection of delamination normally requires sophisticated devices and considerable effort [31]. The same CFM reinforcements were already used in previous investigations of 2D Mode-I delamination [27] due to several advantageous characteristics, e.g., their tendency to promote large-scale fiber bridging is likely to "augment" the 2D effects, while the in-plane isotropy reduces the complexity significantly. On the other hand, pure CFM laminates exhibit low stiffness and strength, which can lead to premature flexural failure under 2D Mode-II loading condition before adequate delamination growth. Therefore, compared to the CFM laminates investigated in [27], not only was the CFM ply number increased from 6 to 14, but the laminates were also reinforced by six MD layers, three on each side. Adjacent MD layers were rotated by 22.5° to achieve a quasi-isotropic layup, as shown in Fig. 3.1a. The asymmetric layup of the sub-laminates in delaminated specimens may have enlarged the mismatch between the curvature of the two crack surfaces and thus introduced a small amount of opening at the crack tip, but the resulting Mode-I component was considered to be insignificant and neglected in

this work. Apart from the main experimental program, tensile and double beam shear tests [32,33] were additionally designed for a CFM laminate with six layers and an MD laminate with four layers to assess the corresponding material properties. The resulting engineering elastic constants and the fiber volume fractions, V_f, for both laminates are summarized in Table 3.1, and the remaining values (marked with a superscript) were calculated using equations in [27].
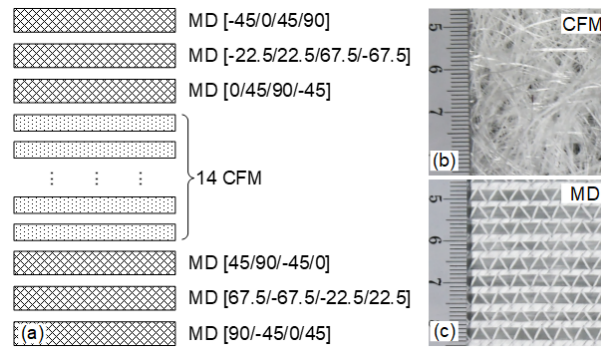
Fig. 3.1. Material description: (a) laminate layup, (b) continuous filament mat and (c) multidirectional sewed fabric.

Table 3.1. Engineering elastic constants of laminates.

Reinforce-ment type	V_f (%)	E_1 (GPa)	E_2 (GPa)	E_3 (GPa)	v_{12} (-)	v_{13} (-)	v_{23} (-)	G_{12} (GPa)	G_{13} (GPa)	G_{23} (GPa)
CFM	28.04	11.83	11.83	6.10[a]	0.33	0.30[a]	0.30[a]	4.45[a]	0.62	0.62
MD	44.90	18.23	18.23	8.96[a]	0.32	0.32[a]	0.32[a]	5.36[a]	1.97[a]	1.97[a]

[a] Theoretical values calculated from equations in [27].

All laminates were manufactured using a vacuum infusion process and cured under vacuum at room temperature for at least 16 hours, followed by post-curing at 70°C for eight hours. For the laminates containing CFM and MD, a pre-crack was introduced at the mid-plane by placing a 13-μm-thick Teflon film of a particular shape (rectangular and circular for 1D and 2D experiments respectively) in the middle of the reinforcements during the layup process. The edge of the films (and center for the circular ones) were marked in red to be visible after fabrication. All specimens were cut from the laminates using a waterjet, dried in an oven to fully evaporate the residual water, and left in room condition for cooling down.

The 2D experiments contained eight circular specimens with a radius of 180 mm concentric to the pre-crack, sorted into two groups. As shown in Table 3.2, the first group comprised five specimens with the pre-crack length (radius) a_0=40 mm (CP40-1 to 5), while the second three specimens with a_0=80 mm (CP80-1 to 3). The laminate thickness varied from 14.99 to 17.24 mm. Examples of the two specimen groups can be seen in Fig. 3.2.

Table 3.2. Specimen list and result summary of 2D delamination experiments.

| Specimen	Thickness	Crack initiation		Ultimate state[a]		Final delamination	
		Deflection	Load	Deflection	Load	Area	Symmetry ratio
	(mm)	(mm)	(kN)	(mm)	(kN)	(mm^2)	(-)
CP40-1	16.92	3.4	23.1	16.7	92.2	38015	0.64
CP40-2	16.77	3.0	20.0	16.8	91.9	34245	0.70
CP40-3	14.99	2.9	16.9	16.2	90.5	35195	0.92
CP40-4	16.57	3.0	20.5	17.6	93.2	46810	0.81
CP40-5	16.01	2.7	19.2	15.4	87.9	34609	0.91
CP80-1	15.79	3.1	15.1	16.4	93.4	35735	0.89
CP80-2	17.24	3.1	19.1	15.3	95.8	32123	0.92
CP80-3	17.21	3.5	19.8	14.8	90.1	38362	0.84

[a] The state when ultimate load was reached.
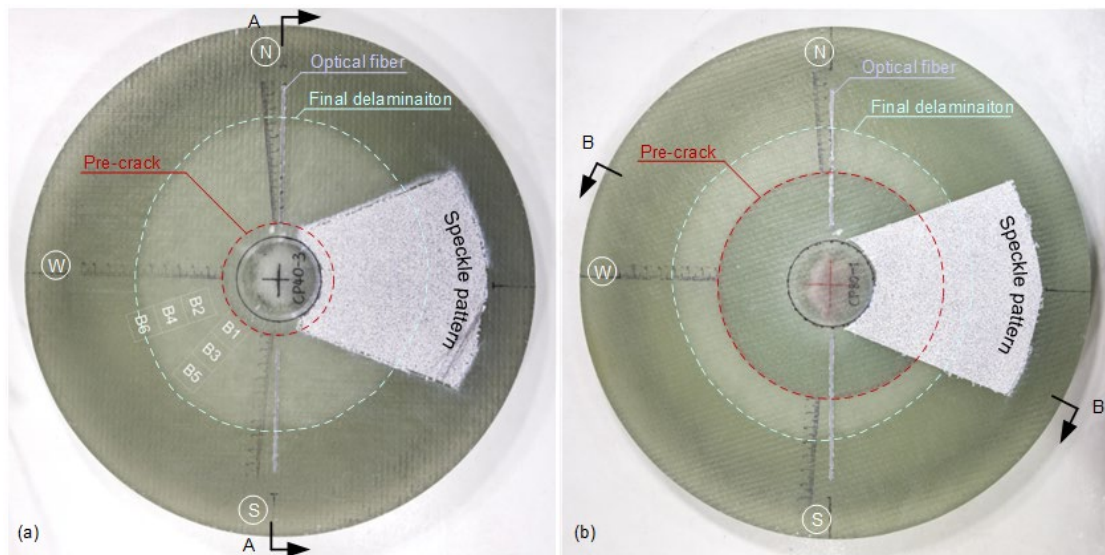
Fig. 3.2. 2D specimen description and final delamination patterns of specimens: (a) CP40-3 and (b) CP80-1.

The 1D experiments contained five specimens, labelled EM1 to EM5, plus another beam dedicated to clamp calibration [5]. Their length, width and average thickness were 240, 40 and 18.10 mm respectively. The free beam length was 150 mm including a_0=79 mm (measured from the loading line). An L-shaped aluminum tab was bonded to the specimen surface by Sikadur 330 epoxy adhesives with 1-mm thickness to hold the pinned loading block.

3.2.2 Experimental set-up

3.2.2.1 2D experiments

The 2D experiments were performed on a Zwick 500-kN universal testing machine in laboratory conditions (23 ± 5 °C and 50 ± 10% RH) with a specially designed fixture. Fig. 3.3 shows the experimental set-up and instrument layout. The circular specimens were placed concentrically between two steel ring-shaped frames and semi-clamped using eight screws of Ø16 mm, each with 20-N·m torque. As shown in Fig. 3.3b, the inner radius of the upper frame was 150 mm, while that of the lower was 145 mm plus a fillet with a radius of 5 mm along the upper edge, forming a 150-mm support radius. The term "semi-clamped" here refers to the specific boundary condition of the specimens, i.e., the vertical movement and rotation of the plate edge were constrained by the frames, while the in-plane deformation was released, in contrast to a fully clamped condition. This was achieved by placing a ring-shaped Teflon film of appropriate size, with graphite lubricant applied on both sides, between the two pairs of contact surfaces of the plate and frames to create nearly frictionless contact (see Fig. 3.3b). Then, the clamping frames with the specimen were placed on the machine and aligned to the loading axis. A steel cylinder with a radius of 25 mm was installed on the loading head of the machine to transfer the load. To reduce stress concentration and avoid punching shear failure for the specimens, the bottom of the cylinder was machined into a spherical surface with a radius of 300 mm, which had been determined according to the curvature of the plate's top surface at a 10-mm displacement through a preliminary finite element simulation. Additionally, a 3-mm-thick rubber pad with a radius of 30 mm was placed between the cylinder and the specimens to further distribute the pressure. The high friction from the rubber also constrained the specimens at the center, preventing horizontal shifting during loading. Overall, the boundary condition of a 2D specimen in radial directions resembled that of an ELS specimen, i.e., both specimens were loaded at the delaminated end (plate center) and could slide at the other

end (plate edge). However, rotation was not allowed at the plate center due to the material continuity and symmetry, whereas the pinned loading block allowed free rotation in ELS experiments.
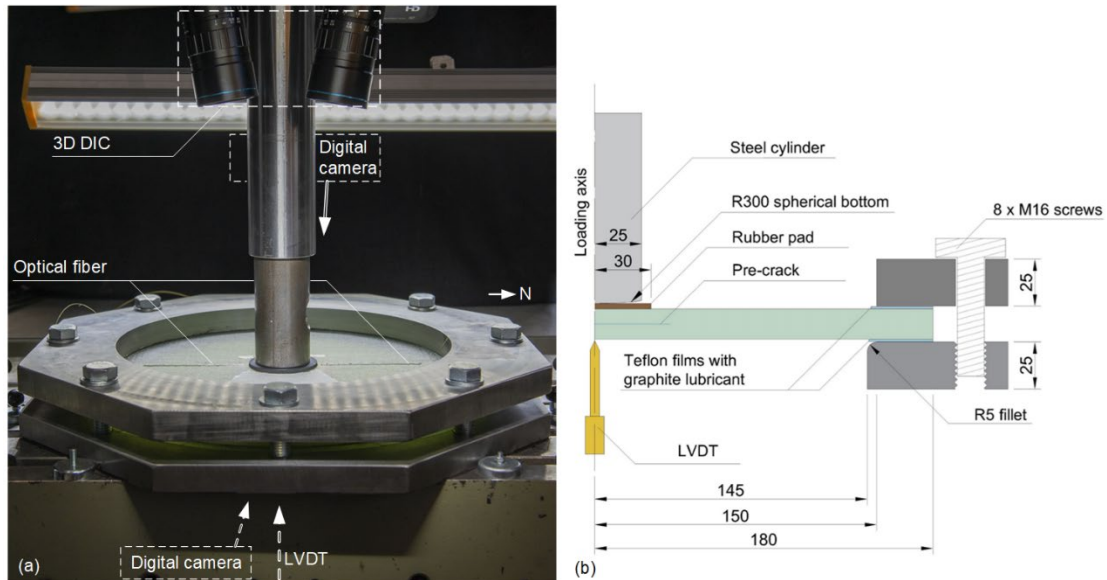
Fig. 3.3. Experimental set-up for 2D delamination: (a) photograph; (b) schematic profile (unit: mm).

The specimens were loaded under displacement-control at a rate of 1 mm/min, with the load and displacement recorded by the machine at a frequency of 2 Hz. To obtain the true displacement excluding the deformation of the rubber pad, a Linear Variable Differential Transducer (LVDT) was placed below the specimen measuring the central deflection (hereafter referred to as "deflection" unless otherwise specified). The delamination growth was filmed by a digital video camera fixed above the specimens in the west ("W"). In the monitored region, three rulers starting from the pre-crack front were stamped on the plate surface along the W, north and south ("N" and "S" directions, with a slight rotation towards the W of ~5°, see Fig. 3.2). After the experiments, the crack lengths, a, in the corresponding directions were read every few millimeters of propagation from the video frames, thanks to the fact that the originally translucent laminates became white after delamination, and then correlated with the loading data. The precision of the visual measurement of a was ±0.5 mm, according to the comparisons between 10 direct measurements of the delamination on the specimens' diametric sections (waterjet cut after loading) and corresponding visual observation

from above. However, the final precision was estimated to be reduced to ±1.0 mm due to the parallax error introduced during video recording (although compensated during geometric analyses). In addition to the aforementioned instrumentation, a 3D Digital Image Correlation System (DIC) was installed above the east sector. The area of interest on the top surface was painted white and sprayed with a random black speckle pattern (see Fig. 3.2), which however also blocked the visual observation of the delamination below. The images for the DIC analyses were acquired at a frequency of 0.2 Hz and post-processed in the Vic-3D software from Correlated Solution Inc to obtain deformation measurements of the top surface, and the radial displacement near the upper frame (i.e., relative slippage between specimens and frames) was extracted to confirm the frictionless sliding as assumed in the semi-clamping boundary condition. Furthermore, an optical fiber was bonded to the top surface of the specimens along the N-S direction, using Sikadur 330 epoxy adhesive of 1 mm in thickness and 2 mm in width (see Fig. 3.2), and then connected to the Luna Optical Distributed Sensor Interrogator (ODiSI) system to measure the radial strains with a pitch of 0.65 mm. Finally, another digital video camera was placed below the specimens to record the potential flexural damage propagation at the bottom center.

Prior to the main loading process, an in-situ debonding procedure was performed to separate the Teflon film from the sub-laminates to create a proper pre-crack, although without propagation (in contrast to the normal "pre-cracking" procedure suggested in the ELS test standard [5]). The specimens were loaded under displacement-control at a rate of 1 mm/min until a sharp drop in the load occurred at a deflection of less than 2 mm, accompanied by a clear sound denoting the sudden separation. After unloading, the main loading process started immediately.

3.2.2.2 1D experiments

The 1D experiments were performed in an ELS set-up using a W+B 250-kN universal testing machine (calibrated to 10% of its maximum capacity, i.e., 25 kN) under displacement-control at a rate of 1 mm/min in the same laboratory condition as the 2D experiments, see Fig. 3.4. The 1D specimens exhibited a high thickness-to-length ratio and an asymmetric layup of the sub-laminates, which were essentially not standardized ELS specimens but rather followed comparable dimensions to the 2D specimens with a_0=80 mm for comparison (similar a_0 and thickness, the same free beam length/support radius). The pre-crack interface was manually separated (i.e., debonding of the Teflon

film) before loading. One lateral surface of the specimens was stamped with rulers along the delamination path and monitored by a digital camera with a photographic frequency of 0.2 Hz during the experiment. Additionally, another ruler was stamped on the top surface of the specimens, and a digital video camera was employed to film the delamination process from above. The photos and videos obtained were correlated with the loading data during post-analyses and used for recording the change of *a* visually.
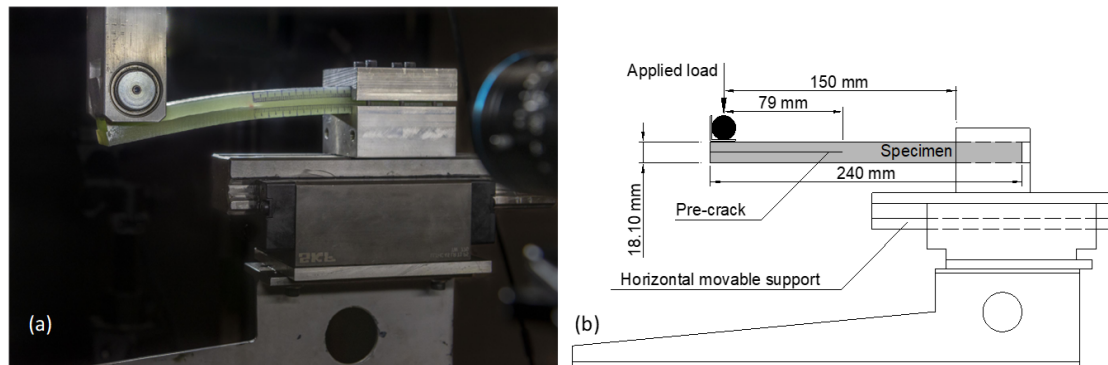

Fig. 3.4. Experimental apparatus for 1D delamination: (a) photograph; (b) schematic.

3.3 Experimental results

3.3.1 Results from 2D experiments

3.3.1.1 Failure mode and delamination pattern

An example of the 2D specimens after loading is presented in Fig. 3.5. All plate specimens failed in flexure due to progressive damage at the center of the bottom surface caused by increasing tensile stresses (see Fig. 3.5b). The experiments were continued while the flexural failure extended. Shortly afterwards, a sharp drop in load occurred, denoting a secondary failure mechanism, and the experiments were stopped. Two representative specimens of the corresponding groups, CP40-3 and CP80-1, were additionally selected and cut diametrically (along the A-A direction in Fig. 3.2a and the B-B direction in Fig. 3.2b) for failure inspection. Similar failure modes could be observed in both specimens, see Fig. 3.6 ($\Delta a = a - a_0$ being the crack length increments), i.e., flexural failure in the lower sub-laminate and shear failure in the upper one. The whole failure process can be explained as follows: tensile damage initiated and accumulated at the bottom center during bending and finally led to rupture of the lowermost MD layers. As the flexural failure extended in both the size and depth dimensions, the stresses near the center redistributed. Finally, the shear stresses in the

upper sub-laminate (larger than those in the lower sub-laminate due to the shear stress distribution in the thickness direction) exceeded the strength, resulting in a sudden shear failure. Before the lowermost layers failed, the effects of the tensile damage on the overall structural response and delamination growth were confirmed to be insignificant by the monitoring videos and DIC results. As a result of the efforts made to avoid stress concentration, only minor local damage could be found at the periphery of the loading zone on the top surface as well as at the circle line on the bottom surface in contact with the lower frame.
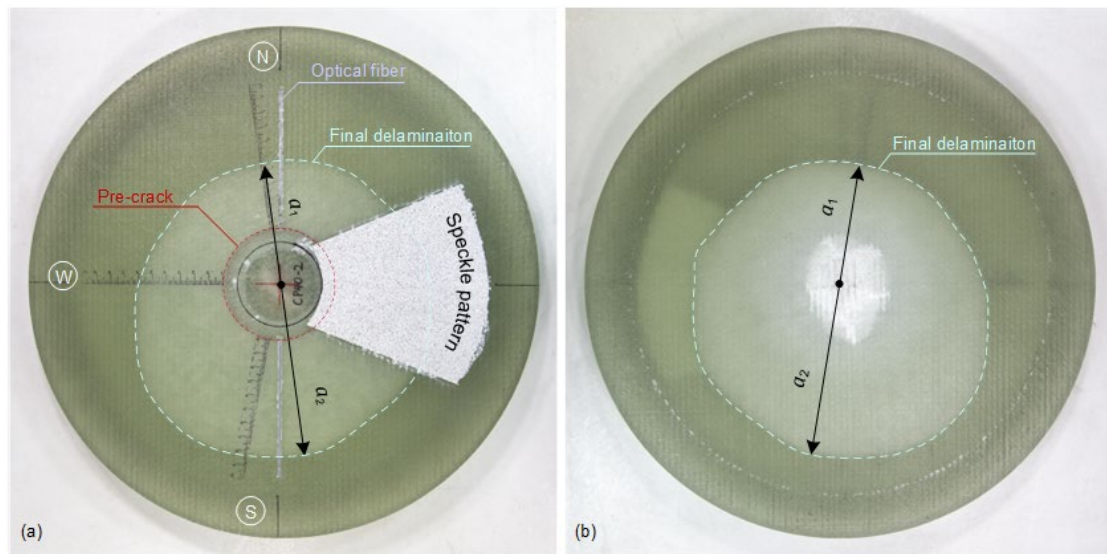

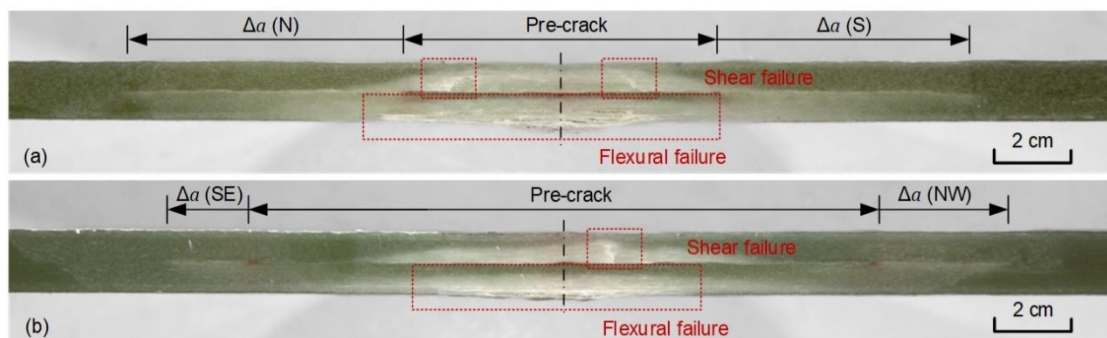Fig. 3.5. Delamination pattern and failure mode of CP40-2: (a) top view and (b) bottom view.

Fig. 3.6. Diametric sections after loading: (a) A-A section of specimen CP40-3 and (b) B-B section of specimen CP80-1.

In general, the main delamination grew in all directions in the mid-plane as expected, except in some cases where the crack kinked into adjacent layer interfaces

after the flexural failure, e.g., in the last centimeter of propagation in the S direction in CP40-3 (Fig. 3.6a). Although the experimental set-up was aligned as concentrically as possible, the pattern of the final delamination, defined as the delamination after the whole loading process, still showed a certain degree of asymmetry in many specimens (e.g., specimen CP40-2 in Fig. 3.5). Indeed, the 2D experiments were highly sensitive to asymmetric loading conditions, which could be introduced by several factors, such as eccentric loading, instability of the rubber pad, uneven friction in the clamping area and material inhomogeneity, etc. In order to quantify the symmetry level of the final delamination, the ratio between a diametric pair of crack lengths was examined for all directions, and the lowest one was designated the "final delamination symmetry ratio", e.g., a_1/a_2 for specimen CP40-2 in Fig. 3.5 (note that the chosen diametric directions did not necessarily lie on any of the previously monitored directions). The obtained value for each specimen is listed in Table 3.2, together with the final delamination area (including the pre-crack), calculated from the specimen photos taken after the experiments in Adobe Photoshop. As can be seen from the table, all plates exhibited substantial delamination growth and reached similar delamination areas despite different symmetry ratios and pre-crack radii, except for specimen CP40-4, whose delamination area was significantly larger.

3.3.1.2 Load, deflection and crack length

Table 3.2 summarizes the experimental results for each specimen, including the deflection at crack initiation (average value from the three ruler directions, N/W/S) and the corresponding load (hereafter referred to as "initiation deflection" and "initiation load"), as well as the ultimate load and the corresponding deflection (hereafter referred to as "ultimate deflection", with the corresponding state of the plates defined as the "ultimate state"). The load-deflection curves for both specimen groups are presented in Fig. 3.7, showing a continuously rising trend in general, with the peak marking the flexural failure described above. Note that the sharp drops at the ends of the curves were removed. For the specimens with a smaller pre-crack (Fig. 3.7a), the curves present only little scatter except for specimen CP40-3 (the thinnest one), which exhibited lower stiffness overall. In this group, the load increased almost linearly with deflection up to 10-12 mm despite crack initiation and certain propagation. After this point, the loads continued rising but with a reduced slope, although slight fluctuations can be observed in each curve. For the specimens with a larger pre-crack (Fig. 3.7b),

the load increased nonlinearly with the deflection up to ~90 kN, revealing a stiffening phenomenon. Although the crack initiated and propagated during this period, no deterioration of the structural performance was reflected in the load-deflection curves. Subsequently, the specimens also underwent a stiffness drop, followed by failure.
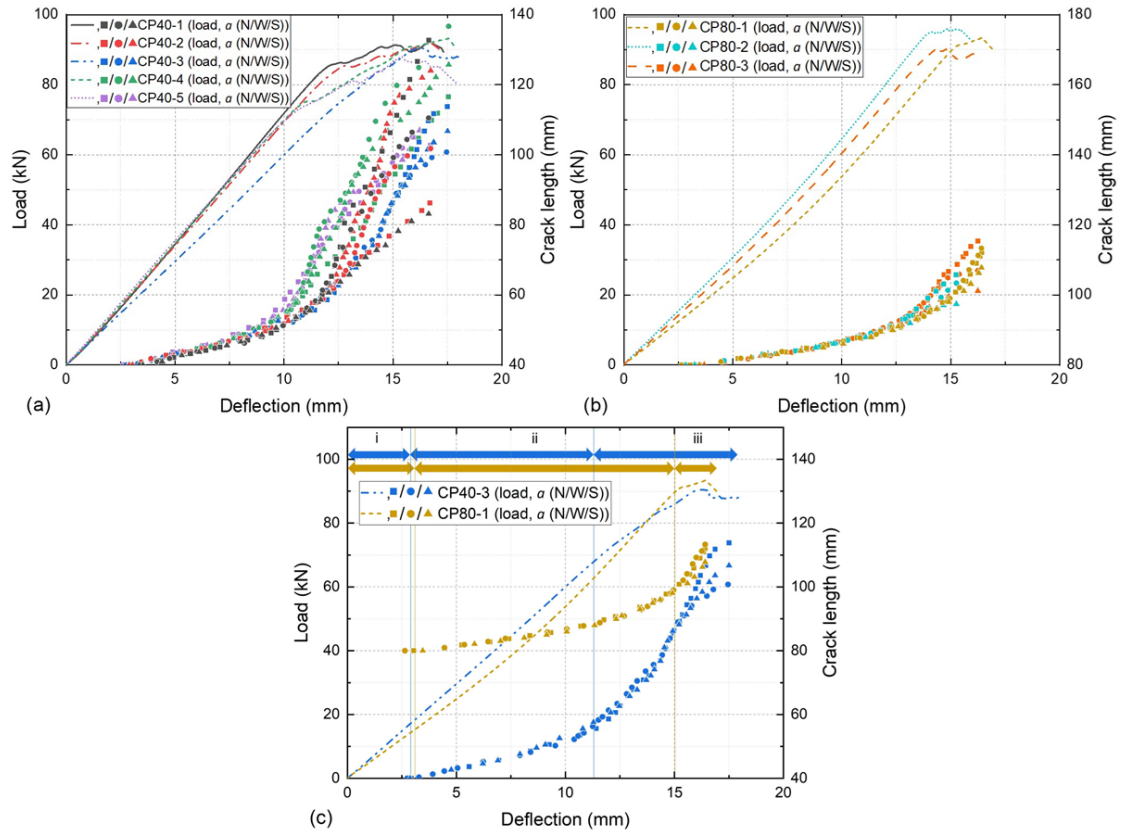
Fig. 3.7. Load and crack length vs deflection curves for (a) specimens with pre-crack radius of 40 mm, (b) specimens with pre-crack radius of 80 mm and (c) specimens CP40-3 and CP80-1.

The recorded crack-length measurements in the N/W/S directions for each specimen were also plotted in Fig. 3.7. A two-segment trend can be observed in the first group (Fig. 3.7a). Specifically, the cracks propagated relatively slowly at first for about 17 mm, after which the propagation rate increased rapidly. Although the crack-length plots of the second segment lie in a wide band due to the different deflections at which the plots turn (i.e., smallest for CP40-4 and 5, then CP40-1 and 2, and largest for CP40-3) as well as the asymmetric delamination growth, similar slopes (i.e., propagation rates) can be noted. In addition, good symmetry was generally presented in the beginning, as the crack-length plots from the three directions for each specimen nearly overlapped.

Asymmetry arose either soon after the rapid propagation (CP40-1, 2 and 4) or when approaching the ultimate state (CP40-3 and 5). For specimens of the second group (Fig. 3.7b), due to limited extent of delamination growth, only the first segment can be identified in the crack length-plots. Good symmetry was also presented initially, and then decreased before failure.

For comparison, the load and crack-length results from specimens CP40-3 and CP80-1 (symmetric cases of the corresponding groups) were displayed together in Fig. 3.7c. Although the specimens experienced different loading history and energy dissipation during delamination growth due to different pre-crack sizes, comparable ultimate loads and deflections were achieved. Furthermore, the two sets of crack-length plots tended to converge at the end, approaching similar delamination sizes and growth rates. According to the general delamination growth behavior, three stages can be defined for both groups, i.e., (i) crack initiation, (ii) slow propagation (corresponding to the first segment in the crack-length plots) and (iii) rapid propagation (corresponding to the second segment in the crack-length plots). In stage (i), the crack was in the initiation phase; in stage (ii), the crack propagated in a relatively slow but increasing rate for a certain length (~17 mm and ~19 mm in specimens CP40-3 and CP80-1 respectively), without obvious deterioration (i.e., softening) in the structural performance; in stage (iii), the crack propagation rate further increased, approaching a constant value, while the plate stiffness decreased notably until final failure. Although the cracks initiated in the specimens at similar deflections, the extent of deflections achieved in the subsequent stages differed significantly according to the pre-crack sizes. To be specific, specimen CP40-3 exhibited overall faster crack propagation and entered stage (iii) at a smaller deflection, and consequently, stage (ii) and (iii) constitute comparable proportions of the loading process. In contrast, in specimen CP80-1, stage (ii) contributed to the major portion, since it required much larger deflection to achieve a similar length of crack propagation (i.e., ~19 mm) before entering stage (iii). Indeed, the larger pre-crack radius and thus perimeter necessitated much more energy for early crack propagation in specimen CP80-1 than CP40-3.

3.3.1.3 Compliance and stiffness variation

Specimens CP40-3 and CP80-1 were selected to investigate the changes in structural compliance, calculated as the deflection (δ) over the load (P), as a function of the delamination area (including the pre-crack area), derived from the average crack length

in the three ruler directions by assuming a circular delamination shape throughout the loading process, see Fig. 3.8. For both specimens, the compliance fell to a low point and then rose continuously. The last segment of the curve for specimen CP40-3, which ascended steeply after 30000-mm^2 crack area, corresponded to the asymmetric delamination growth near ultimate state. Most importantly, the low points were found to mark the transition from stage (ii) to (iii) defined in the previous section. As mentioned above, similar lengths of crack propagation (i.e., Δa) were reached for both specimens in stage (ii). Thus, considering the pre-crack radii, stage (ii) only comprised a small proportion of the whole crack-area increase in specimen CP40-3, whereas in specimen CP80-1, most of the area was generated during this stage.
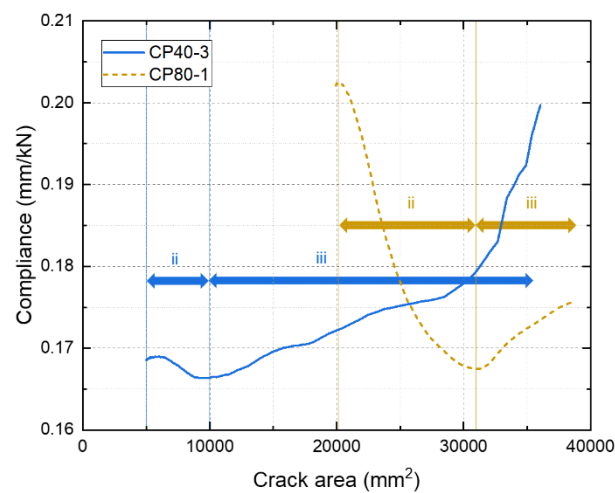

Fig. 3.8. Compliance vs crack area curves for specimens CP40-3 and CP80-1.

The variation in the compliance was a result of competition between the stiffening mechanism, i.e., stretching, and the softening mechanism, i.e., delamination growth. Stretching, which creates extra membrane forces in the plates and increases the flexural stiffness, is a typical 2D nonlinear phenomenon that cannot be ignored during analyses if the deflection is more than 0.2 times the thickness [34]. For the experiments investigated here, stretching was induced in the plates during bending, since the inward movement of the outer part of the plate was limited by the associated circumferential compression effect, making the outer part act like a frame, which constrained the in-plane deformation of the inner part and introduced radial tensile stresses. As the loading proceeded, the stiffening effect from stretching intensified due to increasing deflections, while the softening also increased due to the delamination growth. During delamination

growth however, additional resistant mechanisms, namely resin plastic deformation, microcracking (oriented 45° from the main delamination path near the tip) and fiber bridging, were activated, which tended to weaken the softening effect. In particular, fiber bridging is known for its geometric dependency, and contributed to the increase of SERR for 2D Mode-I delamination compared to 1D cases [30].

For a better understanding of the stiffness variation, the tangent stiffness, calculated as $dP/d\delta$, was plotted against deflections for all specimens from both groups in Fig. 3.9. The three stages defined before were also marked in the figure for specimens CP40-3 and CP80-1 for reference. For specimens with smaller pre-crack (Fig. 3.9a), the stiffness under crack initiation fluctuated due to the initial readjustment between the specimen and the loading system. During stage (ii), the increase in the extent of stretching and the amount of delamination growth reached a balance, leading to a nearly constant stiffness value. Then in stage (iii), the effect of the softening mechanism prevailed due to the accelerated propagation rate, causing a significant decline in stiffness, followed by large fluctuations in each curve. Specimens with larger pre-crack (Fig. 3.9b) exhibited similar behavior in stages (i) and (iii). In stage (ii), however, a rising trend was presented in the stiffness curves, as the softening effect from the much slower crack propagation was not comparable to the stiffening from stretching.

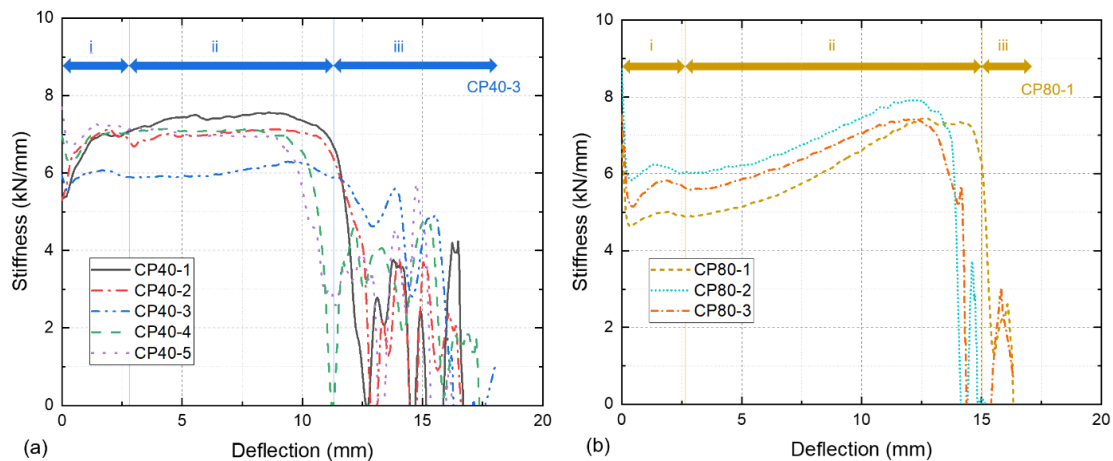Fig. 3.9. Tangent stiffness vs deflection curves for specimens with a pre-crack radius of (a) 40 mm and (b) 80 mm.

3.3.1.4 Delamination inspection

In order to carry out direct observation of the FPZ in 2D experiments, six small rectangular samples, measuring 2 cm × 2 cm each, were waterjet cut from the

delaminated region of specimen CP40-3 (see Fig. 3.2a) through the whole thickness and subsequently conditioned in an oven to evaporate the residual water. The nomenclature of the samples indicates the distance from the center of the sample to the pre-crack perimeter, e.g., sample B2 was 2 cm away. Surprisingly, none of the samples was split completely into two pieces, indicating the presence of a long FPZ. Indeed, even the crack surfaces of sample B1, which was ~5 cm (calculated from the sample center) behind the final delamination front, were still bridged by single fibers, implying that the FPZ measured at least 5 cm in length. The lateral surfaces of the samples (i.e., radial sections) were then examined under a Keyence VHX-2000 digital microscope. During the inspection, samples B1 to B3 were fixed onto a small fixture and opened in a controlled way for ~1 mm to investigate the fiber bridging condition, while samples B4 to B6 were kept in their original condition, since the sub-laminates were connected too firmly to be opened manually.

The delamination condition in each sample is presented in Fig. 3.10, obtained by 3D stitching of several microscopic images using a dynamic focus depth to achieve a larger depth of field. Note that Fig. 3.10f does not show the exact crack "tip" but rather several millimeters behind, since the vicinity of the tip was whitened due to micro-scale damage, hindering the inspection at this magnification. As shown in the first three images in Fig. 3.10, towards the crack tip, the surfaces were gradually bridged by individual fibers, partially broken fiber bundles and less damaged fiber bundles. In addition, rough delamination surfaces could be observed, with numerous broken fibers protruding from the matrix. Closer inspection revealed that a large number of fiber bundles in circumferential directions lay across the crack path as a result of ply nesting, which acted as a crack-arrest mechanism and sometimes caused local branching (Fig. 3.10d and e). Ply nesting is a phenomenon in fiber laminates where yarns of one ply lie in the valleys formed by yarns of adjacent plies, which is more pronounced in CFM laminates due to the special fiber architecture. It can reduce the extent of the resin-rich zone between plies [35] and improve the macroscopic roughness, yielding higher fracture resistance [36]. When moving closer to the tip, hackles oriented ~45° from the main delamination plane could be identified (Fig. 3.10e and f), implying the formation of microcracks during the fracture process [37]. In this work, the microcracking zone, which spanned at least several hundred μm according to the hackle pattern shown in Fig. 3.10f, was considered to be located behind the crack tip, since the material properties within the region were significantly reduced. Even though microcracks being

considered part of the true crack length is controversial [38], they have been included in the visual measurement of *a* in this work because of their whitening effect.
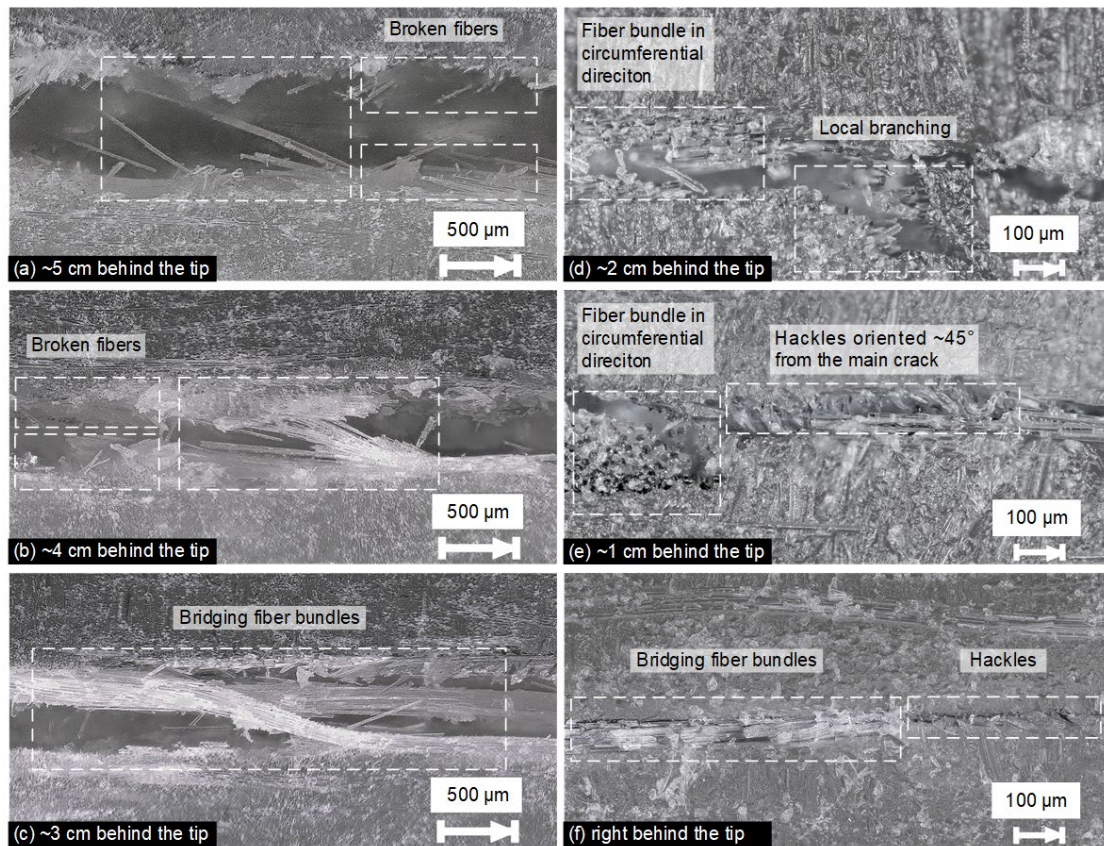

Fig. 3.10. Delamination in specimen CP40-3: samples (a) B1, (b) B2 and (c) B3 with an opening of ~1 mm; samples (d) B4, (e) B5 and (f) B6 in the original conditions (arrows on scales pointing at crack front).
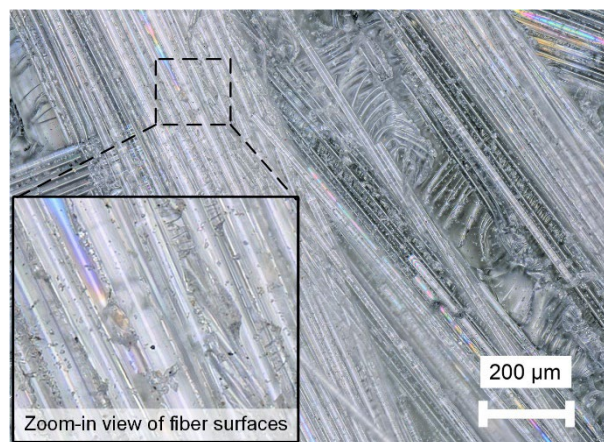

Fig. 3.11. Delamination surface of sample B3.

After inspection of the lateral surfaces, one of the two pieces of sample B3 was manually separated for inspection of the delamination surface using the same method described above, see Fig. 3.11. The ply nesting phenomenon could be clearly identified here, with fiber bundles located in different depths and directions. In addition, the minimal amount of plastically deformed resin on the fracture surface indicated a weak fiber/matrix interface, thus implying a smaller contribution from resin plastic deformation to the total SERR but a greater one from fiber bridging [39], in contrast to the findings in [40] based on ELS specimens made from carbon-fiber/polymer unidirectional composites.

3.3.2 Results from 1D experiments

3.3.2.1 Load, displacement and crack length

The original data for the 1D experiments are available on Mendeley Data [41]. The load-displacement and crack length-displacement responses are presented in Fig. 3.12. Similar to those of the 2D experiments, the crack-length plots exhibited a two-segment behavior. In fact, such behavior is common in various laminates but not usually revealed nor discussed in the literature. Nevertheless, by plotting the crack-length increment against the displacement, e.g., using the ELS experimental data from Ref. [38,40], the two-segment behavior can also be obtained in unidirectional carbon-fiber laminates [40] as well as epoxy-paste and epoxy-film adhesively bonded joints [38].

The three stages defined in section 3.1.2 are still visible in the 1D experiments. During the slow crack propagation stage, the load increased with a decreasing slope, since there was no stretching to counteract the softening mechanism (i.e., delamination growth). The loads reached a peak after ~10 mm of crack propagation (to 89 mm), marking the onset of stage (iii). The delamination growth accelerated notably in stage (iii), becoming unstable in some specimens (i.e., in EM2, EM4 and EM5 from around a=91 to 119 mm) and causing a sharp drop in the load. After the crack neared the clamping boundary, the crack-growth rate slightly decreased, while the load reduction was more moderated. In general, stages (ii) and (iii) constituted similar proportions of the whole loading process, with most of the delamination area being generated in the last stage.
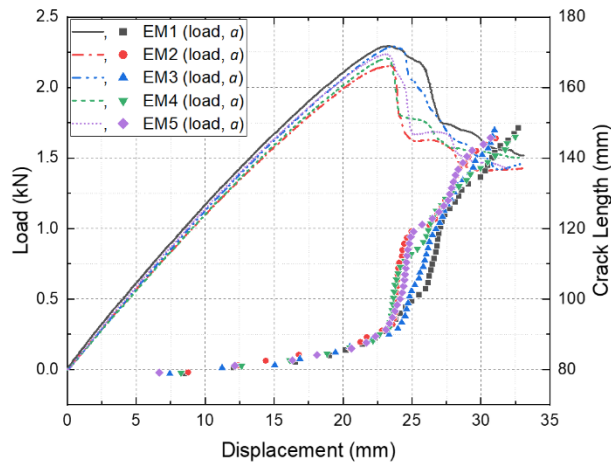
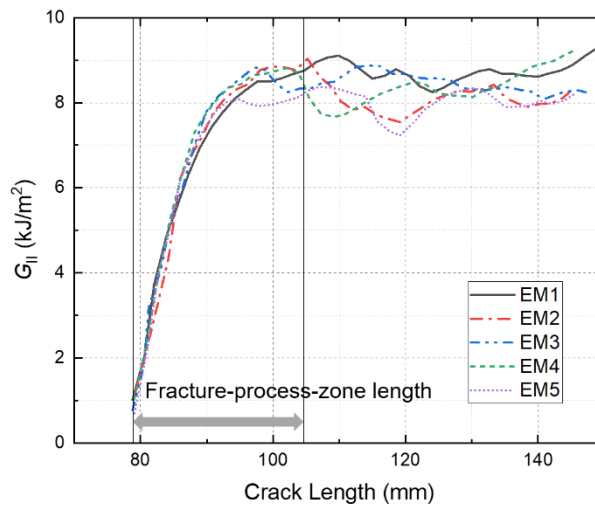Fig. 3.12. Load and crack length vs displacement curves for 1D specimens.

Fig. 3.13. R-curves of 1D specimens.

3.3.2.2 R-curve behavior

As discussed above, the investigated laminates exhibited a large FPZ, reducing the effectiveness of the available data reduction schemes for deriving G_{II} based on Linear Elastic Fracture Mechanics (LEFM) as discussed in [5]. The high thickness-to-length ratio and the asymmetric fiber layup of the 1D specimens would introduce even more errors in the calculations. Since this work did not aim for accurate estimation of the fracture resistance, for the sake of simplicity, the experimental compliance method (ECM) was still employed for qualitative analysis, with both large-displacement and loading-block correction factors [5] considered. The resulting R-curves are shown in Fig. 3.13. According to the figure, the crack initiated at a relatively small G_{II} value. As the crack propagated, G_{II} rose linearly at first and then increased with a decreasing slope

until reaching a plateau, corresponding to a full FPZ length of ~25 mm. The steady value of G_{II} was around an order of magnitude larger than the that for initiation and notably larger than published values for other glass fiber laminates, which typically vary between 1 and 3 kJ/m^2 [42, 43].
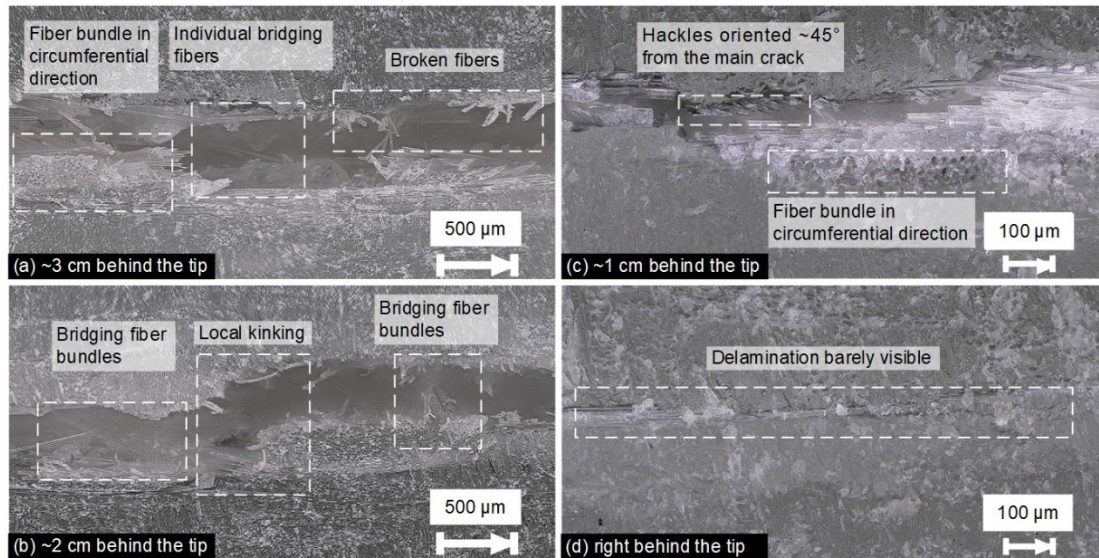

Fig. 3.14. Delamination in specimen EM2 at (a) ~3 cm and (b) ~2 cm behind the tip with an opening of ~1 mm, and (c) at ~1 cm and (d) right behind the tip in the original conditions (arrows on scales pointing at crack front).

3.3.2.3 Delamination inspection

A digital microscope was employed after the experiments to examine the FPZ. Through-thickness rectangular samples, measured 1.6 cm × 1.6 cm, were cut from specimen EM1 every one centimeter in two rows along the longitudinal direction. The two sub-laminates of the samples within 3 cm from the tip (measured from sample center) were still connected to each other, which agreed reasonably well with the FPZ length indicated in the R-curve (~25 mm). Furthermore, it was found impossible to manually separate the two sub-laminates of the samples located within 1 cm of the tip. Fig. 3.14 presents the images of the longitudinal delamination path in the samples spanning the FPZ, with two samples fixed on a fixture and opened for ~1 mm and the other two kept in the original conditions, depending on the traction between the delamination surfaces. Similar phenomena could be identified along the FPZ, as done in the 2D case. Fig. 3.14b additionally captured a local crack kinking phenomenon due to the circumferential fiber bundles on the delamination path. More fracture surface

area was generated by the local crack kinking and branching as well as the larger number of microcracks reflected by the dense hackles, which might have contributed to the large G_{II} values derived in Fig. 3.13.

3.4 Discussion

3.4.1 Fracture process zone

In the literature, the FPZ of delamination in fiber composites is normally divided into a relatively small tip zone and a long fiber bridging zone for analytical or numerical analyses such as cohesive zone modeling [9,39]. Such classification of the FPZ is however not appropriate in this work, since neither the onset of the formation nor the full development (only achieved in 1D experiments) of fiber bridging caused any notable changes in the load-deflection response or crack propagation rate during the loading process. Based on the observations from delamination inspection, the traction between the delamination surfaces was selected as a new criterion to divide the FPZ into two regions, i.e., a strong traction zone (STZ) near the crack tip and a weak traction zone (WTZ) at the wake. The former corresponded to the delamination states in the samples located within 2 cm behind the tip in specimen CP40-3 (samples B4, B5 and B6 in Fig. 3.10d, e and f) as well as those within 1 cm behind the tip in specimen EM2 (Fig. 3.14c and d), which included resin plastic deformation, microcracking and strong fiber-bundle bridging, preventing the delamination interface from macro-separation. The full development of the STZ was responsible for the transition from the slow crack propagation stage to the rapid propagation stage, similar to the phenomenon reported in [30], where the Mode-I crack-propagation rate rose after full development of the fiber-bridging zone. The radial length of the fully developed STZ could thus be determined by the crack-propagation length in the slow propagation stage, i.e., around 17 and 19 mm for 2D specimens with a pre-crack radius of 40 and 80 mm (Fig. 3.7), and 10 mm for 1D specimens (Fig. 3.12), respectively. These values agreed well with the distances from the tip within which no macro-separation on the delamination interface was observed, assuming that the length of a full STZ does not vary significantly with further delamination growth. On the other hand, the WTZ, which was comprised of bridging of partially broken fiber bundles and individual fibers, was not fully developed until the end of the 2D experiments. When the WTZ appeared at the back of the FPZ, the crack surfaces started to be separated, resulting in a decrease in

structural stiffness and an increase in crack propagation rate. As reflected in the trend of the crack-length plots in Fig. 3.7a, a constant propagation rate can be expected after full development of the whole FPZ in 2D delamination.

3.4.2 Effect of pre-crack size in 2D experiments

Initial qualitative comparisons of the effects of different pre-crack sizes on the final delamination area, initiation load and deflection, ultimate load and deflection as well as stiffness and compliance for 2D experiments were made in Section 3.1. Further quantitative examinations are presented in Fig. 3.15. According to Fig. 3.15a, doubling the pre-crack radius caused the crack to initiate at 7% larger deflection and 11% lower load due to the increase in the crack-front length and the decrease in initial stiffness (see Fig. 3.9). In terms of the ultimate state (Fig. 3.15b), the specimens with a larger pre-crack exhibited 6% smaller deflection and 2% higher load. Finally, a larger pre-crack resulted in a 6% drop in the final delamination area.

To explain the results, two ideal specimen cases are employed, i.e., Case 1 with a_0=40 mm and Case 2 with a_0=80 mm, which share the same parameters (material properties, thickness, etc.) except pre-crack radii and exhibit symmetric delamination growth until flexural failure. One important fact is that even if Case 1 is initially loaded until a=80 mm and then unloaded (i.e., pre-cracking), it is essentially still different from Case 2 due to the existence of the large-scale FPZ. The extra traction forces from the FPZ in the region where 40 mm<r<80 mm, r being the radial coordinate, will slightly strengthen Case 1 in the following loading process compared to Case 2, given that a full FPZ will not be achieved in either case even at failure according to Section 3.4.1. The monotonic loading process of Case 1 after a reaches 80 mm can be considered as a reloading process of the pre-cracked plate described above. Therefore, Case 1 will not fail with the same crack size as Case 2, since it will have to develop a larger crack to compensate the strengthening effect from the extra traction forces, which tends to redistribute the stresses in the plate towards a more favorable state. On the other hand, according to Fig. 3.7c, in order to reach any same crack-length value (a>80 mm) as Case 2, Case 1 should sustain larger deflection and load to close the gap in the pre-crack radius, which means even larger deflection and load is required to achieve the larger crack size at failure as demonstrated above. In summary, at ultimate state, the specimens with a smaller pre-crack are supposed to exhibit larger deflection, load and delamination area. The closer to full development of the FPZ at failure for both types

of specimens (by choosing stronger laminates to delay the failure, or introducing smaller pre-cracks to allow more propagation), the less pronounced the effect of different pre-crack sizes on the ultimate state is. Thus, the experimental results in Fig. 3.15b agree well with the above analysis, except for the ultimate load, which can be considered experimental scatter (the final delamination area is considered to follow the same rule of the area at ultimate state). Note the findings are only valid before a full FPZ is developed. Theoretically, after full development of the FPZ, the differences in the load-deflection response and delamination-growth behavior resulting from different pre-crack sizes will vanish, i.e., the two ideal cases will eventually become identical, as already reflected in the converging trends of the load-deflection curves and crack-length plots from the two specimen groups in Fig. 3.7c.
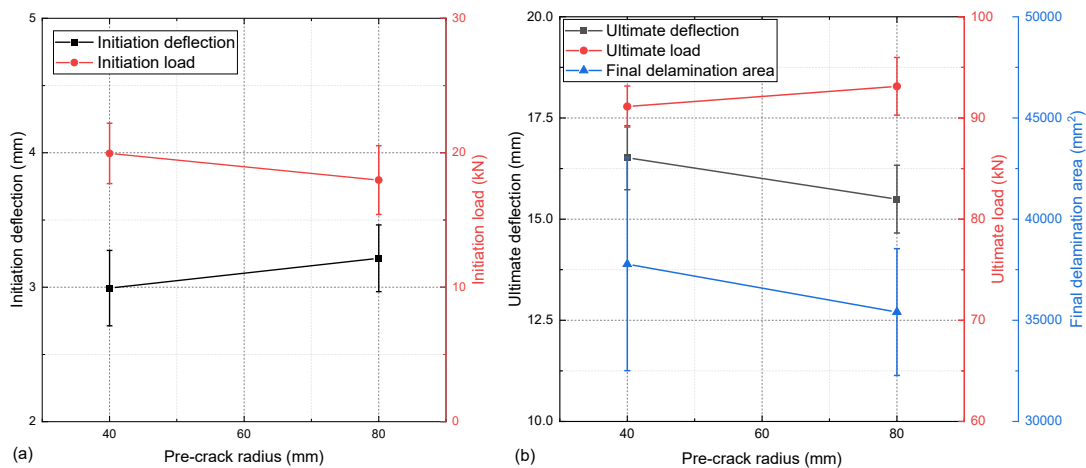

Fig. 3.15. Effects of pre-crack radius on (a) initiation load and deflection, and (b) ultimate load and deflection and final delamination area.

To estimate the effects of pre-crack sizes on the stress state during loading, the radial strains along the optical fiber in the N direction were extracted every 5-mm deflection for specimens CP40-3 and CP80-1, as shown in Fig. 3.16 (some signals were lost at higher loads). The bulges in the curves near the plate center indicate the delaminated region (including the pre-crack), while the flatter segments near the edge indicate the uncracked part. For both specimens, most regions of the top surface were radially under tensile condition, except the central part (not monitored), which was under compression, and the outer region near the boundary, where the tensile strains rapidly decreased to zero. In general, specimen CP40-3 exhibited lower radial strains

on the top surface of the upper sub-laminate, but higher strains on the top surface of the uncracked region. As the difference in crack sizes diminished with larger deflections, the peak strains in specimens CP40-3 and CP80-1 became comparable at the same deflection level (δ=15 mm). In summary, for the loading condition applied in this work, a larger pre-crack led to higher radial tensile strains on the top surface of the delaminated region near the crack front, but the difference turned to be insignificant after a certain extent of crack propagation.
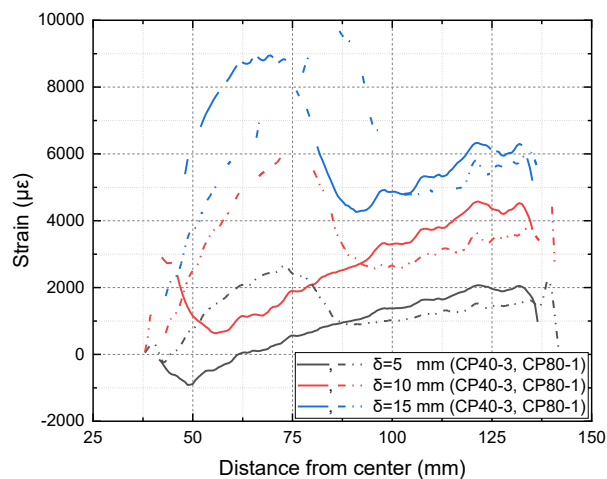

Fig. 3.16. Radial strains along optical fibers (N) at different deflections for specimens CP40-3 and CP80-1.

3.4.3 Comparison between 1D and 2D delamination

Although both types of the experiments exhibited delamination growth with slow and rapid propagation stages, the load decreased with further deflections in the rapid propagation stage in 1D experiments but continued to rise in 2D ones until reaching the ultimate state (Fig. 3.7 and Fig. 3.12). To exclude the effect of the increasing crack front in the latter cases, a normalization procedure was carried out on selected specimens, where the load was simply divided by the crack-front length, i.e., $2\pi a$ for specimens CP40-3 and CP80-1 and the beam width, b, for EM3 respectively, yielding the shear force per unit crack width, designated Q^*. The resulting Q^*, together with Δa, were plotted against deflections in Fig. 3.17. Thus, Q^* decreased in both 1D and 2D cases during rapid propagation of the crack, with the peaks marking the transitioning points from stage (ii) to (iii). Fig. 3.17 also revealed the significant difference in the slopes of the Q^*-δ curves of specimens CP80-1 and EM3 during the first two stages, given that both specimens had similar a_0 (80 vs 79 mm), support radius/free beam length (150

mm) and thickness (15.79 vs 18.10 mm). This was attributed to the 2D bending condition, the stretching and in particular, the continuity and symmetry condition in plate specimens, which provided extra moments at the plate center compared to the free end in beam specimens. Note the comparison here is limited to the overall structural response. Detailed fracture analyses in terms of SERR are needed with the help of additional tools, e.g., numerical simulations, in future works.
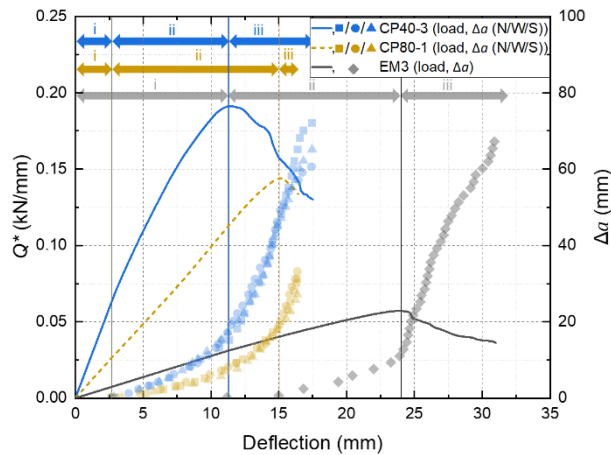

Fig. 3.17. Normalized load and crack length increments vs deflection curves for 1D and 2D experiments.

In terms of the delamination growth, the crack length developed during the slow propagation stage, i.e., the length of the STZ, differed notably between 1D and 2D specimens (~10 mm vs 17 to 19 mm). Furthermore, the whole FPZ was also found to be significantly shorter in the beams than in the plates (2.5 to 3 cm vs at least 5 cm). A similar conclusion for Mode-I delamination was drawn in [28], but the effect was less significant (10 mm in beams vs 13.2 mm in plates). The differences in the lengths of the STZ and the whole FPZ were attributed to the different boundary conditions of the sub-laminates as well as the stretching in 2D experiments. Specifically, from the crack tip to the plate center, the relative slippage, i.e., the Mode-II crack separation, in 2D cases increased from zero to a maximum and then decreased to zero again due to the continuity and symmetry condition, whereas it increased monotonically towards the free beam end in 1D cases. A significantly longer distance from the tip was therefore needed for plate specimens to reach the same amount of separation for a certain fracture process state. In addition, the stiffening effect from stretching in plate specimens could

necessitate larger separation to reach a full FPZ, as reported in 2D Mode-I delamination [28], which tended to increase the length of the FPZ even further.

3.5 Conclusions

The 2D delamination growth in composite laminates with in-plane isotropy under Mode-II fracture condition was experimentally investigated based on a novel set-up. Eight plate specimens with two sizes of pre-cracks were loaded transversely up to flexural failure while being semi-clamped along the edge. The load-deflection response, delamination growth pattern, compliance and stiffness changes and fracture process zone were discussed. Furthermore, 1D experiments using an ELS set-up were performed on beam-like specimens of the same material for comparison. The following conclusions are drawn:

- The crack propagation in both 1D and 2D experiments showed a two-segment behavior, i.e., following initiation, the crack propagated relatively slowly with respect to the increase in deflection (the first segment), and after a certain length of propagation, the rate accelerated obviously (the second segment).

- The whole loading process could be divided into three stages based on the crack propagation behavior, i.e., crack initiation (from the start of loading to the accomplishment of crack initiation), slow propagation (the first propagation segment) and rapid propagation stages (the second propagation segment). For 1D specimens and the 2D ones with a smaller pre-crack, the slow and rapid crack propagation stages exhibited comparable proportions during the whole loading process, and most of the delamination area was generated during the last propagation stage; while for the 2D specimens with a larger pre-crack, the slow crack propagation constituted the major proportion of the whole loading process, and similar amounts of delamination area were created in the slow and rapid crack propagation stages.

- For 2D specimens, the load increased with constant or increasing stiffness, depending on the pre-crack size, during the first two stages, and then continued to increase with reduced stiffness in the last stage as the softening mechanism, i.e., delamination growth, prevailed over the stiffening mechanism, i.e., stretching. For 1D specimens, in contrast, the load initially increased with dropping stiffness and then decreased in the last stage. By plotting the shear

force per unit crack width, instead of the total load, against deflection, similar dropping trends in the curves could be obtained for both 1D and 2D experiments.

- Matrix plastic deformation, hackles reflecting microcracking and fiber/bundle bridging could be identified from the large-scale fracture process zone. The fracture process zone could be further divided into a strong traction zone near the crack tip, where the crack surfaces were firmly connected by plastically deformed or microcracked resin and intact fiber bundles, and a weak traction zone, where the crack surfaces were separated but bridged by partially broken fiber bundles and individual fibers. The full development of the former zone was responsible for the transition from slow to rapid crack propagation mentioned above. The strong traction zone and the whole fracture process zone were significantly longer in 2D compared to 1D specimens due to the continuity and symmetry condition at the plate center as well as the stiffening effect from stretching.

- For quasi-static Mode-II loading, the propagation of a crack will not lead to catastrophic failure, since the load will still increase with further deflection, showing a certain pseudo-ductility effect. If the fracture process zone can be fully developed before failure, then the ultimate load and deflection as well as the delamination area will be independent of the pre-crack size. In practice however, a larger pre-crack will reduce the structural performance more significantly in general, given that the delaminated structures are not always capable of achieving the full fracture process zone before failure.

References

[1] Sridharan S. Delamination Behaviour of Composites. Sridharan S, editor. Delamination Behaviour of Composites. Cambridge, England: Woodhead Publishing Limited; 2008. 1–762 p.

[2] Tabiei A, Zhang W. Composite laminate delamination simulation and experiment: A review of recent development. Appl Mech Rev. 2018;70(3):1–23.

[3] Davies P, Blackman BRK, Brunner AJ. Standard Test Methods for Delamination Resistance of Composite Materials: Current Status. Appl

Compos Mater. 1998;5(6):345–64.

[4]   ISO 15024:2001. Fibre-Reinforced Plastic Composites — Determination of Mode I interlaminar Fracture Toughness, Gic, for Unidirectionally Reinforced Materials. 2001.

[5]   ISO 15114:2014. Fibre-reinforced plastic composites — Determination of the mode II fracture resistance for unidirectionally reinforced materials using the calibrated end-loaded split (C-ELS) test and an effective crack length approach. 2014.

[6]   ASTM D6671/D6671M. Standard Test Method for Mixed Mode I-Mode II Interlaminar Fracture Toughness of Unidirectional Fiber Reinforced Polymer Matrix Composites. 2006;15.

[7]   Blackman BRK, Brunner AJ, Williams JG. Mode II fracture testing of composites: a new look at an old problem. Eng Fract Mech. 2006;73(16):2443–55.

[8]   Sorensen L, Botsis J, Gmür T, Humbert L. Bridging tractions in mode I delamination: Measurements and simulations. Compos Sci Technol. 2008;68(12):2350–8.

[9]   Shahverdi M, Vassilopoulos AP, Keller T. Mixed-mode quasi-static failure criteria for adhesively-bonded pultruded GFRP joints. Compos Part A Appl Sci Manuf. 2014;59:45–56.

[10]   Jiang Z, Wan S, Keller T, Fang Z, Vassilopoulos AP. Influence of curved delamination front on R-curve of DCB specimen. Compos Struct. 2019;227:111311.

[11]   Gong W, Chen J, Patterson EA. An experimental study of the behaviour of delaminations in composite panels subjected to bending. Compos Struct. 2015;123:9–18.

[12]   Nilsson KF, Thesken JC, Sindelar P, Giannakopoulos AE, Stoåkers B. A theoretical and experimental investigation of buckling induced delamination growth. J Mech Phys Solids. 1993;41(4):749–82.

[13]   Rhead AT, Butler R, Hunt GW. Compressive strength of composite laminates with delamination-induced interaction of panel and sublaminate buckling modes. Compos Struct. 2017;171:326–34.

[14]   Andraju LB, Ramji M, Raju G. Snap-buckling and failure studies on CFRP laminate with an embedded circular delamination under flexural loading.

Compos Part B Eng. 2021;214:108739.

[15] Chai H, Babcock CD. Two-Dimensional Modelling of Compressive Failure in Delaminated Laminates. J Compos Mater. 1985;19(1):67–98.

[16] Riccio A, Raimondo A, Di Caprio F, Scaramuzzino F. Delaminations buckling and growth phenomena in stiffened composite panels under compression. Part II: A numerical study. J Compos Mater. 2014;48(23):2857–70.

[17] ASTM D7136. Standard test method for measuring the damage resistance of a fiber-reinforced polymer matrix composite to a drop-weight impact event. Annu B ASTM Stand. 2012;1–16.

[18] Davies GAO, Olsson R. Impact on composite structures. Aeronaut J. 2004;108(1089):541–63.

[19] Davies GAO, Zhang X, Zhou G, Watson S. Numerical modelling of impact damage. Composites. 1994;25(5):342–50.

[20] Davies GAO, Zhang X. Impact damage prediction in carbon composite structures. Int J Impact Eng. 1995;16(1):149–70.

[21] Cartié DDR, Irving PE. Effect of resin and fibre properties on impact and compression after impact performance of CFRP. Compos Part A Appl Sci Manuf. 2002;33(4):483–93.

[22] Sutherland LS, Guedes Soares C. The use of quasi-static testing to obtain the low-velocity impact damage resistance of marine GRP laminates. Compos Part B Eng. 2012;43(3):1459–67.

[23] Zhang X, Hounslow L, Grassi M. Improvement of low-velocity impact and compression-after-impact performance by z-fibre pinning. Compos Sci Technol. 2006;66(15):2785–94.

[24] Chatterjee SN, Dick WA, Byron Pipes R. Mixed-mode delamination fracture in laminated composites. Compos Sci Technol. 1986;25(1):49–67.

[25] Davies GAO, Robinson P, Robson J, Eady D. Shear driven delamination propagation in two dimensions. Compos Part A Appl Sci Manuf. 1997;28(8):757–65.

[26] Kumar P, Reddy SR. Experimental determination of interlaminar GIc using a fully embedded centre-cracked specimen. Eng Fract Mech. 1998;59(2):183–9.

[27] Cameselle-Molares A, Vassilopoulos AP, Keller T. Experimental investigation of two-dimensional delamination in GFRP laminates. Eng Fract Mech. 2018;203(April):152–71.

[28]   Cameselle-Molares A, Vassilopoulos AP, Renart J, Turon A, Keller T. Numerical simulation of two-dimensional in-plane crack propagation in FRP laminates. Compos Struct. 2018;200:396–407.

[29]   Cameselle-Molares A, Vassilopoulos AP, Renart J, Turon A, Keller T. Numerically-based method for fracture characterization of Mode I-dominated two-dimensional delamination in FRP laminates. Compos Struct. 2019;214:143–52.

[30]   Wang C, Vassilopoulos AP, Keller T. Numerical modeling of two-dimensional delamination growth in composite laminates with in-plane isotropy. Eng Fract Mech. 2021;250:107787.

[31]   Wen J, Xia Z, Choy F. Damage detection of carbon fiber reinforced polymer composites via electrical resistance measurement. Compos Part B Eng. 2011;42(1):77–86.

[32]   ISO 527-4:2021(E). Plastics — Determination of tensile properties — Part 4:Test conditions for isotropic and orthotropic fibre-reinforced plastic composites. 2021.

[33]   ISO 19927:2018. Fibre-reinforced plastic composites — Determination of interlaminar strength and modulus by double beam shear test. Geneva, Switzerland; 2018.

[34]   Katsikadelis JT. BEM for Other Plate Problems. In: The Boundary Element Method for Plate Analysis. Academic Press; 2014. p. 113–209.

[35]   Robinson P, Greenhalgh E, Pinho S, editors. Failure mechanisms in polymer matrix composites: Criteria, testing and industrial applications. Cambridge: Woodhead Publishing Limited; 2012.

[36]   Kim JK, Sham ML. Impact and delamination failure of woven-fabric composites. Compos Sci Technol. 2000;60(5):745–61.

[37]   Lee SM. Mode II delamination failure mechanisms of polymer matrix composites. J Mater Sci 1997;32:1287–95.

[38]   Blackman BRK, Kinloch AJ, Paraschi M. The determination of the mode II adhesive fracture resistance, GIIC, of structural adhesive joints: An effective crack length approach. Eng Fract Mech. 2005;72:877–97.

[39]   Khan R. Fiber bridging in composite laminates: A literature review. Compos Struct. 2019;229.

[40]   Hashemi S, Kinloch AJ, Williams JG. The Effects of Geometry, Rate and

Temperature on the Mode I, Mode II and Mixed-Mode I/II Interlaminar Fracture of Carbon-Fibre/Poly(ether-ether ketone) Composites. J Compos Mater. 1990;24(9):918–56.

[41] Wang C, Vassilopoulos AP, Keller T. Mode-II delamination properties of thick glass-fiber/epoxy composite laminates using end-loaded split experiments. Mendeley Data 2023;V1. https://doi.org/10.17632/y88ksnm8xx.1.

[42] Pereira AB, De Morais AB. Mode II interlaminar fracture of glass/epoxy multidirectional laminates. Compos Part A Appl Sci Manuf 2004;35:265–72.

[43] Davies P, Casari P, Carlsson LA. Influence of fibre volume fraction on mode II interlaminar fracture toughness of glass/epoxy using the 4ENF specimen. Compos Sci Technol 2005;65:295–300.

Chapter 4

Mode-II delamination: numerical investigation

4.1 Introduction

Delamination is considered one of the main failure mechanisms in composite structures capable of significantly reducing the structural integrity and load-bearing capacity [1]. Extensive research has been dedicated to studying the delamination fracture behavior of laminated composites, resulting in the establishment and standardization of several testing approaches. For instance, the double cantilever beam (DCB), end-loaded split (ELS) and mixed-mode bending (MMB) tests have been widely used for investigating pure and mixed-Mode fracture behavior [2–4]. However, these investigations typically utilize beam-like specimens, limiting crack propagation to one dimension. In realistic delamination scenarios, cracks are often embedded within laminates and tend to propagate in multiple directions with a changing contour, exhibiting a two-dimensional (2D) pattern.

While a significant number of studies have explored embedded cracks propagating in two dimensions in relation to delamination buckling, these analyses commonly assume that the critical strain energy release rate (SERR) remains identical to that measured from standardized tests, disregarding the differences in specimen configurations [5–7]. Considering that the crack tip of a buckled delamination generally experiences mixed-mode fracture conditions, with the mixity ratio changing both along the delamination perimeter and during the loading history [8], addressing the 2D effects in such complex scenarios without sufficient knowledge of the 2D fracture behavior of each individual mode remains challenging.

The 2D Mode I fracture behavior was investigated experimentally by Kumar and Reddy [9] by opening a centrally embedded circular pre-crack in bonded plexiglass-plates. The resulting Mode-I critical SERR, G_{Ic}, derived from theoretical formulation without considering geometrical nonlinearity, was found to be ~33% lower than that from DCB tests. More recently, Cameselle-Molares et al. [10–12] and the authors [13] used a similar set-up to investigate the 2D Mode-I delamination in glass-fiber/polymer composites in the presence of large-scale fiber bridging. A 2D G_{Ic} value 40-50% higher than that from DCB tests was obtained through a nonlinear numerical-fitting process.

Studies on 2D shear-mode delamination have covered various delamination sources, such as impact-induced delamination [14,15], embedded cracks in a wide beam under three-point bending [16], and edge delamination in circular plates under uniform water pressure with a clamping boundary [17]. However, these findings are limited to specific fracture cases and fail to elucidate the differences from 1D delamination. Recently, the authors proposed a more suitable 2D experimental set-up for Mode II delamination, specifically aiming to reveal the distinctions from 1D experiments. The set-up involved loading circular composite plates with a centrally embedded circular pre-crack transversely above the plate center while semi-clamping the edges to allow free in-plane movement [18]. The results demonstrated that in 2D experiments, the load continued to increase even after crack propagation, and the fracture process zone (FPZ), consisting of resin plastic deformation, microcracking, and fiber/bundle bridging, was significantly larger than that observed in 1D tests. The critical SERR for Mode-II delamination growth, G_{IIc}, was nevertheless left undetermined due to the inapplicability of available data reduction methods, such as compliance-based methods, in the presence of additional membrane forces in the plates, which was a typical 2D geometric-nonlinearity phenomenon, increasing the flexural stiffness [19]. Under such circumstances, numerical approaches can be used to estimate G_{IIc}.

One of the most widely used methods for delamination analyses is the Virtual Crack Closure Technique (VCCT), applied in numerical investigations of both 1D [20,21] and 2D [5,22] specimens, particularly for mode partitioning in mixed-mode delamination [23]. However, VCCT is fundamentally developed within the framework of linear elastic fracture mechanics (LEFM) and cannot be directly applied to cases with a large-scale FPZ [24]. In such cases, the cohesive zone method (CZM) serves as a suitable alternative, which employs a traction-separation law to describe the interactions between the crack surfaces within the FPZ [25].

Efforts have been made to approximate the traction-separation relationships, $\sigma(\delta)$, to represent the Mode-I delamination behavior in laminates with large-scale fiber bridging, where simple linear softening laws have proven insufficient, leading to the exploration of exponential, bilinear, linear-exponential [26] and trilinear [27] softening laws (see Fig. 4.1). The decomposition of the cohesive behavior into a tip component and a bridging component, as implied in the bilinear, linear-exponential and trilinear softening laws, offers additional advantages in numerical analyses [11]. Moreover, researchers have attempted to enhance traditional cohesive models by incorporating the

geometric dependence of the bridging law, which has been revealed in numerous studies [26,28]. For example, Canal et al. [29] proposed a novel cohesive model that correlates the bridging tractions not only with the opening separation but also with the local angle. Pappas and Botsis [30] further developed a simplified formula, which essentially replaced the separation term in the conventional bridging law with the product of the separation and local angle. However, models presented in [29,30] were primarily developed in the context of 1D Mode-I fracture conditions (i.e., DCB experiments), and only considered the beam-thickness dependency of fiber bridging. In the context of Mode-II delamination, fewer studies focusing on cohesive modeling can be found. Heidari-Rarani and Ghasemi [31] compared different shapes of cohesive laws for modeling end-notched flexure (ENF) specimens with R-curve effects and recommended the use of a bilinear softening form. Similarly, Cao et al. [32] employed a bilinear softening law in the simulations of ENF tests, with parameters extracted semi-analytically from test data.
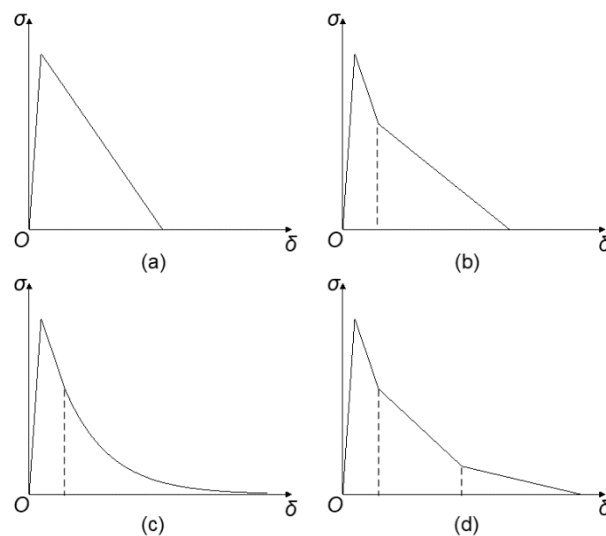
Fig. 4.1. Cohesive relationships: (a) linear, (b) bilinear, (c) linear-exponential and (d) trilinear softening.

This paper aims to numerically investigate the 2D delamination growth behavior under Mode-II fracture condition based on the experiments presented in [18]. Three-dimensional finite element (FE) models were established to simulate the fracture responses of both the 1D and 2D specimens using a novel cohesive model, which takes into account the effects of the large-scale FPZ containing microcracking and fiber bridging. The numerical results clarify the differences between the 1D and 2D cohesive

laws. Additionally, practical methods for identifying the location of an embedded Mode-II crack based on surface curvature and strains are proposed, offering valuable contributions to damage detection in real structures.

4.2 Experimental background

4.2.1 Experimental program

The 1D and 2D delamination behavior of glass-fiber/polymer composites under Mode-II fracture condition was experimentally investigated and compared in [18]. The laminates examined contained 14 inner layers of long continuous filament mats (CFM) and 6 outer layers of multidirectional (quadriaxial $0/\pm45°/90°$) sewed fabrics (MD), with adjacent MD layers rotated by $22.5°$ to achieve in-plane quasi-isotropy, see Fig. 4.2. The combination with the chosen epoxy resin, SikaBiresin CR83, led to good translucency that allows visual observation of the delamination damage (including potential microcracking, which was included in the crack length determination in this work) due to its whitening effect. 13-μm-thick Teflon films cut in proper shapes were placed the middle of the reinforcements to introduce a pre-crack, after which a vacuum infusion process was carried out for laminate fabrication. The laminates were firstly cured under vacuum at room temperature for 16 hours and then post-cured at 70°C for 8 hours. Additionally, a CFM laminate comprising six layers and an MD laminate comprising four layers were fabricated through the same procedure for evaluation of the mechanical properties by tensile and double beam shear tests [33,34]. According to the experimental constitutive curves shown in Appendix B1, both laminates exhibited nonlinearity from an early stage. Table 4.1 lists the engineering constants obtained from the intial slope of the curves, with the remaining values (marked with a superscript) calculated following the approaches described in Ref. [10].

The 1D experiments were performed on a W+B 250-kN universal testing machine under displacement control at a rate of 1 mm/min using an ELS set-up. Five beam specimens were employed, with a free beam length, L, of 150 mm and a pre-crack length, a_0, of 79 mm (refer to EM3 in Table 4.2 as a representative example). During the experiments, the crack lengths, a, were measured from both lateral surfaces using two methods: one lateral surface of the specimens was stamped with a ruler along the delamination path, with the crack propagation recorded by a digital camera; the other surface was stamped with pairs of dots, i.e., tracked targets, evenly spaced on both sides

of the delamination path, monitored by a video-extensometer system at a frequency of 0.2 Hz.
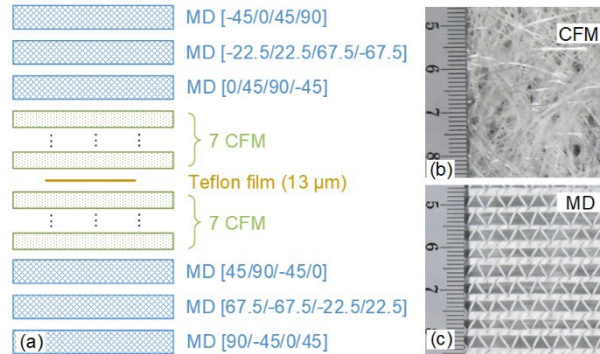

Fig. 4.2. Material description: (a) laminate layup; (b) continuous filament mat and (c) multidirectional sewed fabric.

Table 4.1. Initial engineering elastic constants of laminates.

Reinforce-ment type	V_f (%)	E_1 (GPa)	E_2 (GPa)	E_3 (GPa)	v_{12} (-)	v_{13} (-)	v_{23} (-)	G_{12} (GPa)	G_{13} (GPa)	G_{23} (GPa)
CFM	28.04	11.83	11.83	6.10[a]	0.33	0.30[a]	0.30[a]	4.45[a]	0.62	0.62
MD	44.90	18.23	18.23	8.96[a]	0.32	0.32[a]	0.32[a]	5.36[a]	1.97[a]	1.97[a]

[a] Theoretical values calculated from equations in [10].

Table 4.2. Specimen description for FE modeling[a] (unit: mm).

Model label	Corresponding specimen in [18]	Plane dimension	h	h_{MD}	h_{CFM}	a_0	Half span (R) or free beam length (L)
1	EM3 (1D)	240 × 40 (length × width)	9.1	2.2	6.9	79	150 (L)
2a	CP40-3 (2D)	360 (diameter)	7.5	2.0	5.5	40	150 (R)
2b	CP80-1 (2D)	360 (diameter)	7.9	2.0	5.9	80	150 (R)

[a] h designates the specimen's half thickness, while h_{MD} and h_{CFM} represent the thickness of the MD and CFM layers for each sub-laminate respectively.

The 2D experiments were performed on eight circular plate specimens, organized into two groups based on the radius of the embedded circular pre-crack, a_0. The dimensions of specimens CP40-3 and CP80-1 are provided as examples in Table 4.2. In the experiments, the specimens were subjected to transverse loading and semi-clamped along the edge, where rotation and out-of-plane movement along the edge were constrained, while in-plane sliding was allowed (see Fig. 4.3). The central

deflection, referred to as "deflection" hereafter, was measured by a Linear Variable Differential Transducer (LVDT) fixed below the specimen. Delamination growth was recorded from above by a digital video camera throughout the experiments. From the video frames, the crack lengths in three radial directions (north, "N"; south, "S"; and west, "W") were visually read along the rulers pre-stamped on the top surfaces of the specimens thanks to the translucency of the laminates, and correlated with the load-deflection data. Additionally, a three-dimensional (3D) Digital Image Correlation System (DIC) was employed to measure the displacement and deformation of the top surface of the specimens' east sector. An optical fiber was adhesively bonded to the top surface along the N-S direction to measure the radial strains. Furthermore, a second digital camera was installed below the specimens to monitor potential flexural failure at the bottom center. Overall, the 2D configuration resembled the 1D experiments in the radial direction, except for the additional rotational constraint at the center due to continuity and symmetry. More detailed information about the experimental set-up can be found in Ref. [18].
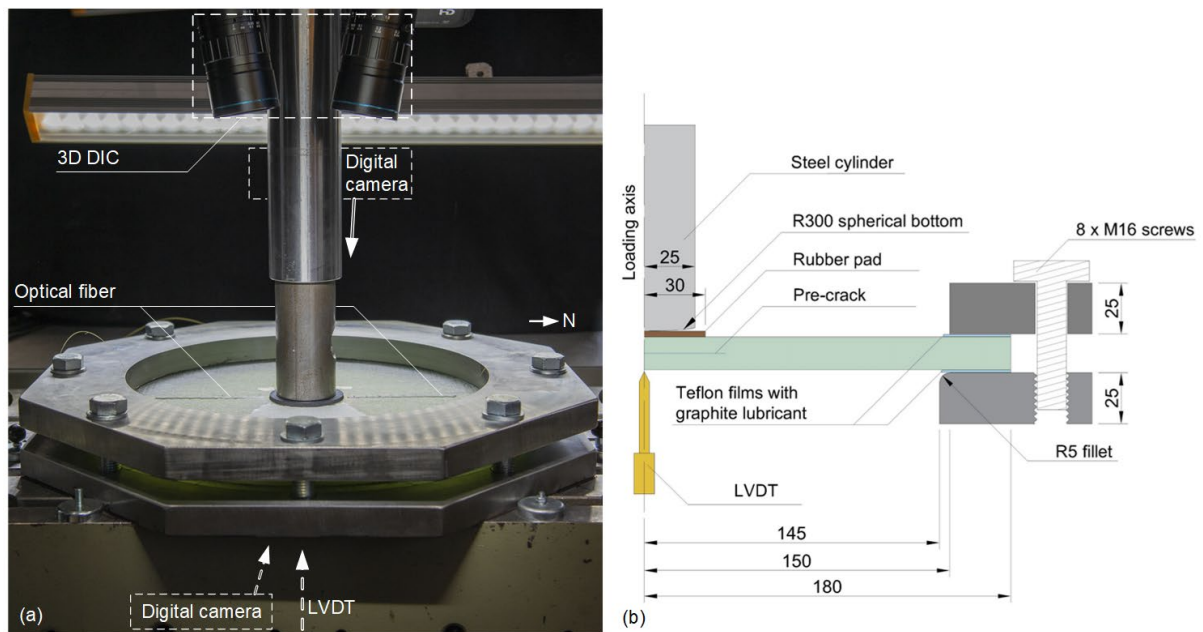
Fig. 4.3. Experimental set-up for 2D delamination: (a) photograph; (b) schematic profile (unit: mm).

4.2.2 Results from 1D experiments

The load-displacement curves for the 1D experiments are shown in Fig. 4.4a. The load increased in the beginning and decreased after ~12 mm of crack propagation. The crack length was measured from both lateral surfaces of the specimens and correlated with the displacement, i.e., direct visual readings along the ruler on one surface using the images captured by the digital camera, and calculations based on the coordinates of the target pairs on the other surface. As shown in Fig. 4.5, for each image from the video-extensometer system, the projected distance (zeroed before loading) between the ith target pair ($1 \leq i \leq$ the total number of the pairs), $T_iT'_i$, along the delamination path, which was approximated as the line segment between the mid-points of the adjacent pairs ($T_{i-1}T'_{i-1}$ and $T_{i+1}T'_{i+1}$), was recorded. This distance was defined as the perceived Mode-II crack sliding, δ_p at the longitudinal coordinate of $T_iT'_i$. The term "perceived" indicates that δ_p did not fully represent the true sliding between the crack surfaces, since it was essentially the relative sliding between the target pair thus additionally including beam shear deformation. In this work, the crack tip was considered to reach a target pair when the corresponding $\delta_p = 0.05$ mm (i.e., the value of sliding for crack initiation), which agreed well with the crack propagation visually measured from the other lateral side. In general, the pre-crack tip was not aligned with any target pair location, and therefore, δ_p at the pre-crack tip, termed δ_p^*, was linearly interpolated using results from adjacent target pairs. However, the crack initiated from the pre-crack tip with $\delta_p^* < 0.05$ mm. This inconsistency possibly resulted from the absence of pre-cracking before loading (thus the fracture behavior at the tip of the Teflon film was different from the bulk material) and the error introduced by liner interpolation. In summary, Fig. 4.4a shows the scatter plots for the crack length versus displacement results from the δ_p measurements, with the exception of the initiation points at a_0=79 mm measured from visual observation. The figure illustrates an initial slow crack propagation stage and a subsequent rapid propagation stage, connected by a transition point (TP). The TP also corresponded to the peak in the load-displacement curves.

The experimental compliance method (ECM) was employed to calculate G_{II}, considering both large-displacement and loading-block correction factors [3]. It is important to point out that the derived G_{II} values contained certain errors due to the high thickness-to-length ratio and the asymmetric fiber layup of the sub-laminates. The resulting R-curves are shown in Fig. 4.6a. According to the figure, G_{II} increased

significantly during crack propagation until reaching a steady value of ~8.1 kJ/m^2 at a ≈ 105 mm. This steady value is an order of magnitude larger than the initiation value, and will hereafter be referred to as G_{IIc}.
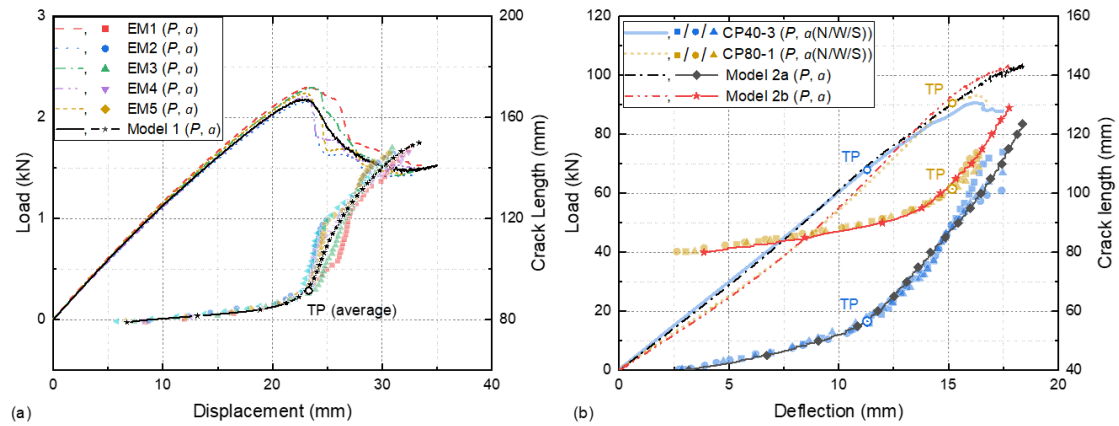

Fig. 4.4. Load, P, and crack length, a, versus displacement (deflection) curves for (a) 1D and (b) 2D specimens. "TP" denotes "transition point" where crack propagation changed from slow to rapid stage in experiments.
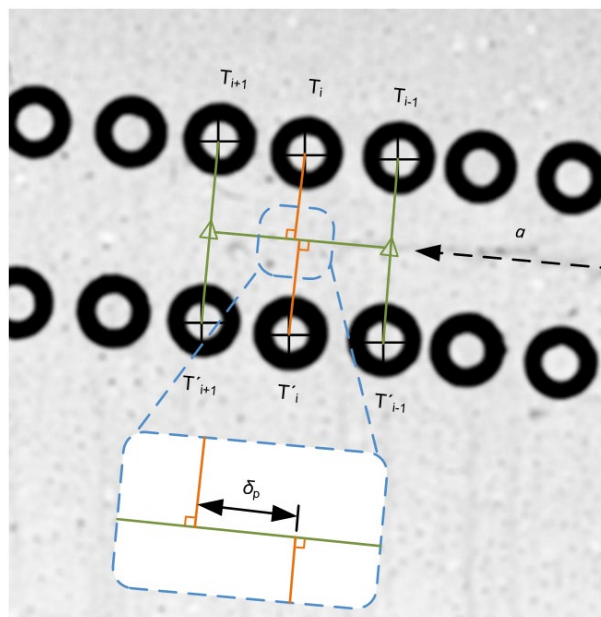

Fig. 4.5. Calculation schema for δ_p from video-extensometer images.
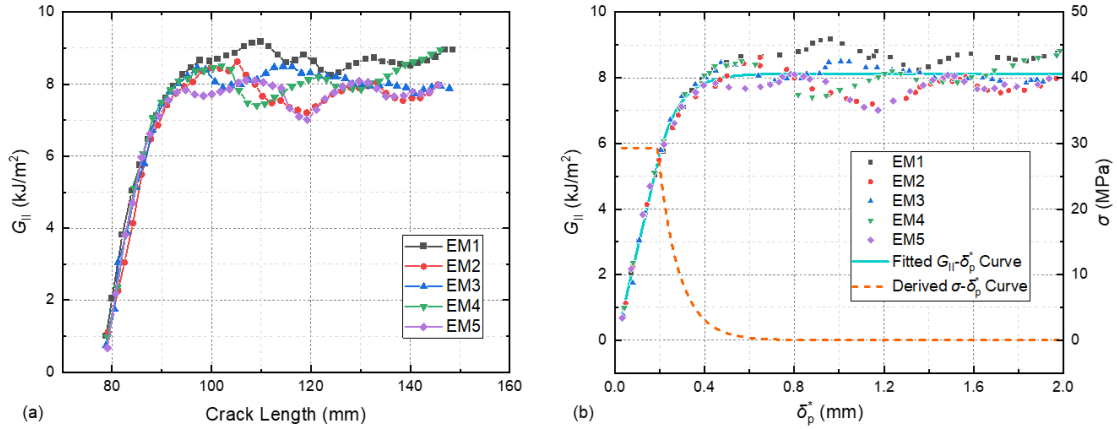
Fig. 4.6. Experimental G_{II} versus (a) crack length (R-curves) and (b) δ_{IIp}^* curves for 1D specimens. The G_{II}-δ_{IIp}^* results were fitted with a linear-exponential curve and differentiated with respect to δ_{IIp}^* to derive an experimental softening law.

The experimental estimation of the Mode-II cohesive softening relationship was carried out as follows. Shrinking the contour of the J integral to the upper and lower surfaces of the cohesive zone gives [35]

$$G = \int_0^{\delta^*} \sigma(\delta)d\delta \tag{4.1}$$

where δ^* is the separation at the pre-crack tip. By differentiating Eq. (4.1) with respect to δ^* [36,37] and using data from the 1D experiments, it follows that

$$\sigma(\delta_p^*) = \frac{\partial G_{II}}{\partial \delta_p^*} \tag{4.2}$$

Therefore, after obtaining the R-curves, G_{II} was further plotted against δ_p^*, as shown in Fig. 4.6b, where a linear-exponential relationship could be observed. The resulting traction-separation relationship, derived by differentiating the fitted G_{II}-δ_p^* curve, exhibited a plateau after crack initiation, followed by exponential softening behavior. Due to potential errors in deducing G_{II} and the fact that δ_p^* was not directly measured at the precise pre-crack tip, this traction-separation relationship served only as a qualitative reference.

During post-inspection using a microscope, hackles reflecting microcracks oriented at ~45° from the main delamination path, bridging fiber bundles and individual bridging fibers were observed along the FPZ. Examples of these microscopic images are presented in Fig. 4.7.
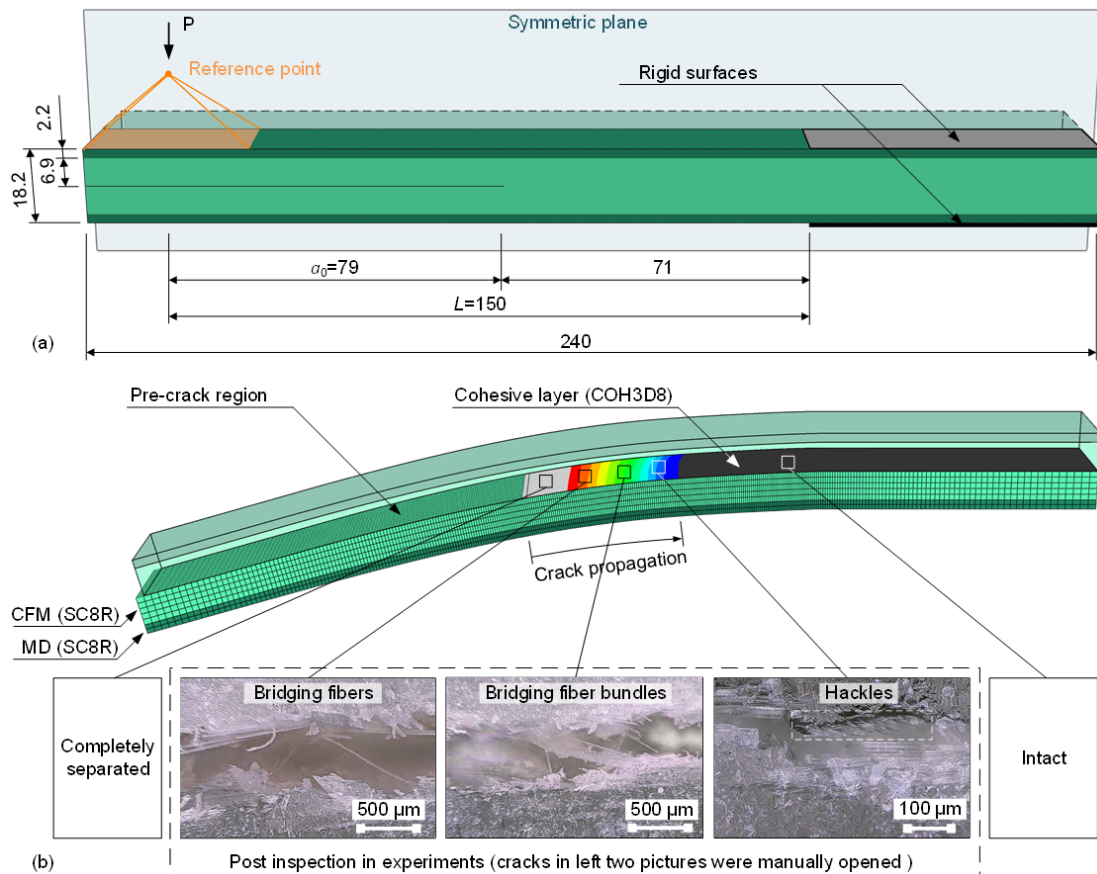
Fig. 4.7. Description of Model 1 for 1D specimens: (a) undeformed (unit: mm); (b) deformed. Fracture response including microcracking (reflected by hackles) and fiber bridging, as shown in microscopic images from experiments [18], was simulated by cohesive modeling.

4.2.3 Results from 2D experiments

The load and crack length versus deflection results for two selected 2D specimens, CP40-3 and CP80-1, were presented in Fig. 4.4b. In contrast to the 1D experiments, the load in 2D experiments continued to increase even after crack propagation. This behavior could be attributed to the increasing crack-front width and the stretching forces in the plates induced by geometric nonlinearity. The crack propagation in the 2D specimens also exhibited both slow and rapid stages. The transition points appeared at a deflection of 11 and 15 mm for specimens CP40-3 and CP80-1 respectively, leading to a decrease in the slope in the load-deflection curves. Notably, both specimens achieved similar ultimate loads and deflections with the crack propagation rates approaching a comparable constant value. According to post-inspection, both specimens failed in flexure at the bottom center before full development of the FPZ. A

comprehensive analysis of the experimental results, as well as further discussion on the FPZ, pre-crack size effect, and differences between 1D and 2D delamination, can be found in Ref. [18].

4.3 Numerical methods

4.3.1 Model of 1D specimens

A FE model, referred to as Model 1, was developed in ABAQUS/Explicit to simulate the 1D delamination behavior based on specimen EM3, with the dimensions provided in Table 4.2. Only one half of the beam, cut longitudinally in the middle, was modeled, with corresponding symmetric boundary conditions applied (Fig. 4.7). The laminate was discretized symmetrically into two sub-laminates at the delamination plane, where a zero-thickness layer of eight-node 3D cohesive elements (COH3D8) were inserted to connect the uncracked region by merging the corresponding nodes. Each sub-laminate consisted of a CFM component and a MD component with appropriate thicknesses, modeled respectively by five and two layers of eight-node continuum shell elements with reduced integration (SC8R). The number of layers was determined for computational efficiency rather than replicating the real composite plies. To ensure an adequate number of elements along the cohesive zone, the longitudinal mesh size for the initially uncracked region was set to be 0.5 mm following a sensitivity analysis. The engineering constants employed to define the bulk material are presented in Table 4.1. For simplicity, the nonlinear material behavior was simulated using plasticity and input as tabular data.

To simulate the sliding boundary condition (ball bearings with lubrication), the beam was positioned between two rigid surfaces with frictionless hard contact. Friction was only introduced between the surfaces in the pre-crack region with a coefficient of 0.3, although the effect of friction was shown to be insignificant, as demonstrated in Ref. [38]. For the split end of the beam, a rigid-body constraint was applied to the top surface to simulate the bonded loading block, with the reference point positioned at the load point. A displacement of up to 35 mm was applied to the reference point to perform the loading process. The nonlinear geometry (NLGEOM) option was used to take into account large deformation effects.

4.3.2 Model of 2D specimens

The same modelling strategy was employed for the simulation of the 2D delamination behavior. Two FE models, referred to as Models 2a and 2b, were developed based on two selected specimens with different pre-crack sizes, namely specimens CP40-3 and CP80-1, whose dimensions are listed in Table 4.2. As an example, Model 2a is presented in Fig. 4.8. Considering symmetry, only one-eighth of the plate was established, using the same element selections and mesh configurations as used in the 1D model. The rubber pad was modeled by six layers of eight-node brick elements with reduced integration and enhanced hourglass control (C3D8R), utilizing the Yeoh model with material properties taken from Ref. [39]. The steel loading block and clamping frames were represented as rigid surfaces with all degrees of freedom constrained.

Symmetric boundary conditions were applied to the two lateral surfaces of the model. Several contact pairs were included in the analysis. The contact between the specimen and the frames was set to be frictionless "hard" contact, which aligned with the smooth slippage observed throughout the experiments. The friction coefficients were set to be 0.5 for the contact with the rubber pad and 0.3 for the pre-crack surfaces. To simulate the loading process, a vertical displacement of up to 20 mm was applied to the loading block.
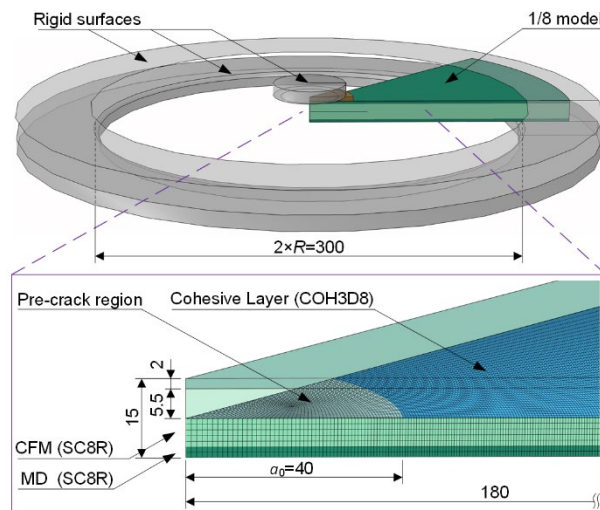
Fig. 4.8. Description of Model 2a for Specimen CP40-3 (unit: mm).

4.3.3 Cohesive model

A new cohesive model, shown in Fig. 4.9, was developed based on the experimental estimation of the softening law (Fig. 4.6b). The model accounts for three major mechanisms observed in the FPZ from the experiments:

- Segment O-A-B-C represents the matrix plastic damage ahead of the macro-crack tip. Segment O-A corresponds to the material continuity before damage onset, where σ increases linearly with δ at a high slope, i.e., penalty stiffness, K_0. After reaching the Mode-II interfacial strength, σ_c, at a separation of δ_c, the curve enters a plateau. The traction drops abruptly at point B with a slope of -K_0, indicating a rapid traction jump.

- Segment C-D represents the microcracking-dominant mechanism, where the separation increases from δ_1 to δ_2 with a constant traction, σ_m. This corresponds to the plateau in the experimental softening law, reflecting the mean shear traction over multiple microcracks.

- Segment D-E represents the fiber (bundle) bridging-dominant mechanism, which appears after the coalescence of the microcracks at the wake of the microcracking zone. In this region, macro separation of the crack surfaces activates fiber (bundle) bridging, as captured by the exponential decay in the experimental softening law. Segment D-E is described using the following relationship, which has been proven effective in modeling the bridging behavior in both 1D and 2D Mode-I delamination [13,26]:

$$\sigma(\delta) = e^{-\gamma\sqrt{\delta-\delta_2}}\sigma_m\left(1 - \sqrt{\frac{\delta - \delta_2}{\delta_f - \delta_2}}\right), \qquad \delta_2 \leq \delta \leq \delta_f \qquad (4.3)$$

  where δ_f is the sliding at which bridging vanishes, γ a parameter that controls the decay rate.

Consequently, the SERR at the crack tip (i.e., the SERR required for crack initiation), G_{tip} and the SERRs dominantly attributed to microcracking and fiber bridging, G_m and G_{br}, can be determined based on the area below the corresponding curve segments (Fig. 4.9a). In summary, the following relationship for the SERR can be obtained:

$$G_{\text{IIc}} = G_{\text{tip}} + G_m + G_{\text{br}} \qquad (4.4)$$

The partition of the cohesive law and the corresponding SERR components are approximate and serve as qualitative tools for analysis, since the real stress state along

the FPZ on the micro scale is complex due to stress singularities at each microcrack and macro-crack tip, which are not explicitly accounted for in the model.
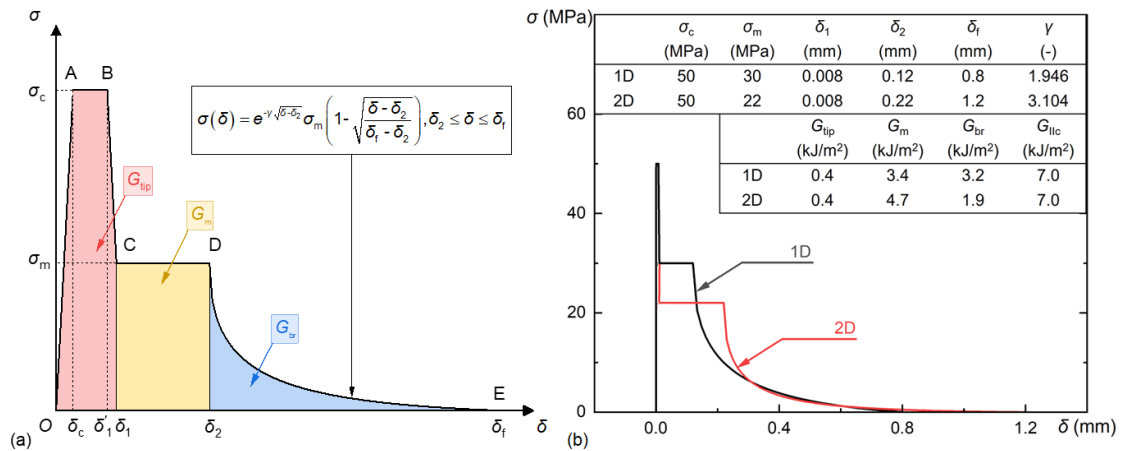

Fig. 4.9. Description of cohesive laws employed: (a) schematic and (b) detailed graphs.

The proposed cohesive model was implemented in the FE models using a user material subroutine (VUMAT) with seven independent parameters, i.e., $\{K_0, \sigma_c, \sigma_m, \delta_1, \delta_2, \delta_f$ and $\gamma\}$. Alternatively, the set of independent parameters can also be chosen as $\{G_{tip}, G_{IIc}, K_0, \sigma_c, \sigma_m, \delta_2$ and $\delta_f\}$ for better reference to the experiments. Among these parameters, G_{tip} was assumed to be equal to that of the CFM specimens under Mode-I delamination, i.e., 0.4 kJ/m^2, regardless of the fracture dimensions. This assumption is supported by previous research findings showing that G_{tip} remains similar not only in Mode I and Mode II delamination of the same material [40] but also in 1D and 2D delamination scenarios [11]. The value of K_0 was set to 100,000 MPa/mm [13]. The value of σ_c was assumed to be 50 MPa, i.e., 60% of the matrix's tensile strength (84 MPa, manufacturer data [41]), as suggested in Ref. [42] based on a micromechanical model using the periodic representative volume element technique.

The four remaining independent variables, G_{IIc}, σ_m, δ_2 and δ_f, were determined through an iterative fitting process for Models 1, 2a and 2b successively, as shown in the flow chart in Fig. 4.10. At the start of the computation for Model 1, the parameters to be determined were initialized according to the experimental traction-separation relationship (Fig. 4.6b), i.e., G_{IIc} = 8.1 kJ/m^2, σ_m = 29 MPa, δ_2 = 0.19 mm, and δ_f = 0.8 mm. To assess the effectiveness of the current parameter set, the resulting crack length-displacement curve, which demonstrated higher sensitivity than the load-displacement

curve commonly employed in the literature, and the FPZ length were compared with the experimental results. Each computation cycle involved adjusting only one parameter until an overall good agreement was achieved. The obtained parameter set served as the initial values for the fitting process for Model 2a and so on. The derived parameter sets and the corresponding SERR components of the cohesive laws are presented in Fig. 4.9b, revealing that Models 2a and 2b shared the same cohesive law (2D), which differed from that of Model 1 (1D).
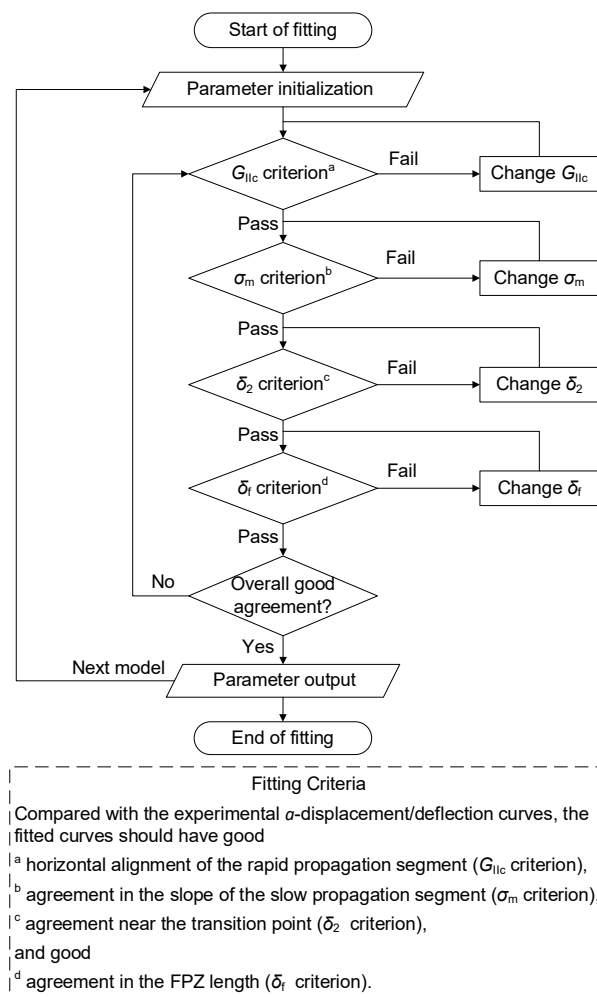
Fig. 4.10. Flow chart for determination of cohesive parameters.

4.4 Numerical results

4.4.1 Load, displacement (deflection) and crack propagation

The load and crack length versus displacement (deflection) curves obtained from the numerical simulations using the final cohesive parameters are presented in Fig. 4.4. The results demonstrated good agreement with the experimental data, confirming the

effectiveness of the employed numerical method in simulating both the 1D and 2D Mode-II delamination behavior.

For Models 2a and 2b, the load-deflection curves showed a slight decrease in slope after the transition from slow to rapid crack propagation, which coincided with the experimental results. However, unlike the experiments, the simulations did not exhibit further fluctuations and load drops due to the absence of failure criteria for the laminates' in-plane properties, which were artificially substituted by perfect plasticity. In reality, flexural damage accumulated at the bottom center of the plates after large deflection and finally led to bending failure. While in the 2D numerical models, the crack propagation curves became nearly parallel after the transition point, approaching a constant growth rate.

4.4.2 R-curves

Based on Eq. (4.1), δ^* was extracted from the models and substituted into the corresponding cohesive laws to calculate G_{II}, which was then plotted against the newly developed crack length, as shown in Fig. 4.11. All three models exhibited pronounced R-curve behavior, with G_{II} rising from 0.4 kJ/m^2 to a plateau of 7.0 kJ/m^2, consistent with the input parameters for the cohesive laws employed (Fig. 4.9b). In comparison, the ECM used in the 1D experiments overestimated the G_{IIc} values by ~1.1 kJ/m^2 (Fig. 4.6a). A larger G_{II} could always be found in 1D delamination than in 2D for any crack propagation length before the plateau, indicating better fracture resistance per unit crack width in early delamination stages. However, considering the increasing crack front, crack propagation in two dimensions usually requires much more energy than in one dimension. Within the context of 2D delamination growth, G_{II} was slightly larger in Model 2b than in Model 2a at any given crack propagation length before reaching the plateau. In addition, the Mode-I SERR component was monitored during the loading, which only presented a negligible value near the end of the loading process.

The full development of the FPZ (i.e., when $\delta^* = \delta_f$, namely $G_{II} = G_{IIc}$) was observed in Models 1 and 2a at displacements (deflections) of 24.5 mm and 18.3 mm, resulting in FPZ lengths of 25.0 mm and 81.6 mm (i.e., the crack lengths at $\delta^* = \delta_f$), respectively. Also note that the cohesive traction in Model 2a at more than 50 mm away from the tip was already neglectable, since the R-curve almost entered a plateau after a=50 mm. These values agreed well with the experimental observations [18]. However, Model 2b did not achieve a full FPZ by the end of the loading process due to its larger

pre-crack size. Furthermore, the full development of the microcracking-dominant zone (i.e., when $\delta^*=\delta_2$) occurred in Models 1, 2a and 2b at displacements (deflections) of 18.6, 10.0 and 12.4 mm respectively. This indicated that the TPs (at displacements of 23.3, 11.3 and 15.2 mm for Models 1, 2a and 2b respectively, see Fig. 4.4) did not correspond to any specific state regarding the formation of the FPZ, but appeared during the development of the bridging-dominant zone.
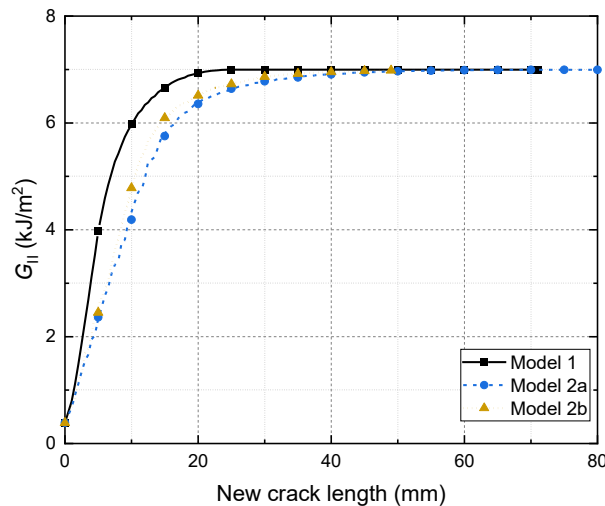

Fig. 4.11. Numerical R-curves.

4.4.3 Membrane stresses in 2D models

A key distinction between the 2D and 1D experiments lies in the presence of membrane forces in the laminates during plate bending, stemming from geometric nonlinearity. As shown in Fig. 4.12a, as the plate deflected, the outer part tended to move inward due to large deformation. However, such radial displacement u, was constrained by the associated circumferential compression effect, which made the outer part behave like a frame, inducing overall radial tensile membrane forces that enhanced the bending stiffness of the plate. The circumferential membrane stresses were disregarded in this work since they act perpendicular to the crack propagation direction.

The radial membrane stresses, σ_r, were extracted from the neutral axes of the plate sections for Models 2a and 2b every 20 mm of crack propagation, and plotted against the polar coordinates, r, as shown in Fig. 4.12b – f. Assuming the laminates behaved similarly in tension and compression, the neutral axis of the outer region aligned with the centerline of the section. For the sub-laminates in the delaminated region, the neutral axis position was estimated using the elastic moduli of the CFM and MD laminates,

and σ_r was subsequently linearly interpolated using the results at adjacent integration points above and below.
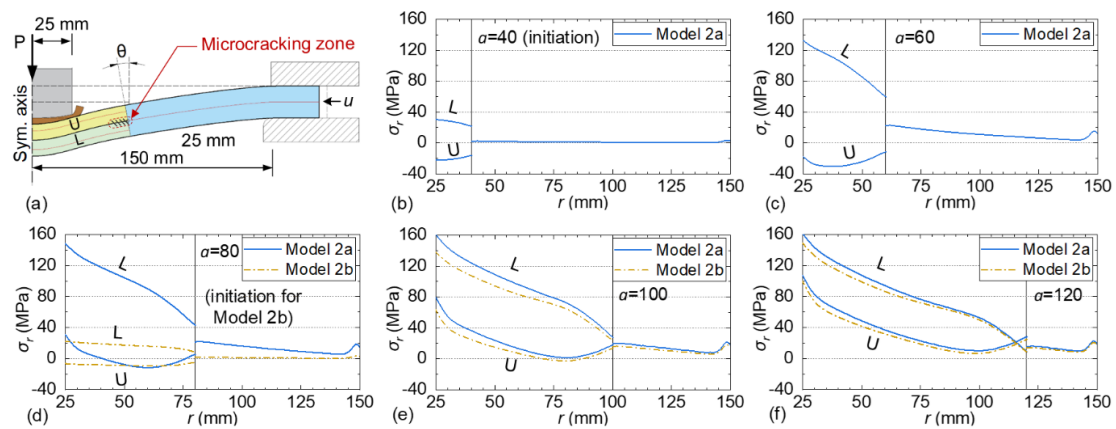
Fig. 4.12. Membrane stresses in 2D models: (a) schematic illustration of the deformed radial section; (b) – (f) radial membrane stresses along r axis (undeformed coordinates) at different crack propagation states. "L" and "U" denote "lower sub-laminate" and "upper sub-laminate" respectively.

In Model 2a, at crack initiation (Fig. 4.12b), σ_r was almost zero in the outer intact region, whereas in the delaminated region, σ_r in the upper ("U") and lower ("L") sub-laminates reached around 20 MPa with opposite signs. At this stage, the geometric nonlinearity effect was insignificant due to small deflection ($\sim$ 3 mm, less than half of the thickness of the sub-laminates, $1/2\ h$). Consequently, the membrane behavior of the sub-laminates was controlled by local effects from the loading block and the rotation of the section at the delamination boundary (see θ in Fig. 4.12a), which resulted in compression of the upper sub-laminate and stretching of the lower. As the loading continued, at a=60 mm (Fig. 4.12c), the outer region also experienced stretching, with σ_r decreasing linearly from the crack tip to the support, except for a local jump above the support boundary. In the lower sub-laminate, σ_r also decreased in an approximate linear manner from the center toward the crack tip, but with an increased slope compared with the previous state. The upper sub-laminate remained under radial compression with slightly increased compressive stresses. For both sub-laminates, the change in slope in the curves near the crack tip resulted from the traction on the crack surfaces. During subsequent crack propagation (Fig. 4.12d – f), σ_r in the upper sub-laminate changed gradually from compressive to tensile, approaching the curve of the lower sub-laminate. This was due to increasing geometric nonlinearity as well as the

decreasing impact of the section rotation (θ) as the crack tip moved outward. Meanwhile, the membrane-stress levels in the lower sub-laminate and the outer region stabilized. Notably, σ_r in the outer region near the crack tip almost maintained a constant value of ~20 MPa from a=60 mm to a=120 mm (Fig. 4.12c – f), which was the average of the σ_r values from the two sub-laminates near the crack tip, following in-plane-force equilibrium at the section.

Model 2b showed similar behavior to Model 2a, and the overall membrane-stress level became comparable to that of Model 2a after a=100 mm. Additionally, the longitudinal membrane stresses were extracted from Model 1 and found to be negligible (less than 2.5 MPa) as expected.

4.5 Discussion

4.5.1 Comparison of cohesive relationships between 1D and 2D delamination

In Section 3.3, the fitting process for the three models resulted in two distinct cohesive laws, one for the 1D case and another for the 2D cases. It was reasonable that Models 2a and 2b shared the same cohesive law since the membrane-stress levels in the laminates were comparable during delamination growth (see Fig. 4.12e and f).

The assumption of equal G_{tip} values in 1D and 2D Mode-I and Mode-II delamination was validated by the good agreement in the crack-initiation displacement (deflection) between the numerical and experimental results for all three models. Surprisingly, the G_{IIc} value was comparable among all three models regardless of the difference in the traction-separation response. This contrasts with Mode-I delamination, where G_{Ic} is significantly larger in 2D scenarios than in 1D due to the increasing amount of fiber bridging [13].

The difference in the detailed shape between 1D and 2D cohesive laws (Fig. 4.9b) can be attributed to the presence of membrane forces. In 1D delamination, the microcracks, oriented ~45° from the main delamination plane, were induced solely by the principal tensile stresses associated with the pure shear stress field, whereas in 2D delamination, the overall tensile membrane stresses along the microcracking zone provided an extra opening component to the inclined microcracks in the normal direction (see Fig. 4.12a), causing the microcracks to initiate in a lower shear stress level. Therefore, σ_m, which represents the mean shear tractions over the microcracking zone, decreased to 22 MPa in 2D delamination, compared with 30 MPa in 1D. Lee [43]

developed an analytical model to study the microcracking mechanisms in ENF tests at a micro-scale level considering the shear lag theory, and attributed the spacing between adjacent microcracks to the shear-stress field decaying ahead of the microcrack (specifically, on the interface between the resin-rich layer where the microcracks were located and the lamina above/below). In the context of 2D delamination, the lower peak shear stresses resulted in a shorter decay distance and hence shorter microcrack spacing. As a consequence, more microcracks initiated in the microcracking zone, contributing to an increased G_m (Fig. 4.9b). This finding coincides with the qualitative analysis in [43], which shows that G_{II} is inversely related to the mean microcrack spacing for typical fiber polymer composites.

The mechanism of fiber bridging in Mode-II delamination has been rarely discussed in the literature. In this work, although the maximum separation at which bridging vanished increased in the 2D model compared to 1D, G_{br} was found to be smaller, which compensated for the increase in G_m, resulting in a comparable G_{IIc} value for both 1D and 2D models.

4.5.2 Locating crack tip in 2D delamination

In the 2D experiments, visual recording of the crack length from above the laminates was feasible due to their translucency. However, for most real structures, cracks are often concealed from direct observation, making it more practical to estimate the crack length based on measurements on the laminate surface. To achieve this, the curvature and strain variations on the top surface of the plate in the radial direction were analyzed, as they reflected changes in bending stiffness between the delaminated and intact regions.

The curvature-based method was validated in Model 2a, as presented in Fig. 4.13. The radial curvature, w'', were obtained every 20 mm of crack propagation by differentiating the vertical displacements of the top surface, w, twice with respect to r coordinates. The results were transferred to undeformed r coordinates to exclude the in-plane deformation and section rotations. For clarity, only the range with $30 \leq r \leq 140$ mm is shown, excluding the local effects from the loading block and clamping frames. According to Fig. 4.13a, most of the plate was under negative bending moments (indicated by negative w'' values) throughout the loading process. In fact, positive moments were concentrated in a small region near the center (approximately $r \leq 25$ mm) reflected by high positive curvatures. Within the displayed range, each w''-r curve

consisted of three segments: a notably decreasing inner segment representing the delaminated region, a moderately decreasing outer segment representing the intact region, and a rising transition segment in between. During delamination growth, the slope of the inner segment changed slightly, while the slopes of the transition segment and the outer segment almost remained unchanged (except for a=40 mm, i.e., crack initiation). The transition segment represented the continuous transition of the bending behavior from the upper sub-laminate to the full laminate near the crack tip, with a radial length of approximately 18 mm that remained almost constant regardless of the loading level, which is approximately one order of the laminate thickness, $2h$ =15 mm. To precisely locate the crack tip, the curvature was further differentiated with respect to r (Fig. 4.13b), and the maximum in the transition zone aligned well with the actual crack tip location (except for the initiation curve, with a small error). In summary, the crack tip can be determined by first identifying the transition zone based on the radial curvature and then finding the maximum in the derivative curve of curvature within the transition zone.
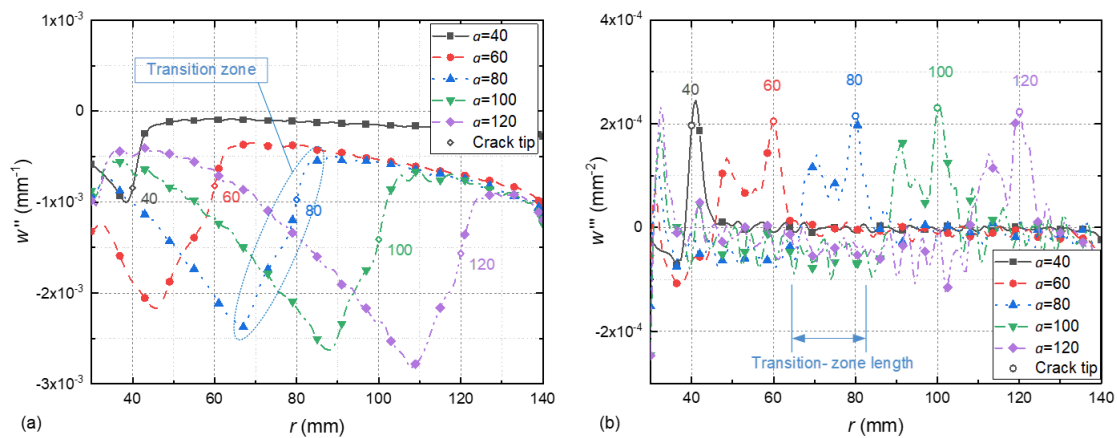
Fig. 4.13. Locating crack tips in Model 2a based on curvature data on top surface: (a) w'' and (b) w''' along r axis (undeformed coordinates).

The discussions presented so far are based on the numerical model, which produced minor noise in the results and can be assumed as an ideal case. In practice, the accuracy of measurements is limited by the measuring devices and sampling density, resulting in significant noise during higher order differentiation. Therefore, the measured w should be processed before the differentiation process. As an example, in the case of specimen CP40-3, the experimental w-r curves measured from the DIC

system (Fig. 4.14a) were fitted with ninth order polynomial curves (not shown as they nearly overlap with the measured ones before differentiation). The selection of the polynomial order was based on the expectation that roughly five inflection points would be presented in the w'''-r curve in corresponding region ($33 \leq r \leq 140$ mm), according to the numerical results (Fig. 4.13b). The subsequent differentiation on the fitted curves resulted in smooth w''-r curves (Fig. 4.14b) that resembled the shape of the numerical ones (Fig. 4.13a). However, some fine details near the crack tip were not accurately captured, leading to a shift in the local maxima in the subsequent derivatives from the crack tip location. Consequently, the maxima in the w'''-r curves underestimated the crack length by around $5 - 9$ mm, but the error decreased as the crack propagated further.
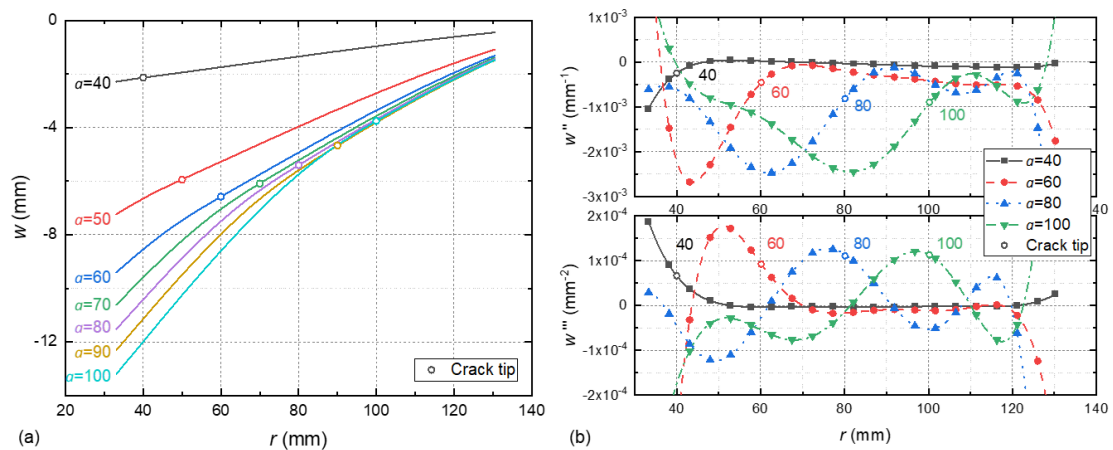
Fig. 4.14. Locating crack tips in specimen CP40-3 based on curvature measurements on top surface: (a) original w-r curves and (b) w''-r and w'''-r curves differentiated from fitted w-r curves (undeformed coordinates).

Alternatively, the strains on the top surface can also be used to estimate the crack tip locations. For instance, a steep increase in the surface strains was observed near the debond tip in wrapped composite joints in Ref. [44]. In this work, the radial-strain distribution at different crack propagation states, obtained from the fiber optic system, was analysed. Example curves of specimen CP40-3 are presented in Fig. 4.15a, which also exhibit three segments in the radial direction. The transition-zone length determined from the radial-strain curves was comparable to that obtained from the curvature curves (i.e., ~18 mm, see Fig. 4.13). Similarly, ninth-order polynomial curves were employed to fit the data points to derive smoother derivative curves as shown in Fig. 4.15b. The minima in the transition-zone range were found to be ~2 mm behind

the actual crack tip location due to the inability of the fitting process to capture the detailed slope fluctuations at the tip (similar to that in w''-r curves), which could be observed in the numerical models (not shown for brevity). This resulted in a slight underestimation of a, but the method still demonstrated effectiveness and better precision compared to the previous curvature-based method.
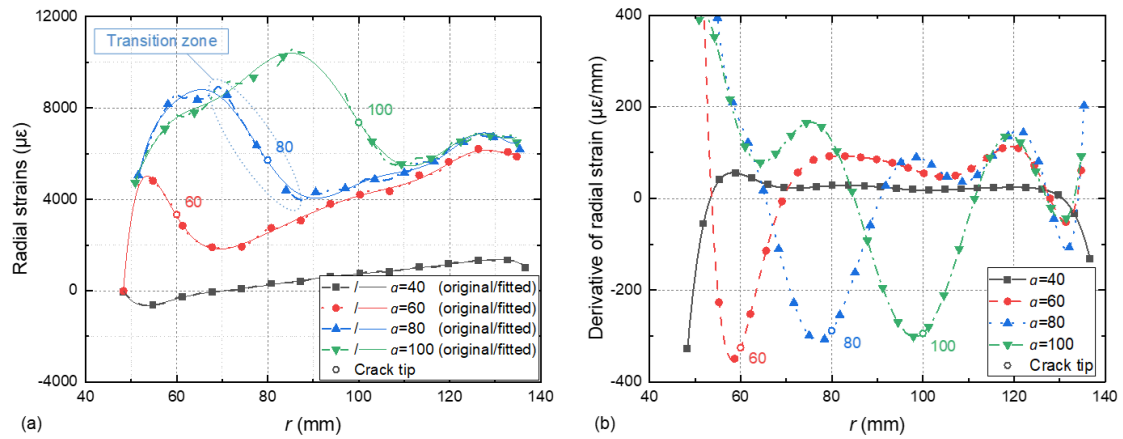
Fig. 4.15. Locating crack tips in specimen CP40-3 based on radial strain measurements on top surface: (a) original and fitted radial strains and (b) their derivative along r axis (undeformed coordinates).

Likewise, measurements on the bottom surfaces can also be used for locating the crack tip, depending on the accessibility. Overall, both methods (curvature-based and strain-based) offer viable means to estimate crack tip locations based on measurements on the laminate surface, and the strain-based method is particularly recommended due to its ease of use and better precision. Moreover, the proposed approaches remain applicable even for embedded cracks with irregular shapes. In such scenarios, the measurements of vertical displacements or primary strains (instead of radial strains) should be carefully analyzed across the entire area of interest to obtain the gradients of curvature and strains (feasible through certain measuring methods like the DIC system). Once these gradients are available, the proposed approach can be applied along the gradient directions to estimate individual tip locations, ultimately forming a continuous 2D crack front.

4.6 Conclusions

The 1D and 2D delamination growth in composite laminates under Mode-II fracture conditions was investigated numerically based on previous experimental results. A new cohesive model was employed for a comparative analysis between the 1D and 2D delamination behaviors, discerning the 2D effects. The following conclusions were drawn:

- A new cohesive model was developed using a semi-experimental approach, which successfully simulated both the 1D and 2D delamination behavior of laminates under Mode-II fracture conditions in the presence of microcracking and fiber bridging.

- The proposed cohesive model, combined with the fitting strategy, proved effective in deriving the SERR from experimental data, particularly when analytical solutions were challenging due to complex fiber layup designs or material and geometric nonlinearity.

- The introduced cohesive law could describe 2D delamination growth from pre-cracks of various sizes. However, different traction-separation responses were observed between 1D and 2D delamination cases, necessitating distinct sets of cohesive parameters. While the 1D and 2D specimens exhibited comparable SERR for crack initiation and full FPZ development, the mean traction over the microcracking zone was significantly lower in 2D delamination.

- During 2D delamination growth, the laminates experienced significant membrane stresses due to geometric nonlinearity. The lower sub-laminate and outer intact region underwent stretching throughout the loading process, with the stretching-stress level stabilizing after around 20 mm of crack propagation. Conversely, the upper sub-laminate experienced initial compressive membrane stresses, which shifted to stretching stresses as the delamination grew further.

- Methods for locating the tip of an embedded circular crack based on experimentally measured radial curvatures (obtained from vertical displacements) and strains were proposed, with the strain-based method demonstrating better precision. These nondestructive and convenient approaches hold great potential for application in more complex structures with irregular crack shapes.

References

[1]   Sridharan S. Delamination Behaviour of Composites. Sridharan S, editor. Cambridge, England: Woodhead Publishing Limited; 2008.

[2]   ISO 15024:2001. Fibre-reinforced plastic composites — Determination of mode I interlaminar fracture toughness, Gic, for unidirectionally reinforced materials. 2001.

[3]   ISO 15114:2014. Fibre-reinforced plastic composites — Determination of the mode II fracture resistance for unidirectionally reinforced materials using the calibrated end-loaded split (C-ELS) test and an effective crack length approach. 2014.

[4]   ASTM D6671/D6671M. Standard Test Method for Mixed Mode I-Mode II Interlaminar Fracture Toughness of Unidirectional Fiber Reinforced Polymer Matrix Composites. 2006;

[5]   Riccio A, Raimondo A, Di Caprio F, Scaramuzzino F. Delaminations buckling and growth phenomena in stiffened composite panels under compression. Part II: A numerical study. J Compos Mater. 2014;48(23):2857–70.

[6]   Rhead AT, Butler R, Hunt GW. Compressive strength of composite laminates with delamination-induced interaction of panel and sublaminate buckling modes. Compos Struct. 2017;171:326–34.

[7]   Andraju LB, Ramji M, Raju G. Snap-buckling and failure studies on CFRP laminate with an embedded circular delamination under flexural loading. Compos B Eng. 2021;214:108739.

[8]   Nilsson KF, Thesken JC, Sindelar P, Giannakopoulos AE, Stoåkers B. A theoretical and experimental investigation of buckling induced delamination growth. J Mech Phys Solids. 1993;41(4):749–82.

[9]   Kumar P, Reddy SR. Experimental determination of interlaminar GIc using a fully embedded centre-cracked specimen. Eng Fract Mech. 1998;59(2):183–9.

[10]   Cameselle-Molares A, Vassilopoulos AP, Keller T. Experimental investigation of two-dimensional delamination in GFRP laminates. Eng Fract Mech. 2018;203:152–71.

[11]   Cameselle-Molares A, Vassilopoulos AP, Renart J, Turon A, Keller T. Numerical simulation of two-dimensional in-plane crack propagation in FRP laminates. Compos Struct. 2018;200:396–407.

[12] Cameselle-Molares A, Vassilopoulos AP, Renart J, Turon A, Keller T. Numerically-based method for fracture characterization of Mode I-dominated two-dimensional delamination in FRP laminates. Compos Struct. 2019;214:143–52.

[13] Wang C, Vassilopoulos AP, Keller T. Numerical modeling of two-dimensional delamination growth in composite laminates with in-plane isotropy. Eng Fract Mech. 2021;250:107787.

[14] Davies GAO, Zhang X. Impact damage prediction in carbon composite structures. Int J Impact Eng. 1995;16(1):149–70.

[15] Cartié DDR, Irving PE. Effect of resin and fibre properties on impact and compression after impact performance of CFRP. Compos Part A Appl Sci Manuf. 2002;33(4):483–93.

[16] Chatterjee SN, Dick WA, Byron Pipes R. Mixed-mode delamination fracture in laminated composites. Compos Sci Technol. 1986;25(1):49–67.

[17] Davies GAO, Robinson P, Robson J, Eady D. Shear driven delamination propagation in two dimensions. Compos Part A Appl Sci Manuf. 1997;28(8):757–65.

[18] Wang C, Vassilopoulos AP, Keller T. Experimental investigation of two-dimensional Mode-II delamination in composite laminates. Compos Part A Appl Sci Manuf. 2023;173:107666.

[19] Katsikadelis JT. BEM for Other Plate Problems. In: The Boundary Element Method for Plate Analysis. Academic Press; 2014. p. 113–209.

[20] Shahverdi M, Vassilopoulos AP, Keller T. Mixed-mode quasi-static failure criteria for adhesively-bonded pultruded GFRP joints. Compos Part A Appl Sci Manuf. 2014;59:45–56.

[21] Jiang Z, Wan S, Keller T, Fang Z, Vassilopoulos AP. Influence of curved delamination front on R-curve of DCB specimen. Compos Struct. 2019;227:111311.

[22] Pietropaoli E, Riccio A. Formulation and assessment of an enhanced finite element procedure for the analysis of delamination growth phenomena in composite structures. Compos Sci Technol. 2011;71(6):836–46.

[23] Krueger R. Virtual crack closure technique: History, approach, and applications. Appl Mech Rev. 2004;57(1–6):109–43.

[24]   Tabiei A, Zhang W. Composite laminate delamination simulation and experiment: A review of recent development. Appl Mech Rev. 2018;70(3):1–23.

[25]   Park K, Paulino GH. Cohesive zone models: A critical review of traction-separation relationships across fracture surfaces. Appl Mech Rev. 2011;64(6).

[26]   Frossard G, Cugnoni J, Gmür T, Botsis J. Mode I interlaminar fracture of carbon epoxy laminates: Effects of ply thickness. Compos Part A Appl Sci Manuf. 2016;91:1–8.

[27]   Yin S, Gong Y, Li W, Zhao L, Zhang J, Hu N. A novel four-linear cohesive law for the delamination simulation in composite DCB laminates. Composites Part B. 2020;180(October 2019):107526.

[28]   Manshadi BD, Vassilopoulos AP, Botsis J. A combined experimental/numerical study of the scaling effects on mode I delamination of GFRP. Compos Sci Technol. 2013;83:32–9.

[29]   Canal LP, Alfano M, Botsis J. A multi-scale based cohesive zone model for the analysis of thickness scaling effect in fiber bridging. Compos Sci Technol. 2017;139:90–8.

[30]   Pappas GA, Botsis J. Towards a geometry independent traction-separation and angle relation due to large scale bridging in DCB configuration. Compos Sci Technol. 2020;197:108172.

[31]   Heidari-Rarani M, Ghasemi AR. Appropriate shape of cohesive zone model for delamination propagation in ENF specimens with R-curve effects. Theoretical and Applied Fracture Mechanics. 2017;90:174–81.

[32]   Cao T, Zhao L, Wang L, Wang K, Gong Y, Zhang J. An efficient semi-analytical method to extract the mode II bridging-traction law in ENF tests directly from the experimental load displacement data. Compos Struct. 2022;285(January):115229.

[33]   ISO 527-4:2021(E). Plastics — Determination of tensile properties — Part 4:Test conditions for isotropic and orthotropic fibre-reinforced plastic composites. 2021.

[34]   ISO 19927:2018. Fibre-reinforced plastic composites — Determination of interlaminar strength and modulus by double beam shear test. Geneva, Switzerland; 2018.

[35]   Rice JR. A path independent integral and the approximate analysis of strain concentration by notches and cracks. J Appl Mech. 1968;35(2):379–88.

[36]   Suo Z, Bao G, Fan B. Delamination R-curve phenomena due to damage. J Mech Phys Solids. 1992;40(1):1–16.

[37]   Sørensen BF, Jacobsen TK. Large-scale bridging in composites: R-curves and bridging laws. Compos Part A Appl Sci Manuf. 1998;29(11):1443–51.

[38]   Mencattelli L, Borotto M, Cugnoni J, Lazzeri R, Botsis J. Analysis and evaluation of friction effects on mode II delamination testing. Compos Struct. 2018;190(January):127–36.

[39]   Shahzad M, Kamran A, Siddiqui MZ, Farhan M. Mechanical characterization and FE modelling of a hyperelastic material. Materials Research. 2015;18(5):918–24.

[40]   Hashemi S, Kinloch AJ, Williams JG. The Effects of Geometry, Rate and Temperature on the Mode I, Mode II and Mixed-Mode I/II Interlaminar Fracture of Carbon-Fibre/Poly(ether-ether ketone) Composites. J Compos Mater. 1990;24(9):918–56.

[41]   SikaBiresin CR83. Product Data Sheet [Internet]. 2021.

[42]   Ye Q, Chen P. Prediction of the cohesive strength for numerically simulating composite delamination via CZM-based FEM. Compos B Eng. 2011;42(5):1076–83.

[43]   Lee SM. Mode II delamination failure mechanisms of polymer matrix composites. J Mater Sci. 1997;32(5):1287–95.

[44]   He P, Pavlovic M. Failure modes of bonded wrapped composite joints for steel circular hollow sections in ultimate load experiments. Eng Struct. 2022;254(December 2021):113799.

Chapter 5

Conclusions and future work

5.1 Conclusions

In this thesis, the two-dimensional (2D) delamination growth in composite laminates under pure Mode-I and Mode-II fracture conditions was explored through both experimental and numerical investigations. Parametric analyses were executed to discern the influence of various factors on 2D delamination behavior and structural response. A novel cohesive zone model, formulated with consideration of microcracking and fiber bridging within the fracture process zone, was developed utilizing a semi-experimental methodology and incorporated into three-dimensional finite element simulations. The key findings and conclusions drawn from this study are listed below.

5.1.1 Increasing loads during 2D delamination growth

In contrast to standardized fracture tests where loads decrease upon crack propagation, 2D delamination experiments exhibited continuously increasing loads until flexural failure of the plates. This phenomenon stemmed from both the increasing crack-front length and the stiffening effect from the membrane stresses (i.e., stretching), which were induced by large deformation during flexure. Therefore, 2D delamination growth in composites will not lead to catastrophic failure, presenting a certain pseudo-ductility effect. In Mode-II delamination experiments, by plotting the shear force per unit crack width, instead of the total load, against deflection, similar dropping trends in the curves could be obtained for both 1D and 2D cases.

5.1.2 Crack initiation and propagation behavior

In scenarios of 2D delamination with circular symmetric loading conditions, the crack initiated in all directions simultaneously. Conversely, in cases featuring an elliptic loading zone or pre-crack, the crack primarily initiated in the direction showing the shortest distance between the loading-zone and pre-crack fronts, due to the non-uniform strain energy release rate (SERR) distribution along the pre-crack perimeter.

The radial crack propagation rates experienced an increase during loading. In Mode-I delamination, the crack propagation rate rose as soon as full development of fiber bridging occurred, while in Mode-II delamination, the crack propagation rate rose during the development of the fiber-bridging zone. If enough propagation can be achieved before flexural failure of the laminates (usually not the case in real structures), the delamination will finally grow in a constant shape, which was mainly affected by the loading-zone shape and independent of the pre-crack shape or size.

5.1.3 Effect of pre-crack size

In 2D delamination scenarios, the pre-crack size greatly affected the initial structural stiffness, forcing the crack to initiate at a larger deflection and lower initiation load. In fact, specimens with larger pre-cracks consistently exhibited lower load levels compared to smaller pre-crack specimens. In addition, the 2D Mode-II experiments demonstrated that, at flexural failure, the specimens with larger pre-cracks exhibited lower ultimate loads and deflections.

5.1.4 Effect of fracture resistance

In 2D delamination scenarios, after full development of the fracture process zone (FPZ), the stiffness of the system retained a constant value, which increased linearly with the fracture resistance. Higher fracture resistance also induced the final delamination shape to more closely resemble the loading zone shape.

5.1.5 Cohesive laws and mechanisms within FPZ

For delamination between layers with continuous filament mat (CFM) reinforcements, a large-scale FPZ was observed under both Mode-I and Mode-II fracture conditions. The utilization of the cohesive zone method proved beneficial for describing such delamination behavior, effectively segregating the crack tip region and its trailing zone. Behind the crack tip, Mode-I delamination was dominated by fiber bridging, described by an exponential softening law, while Mode-II delamination saw contributions from microcracking and fiber bridging, which could be represented by the plateau and the exponential segments in the softening curve, respectively.

5.1.6 Membrane effects on 2D delamination

Membrane stresses were introduced to the laminates during 2D delamination growth due to large deflection, which is a geometric nonlinear phenomenon inherent to 2D flexure. These stresses affected the fracture mechanisms within the FPZ significantly, constituting the main factor differentiating 1D and 2D delamination behaviors. In Mode-I delamination, the tensile membrane stresses enhanced the fiber bridging and consequently increased the total SERR; in Mode-II delamination, these stresses introduced additional opening components to the inclined microcracks, reducing the mean traction over the microcracking zone, while maintaining a comparable total SERR to that of the 1D tests.

5.1.7 Locating embedded crack tip using surface measurements

Methods for locating the tip of an embedded circular crack were proposed, employing experimentally measured radial curvatures (obtained from vertical displacements) and strains. The strain-based method exhibited superior precision. These nondestructive and convenient approaches show great potential for application in more complex structures with irregular crack shapes.

5.2 Original contributions

The original contributions of this thesis are summarized as follow:

1. The effects of different factors, including pre-crack and loading-zone shape and size, as well as fracture resistance, on the growth of 2D Mode-I delamination were parametrically studied.

2. A novel experimental setup was developed specifically for investigating 2D Mode-II delamination growth. This approach offers a more realistic representation of delamination behavior compared to standardized fracture tests. The pseudo ductility demonstrated in 2D delamination growth can provide valuable references to damage-tolerant designs of composite structures.

3. A new cohesive model was introduced, incorporating both microcracking and fiber bridging mechanisms within the fracture process zone (FPZ). This model, developed using a semi-experimental approach, accurately captured the

behavior of both 1D and 2D Mode-II delamination, contributing to a better understanding of the underlying mechanics.

4. By examining the differences between 1D and 2D Mode-II delamination behavior, the study uncovered the significance of membrane stresses generated in laminates during large deflection.

5. Practical approaches for locating the embedded crack front were proposed, employing surface curvature and strain measurements, which hold promises for application in structures with irregular crack shapes.

5.3 Recommendations for future work

5.3.1 1D delamination experiments with membrane stresses

The differences between the 1D and 2D delamination behavior, including the traction-separation relationships and the SERR, have been attributed to the membrane stresses induced during large deflection of the laminates. As shown in the thesis, the 2D effects can be quantified in the 2D experiments and corresponding numerical simulations. However, such direct methods typically require substantial efforts and are thus difficult to perform for every engineering case in practice. It is preferred by engineers and researchers to carry out standardized tests, and then extrapolate the results for 2D applications. To achieve this, it is important to explore the relationship between the membrane stresses and the SERR. Developing a novel 1D experimental set-up that resembles the standardized fracture tests but additionally introduces membrane stresses in the specimens during crack propagation, is suggested, alongside continuous monitoring of membrane-stress levels. This could be followed by numerical or analytical methods to derive the SERR, and subsequently correlating variations in the SERR to membrane stresses. Upon establishing this relationship, a coefficient or equation could be developed to translate the SERR derived in standardized tests to 2D cases based on membrane stress information.

5.3.2 2D mixed-mode delamination growth

While this thesis delved into the behavior of 2D Mode-I and Mode-II delamination, real structures often feature embedded cracks that propagate under mixed-mode fracture conditions owing to complex stress states. It is recommended to further expand the

scope of experimental and numerical investigations to encompass the 2D mixed-mode delamination behavior, using a methodology akin to that demonstrated in this thesis.

A possible experimental method could involve adopting the same specimen configuration and test fixtures as those employed in the 2D Mode-II experiments, while pulling one side of the pre-crack surface (see Fig. 5.1). To effectively apply the asymmetric opening load, the use of a steel insert, bolted to an external steel plate (resembling the arrangement introduced in Ref. [1]), is suggested. By varying the height of the pre-crack, different mixed-mode ratios could be achieved. Beginning with in-plane isotropic laminates, the study could accomplish the formulation of a 2D mixed-mode criterion that bridges the current findings regarding pure Mode-I and Mode-II delamination behaviors.
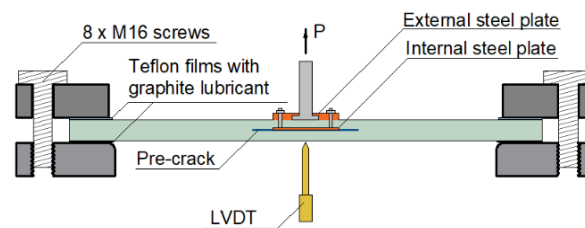
Fig. 5.1. Proposed set-up for 2D mixed-mode experiments.

5.3.3 Modified model considering membrane stresses in laminates

Traditional cohesive zone models determine the traction in the cohesive zone based on the separation of crack surfaces, without considering bulk material stress states. However, this thesis has demonstrated that the membrane stresses, which are common in 2D delamination scenarios, can significantly affect the fracture behavior within a large-scale FPZ. Developing a new cohesive model that considers the membrane stress levels within laminates is therefore crucial for accurate delamination simulations in composite structures. This model could potentially incorporate the SERR-membrane stress relationship as discussed in Section 5.3.1.

Modified cohesive models considering the crack opening angle (crack-surface curvature) in addition to the crack opening displacement can be found in Ref [2,3], which eliminate the stiffness dependency of the SERR due to fiber bridging in Mode-I delamination. Further investigation is needed to verify if these models can also explain the 2D effects under Mode-I fracture conditions, considering that stiffness enhancement is the main influence from the membrane stresses in 2D Mode-I delamination. For

Mode-II delamination, on the other hand, the 2D effects on the fracture properties are not attributed to changes in laminate stiffness or crack-surface curvature. A new model formulated with information about the strain or stress in the length direction is required.

5.3.4 Extending analysis to orthotropic laminates

In practical applications, orthotropic laminates are widely employed to harness material properties effectively based on load paths. Analyzing the 2D fracture behavior of orthotropic laminates, which could involve complex mode mixity and direction-dependent fracture responses, presents challenges. Preliminary investigations on 2D Mode-I delamination for orthotropic laminates have been conducted in Ref. [1], but a comprehensive exploration of their 2D delamination behavior, particularly under Mode-II conditions, is recommended, using the set-up developed in Chapter 3. This involves a combination of experimental and numerical investigations, building upon the concepts proposed in Sections 5.3.2 and 5.3.3.

5.3.5 Analytical solutions for 2D delamination growth

While this thesis focused on experimental and numerical investigations, there is a valuable role for analytical exploration of 2D delamination growth, which could provide clear physical explanations, and potentially offer solutions for 2D SERR derivation. The expression for the SERR in a general cracked plate was reduced to that of an equivalent split beam by Nilsson and Storåkers [4] in order to partition the fracture modes conveniently. Other investigations of more specific cases can be found in Ref. [5,6], where circular plates with embedded crack subjected to transverse loads were analyzed based on first-order and third-order shear deformation theories. However, Ref. [5,6] are essentially flexure analyses of delaminated plates, and the effects of a large-scale FPZ were not included. Further analytical research could involve integrating flexure analysis with J-integral techniques in the context of 2D delamination growth with a large-scale FPZ.

5.3.6 2D fatigue delamination

Fiber bridging has been found to be an important toughening effect in fatigue delamination growth in 1D Mode-I specimens [7], with strong geometric dependency similar to that observed in quasi-static delamination growth [8]. Other research suggests that high fatigue amplitude associated with low R-ratios can break bridging fibers thus

minimizing their contribution to the SERR [9]. The 2D effects on fatigue delamination growth, especially under Mode-II (dominant) fracture conditions, are still unclear. To bridge this gap, it is recommended to conduct 2D fatigue delamination experiments with varying R-ratios (using the same set-ups as those in the quasi-static experiments) and compare the results with 1D experiments.

References

[1]   Cameselle-Molares A, Vassilopoulos AP, Keller T. Experimental investigation of two-dimensional delamination in GFRP laminates. Eng Fract Mech 2018;203:152–71.

[2]   Canal LP, Alfano M, Botsis J. A multi-scale based cohesive zone model for the analysis of thickness scaling effect in fiber bridging. Compos Sci Technol 2017;139:90–8.

[3]   Pappas GA, Botsis J. Towards a geometry independent traction-separation and angle relation due to large scale bridging in DCB configuration. Compos Sci Technol 2020;197:108172.

[4]   Nilsson KF, Storåkers B. On interface crack growth in composite plates. Journal of Applied Mechanics, Transactions ASME 1992;59:530–8.

[5]   Chen D, Chen C, Fu Y, Dai L. Growth of delamination for laminates circular plates subjected to transverse loads. Proceedings of the ASME 2009 International Mechanical Engineering Congress and Exposition. Volume 10: Mechanical Systems and Control, Parts A and B., Florida, USA: ASME; 2009, p. 597–605.

[6]   Haghani A, Mondali M, Faghidian SA. Linear and nonlinear flexural analysis of higher-order shear deformation laminated plates with circular delamination. Acta Mech 2018;229:1631–48.

[7]   Khan R. Fiber bridging in composite laminates: A literature review. Compos Struct 2019;229.

[8]   Farmand-Ashtiani E, Cugnoni J, Botsis J. Effects of large scale bridging in load controlled fatigue delamination of unidirectional carbon-epoxy specimens. Compos Sci Technol 2016;137:52–9.

[9]   Cameselle-Molares A, Vassilopoulos AP, Keller T. Two-dimensional fatigue debonding in GFRP/balsa sandwich panels. Int J Fatigue 2019;125:72–84.

Appendix A1

Development of 2D Mode-II experimental set-ups

A1.1 Overview

The experimental set-up and specimen configurations for the investigation of 2D Mode-II delamination in Chapter 3 were established following a series of preliminary designs and trials, which are summarized in Table A1. Detailed experimental data can be found in Ref. [1].

Table A1.1 Set-up list for 2D Mode-II experiments

Set-up #	BC[a]	Loading block bottom	Reinforcement type[b]	Pre-crack radius (mm)	Results
1	SS1	Flat	CFM	60	
2	SS2	Flat	CFM	60	Fig. A1.4, Fig. A1.12
3	SS2	Flat	MD/CFM/MD	60	Fig. A1.5, Fig. A1.13
4	SS2	Curved	MD/CFM/MD	60	Fig. A1.6, Fig. A1.14
5	SS2	Curved	MD/CFM/MD+LC	50	Fig. A1.7, Fig. A1.15
6	SS2	Curved	MD/CFM/MD	40	Fig. A1.8, Fig. A1.16
7	SS2	Curved	MD/CFM/MD	40[c]	Fig. A1.9, Fig. A1.17
8	SC1	Curved	MD/CFM/MD	40, 80	Fig. A1.10, Fig. A1.11, Fig. A1.18, Fig. A1.19, Fig. A1.20, Fig. A1.21
9	SC2	Curved	MD/CFM/MD	40, 80	Section 3.3.1

[a] Four different boundary conditions (BCs) were selected:

- SS1: simply supported, with a radius of 175 mm.
- SS2: simply supported, with a radius of 150 mm (see Fig. A1.1).
- SC1: semi-clamped, with an elastic boundary and a 150-mm support radius (see Fig. A1.2).
- SC2: semi-clamped, with a rigid boundary and a 150-mm support radius (see Fig. 3.3).

[b] Three different laminate layups were selected:

- CFM: 12 layers of continuous filament mats.
- MD/CFM/MD: 14 layers of continuous filament mats and 6 layers of multi-axial sewed fabrics (see Fig. 3.1).
- MD/CFM/MD+LC: 14 layers of continuous filament mats and 6 layers of multi-axial sewed fabrics, with 2 additional layers (0/90°) of uniaxial carbon fiber fabrics (LC) with a 40-mm radius locally reinforcing the bottom center of the plate.

[c] This case employed a ring-shaped pre-crack with inner and outer radii of 15 and 40 mm, respectively.

Set-ups #1 – 7 employed simply supported (SS) boundary conditions (BC) with different support radii (i.e., SS1 with a 175-mm support radius and SS2 with a 150-mm support radius), for comparison of different BCs. Each set-up contained one specimen, with modified layups and configurations (see Table A1.1). In these experiments, however, the specimens always failed in flexural before adequate crack propagation. Fig. A1.1 shows the photograph and assembly diagram from Set-up #6 as an example.

Set-up #8 included a semi-clamped (SC) BC similar to that employed in the final experiments in Chapter 3, with however less rigidity (SC1, see Fig. A1.2). Consequently, slight rotation and vertical displacement along the specimen edge was observed during loading. This set-up contains four specimens that were nominally identical to the 2D specimens described in Section 3.2.2.1, three of which contained a pre-crack with a 40-mm radius (labeled CP1, 2 & 3), and the other one contained a pre-crack with an 80-mm radius (labeled CP4). The final experimental set-up employed in Chapter 3 is referred to as Set-up #9, using a rigid SC condition (SC2). The assembly diagram is presented in Fig. A1.3.

All experiments were performed on a Zwick 500-kN universal testing machine (±1.0% relative error of accuracy and ±0.5% relative resolution in force measurement) in laboratory conditions (23 ± 5 °C and 50 ± 10% RH) under displacement control at a rate of 1 mm/min. A Linear Variable Differential Transformer (LVDT, model WA10 from HBM, with ± 0.2% accuracy) was installed below the specimens, except for those from Set-up #1 and #2, to measure the deflection at bottom center (hereafter referred to as "deflection").
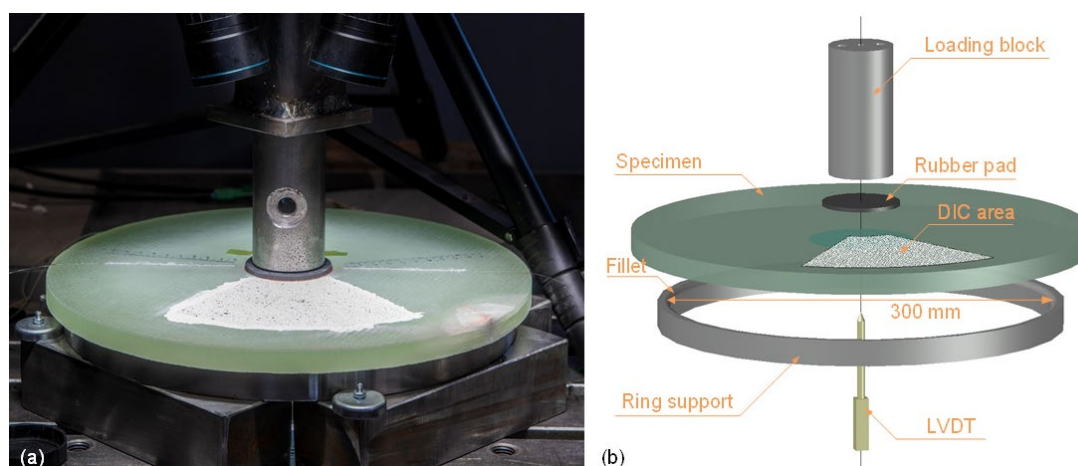
Fig. A1.1. Set-up #6 with a simply supported boundary (SS2, 150-mm support radius): (a) photograph and (b) assembly diagram.
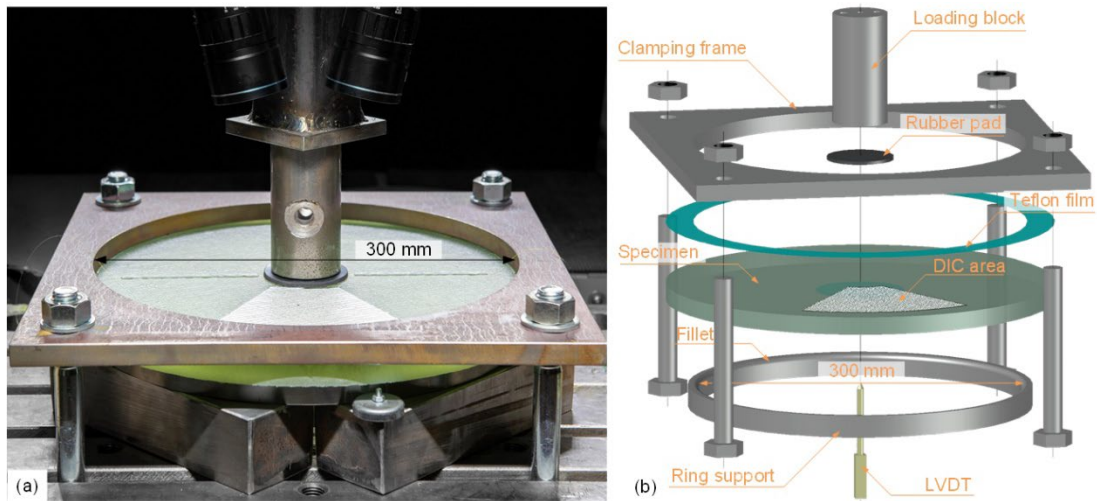
Fig. A1.2. Set-up #8 with semi-clamping elastic boundary (SC1): (a) photograph and (b) assembly diagram.
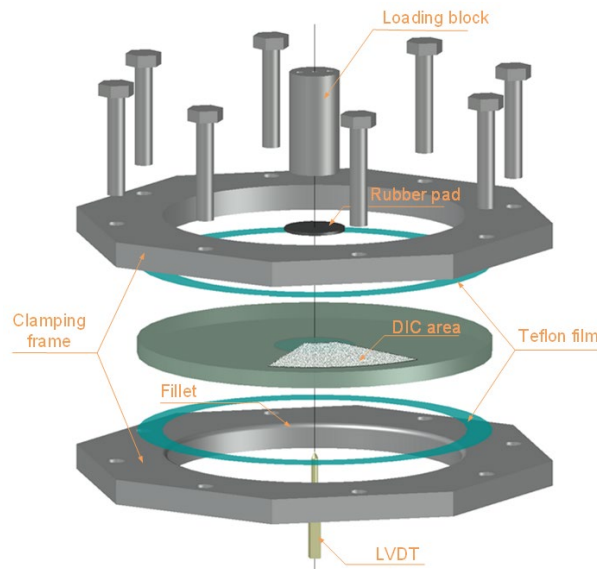
Fig. A1.3. Set-up #9 with semi-clamped rigid boundary (SC2): assembly diagram.

A1.2 Crack propagation pattern and failure mode

The crack propagation pattern and failure mode from Set-ups #2 – 8 are shown in Fig. A1.4 – 11. As can be seen from the figures, the SS boundary only allowed limited crack propagation before the flexural failure.
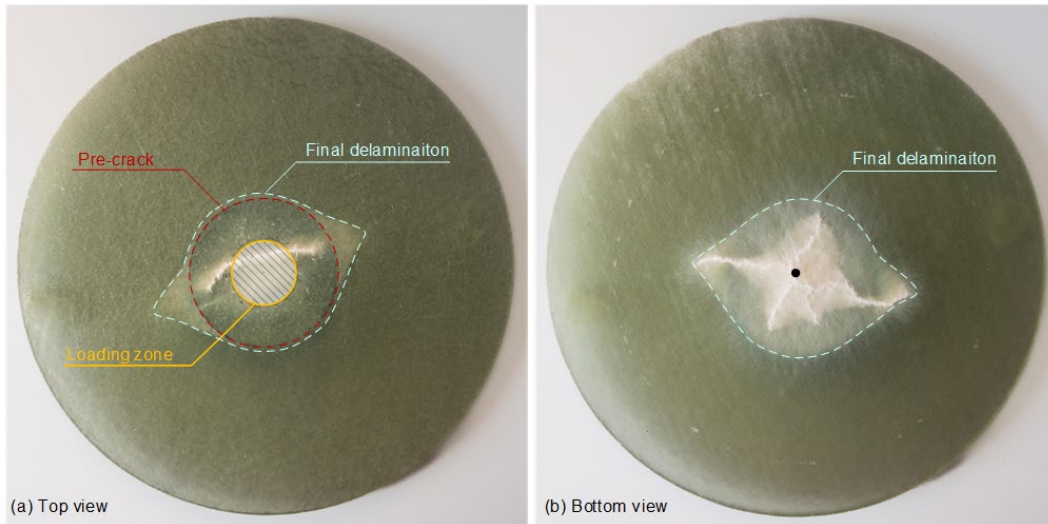
Fig. A1.4. Crack propagation pattern and failure mode of specimen using Set-up #2.
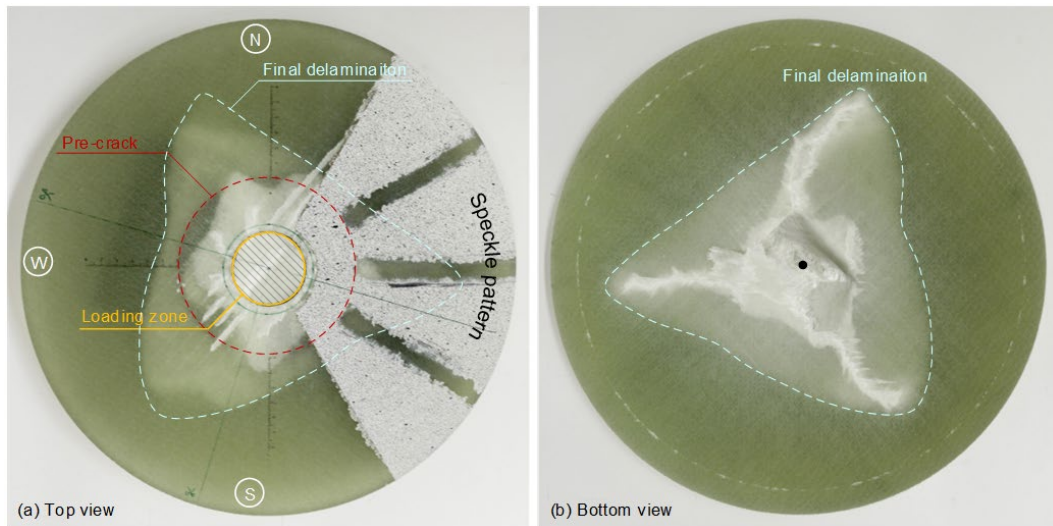
Fig. A1.5. Crack propagation pattern and failure mode of specimen using Set-up #3.
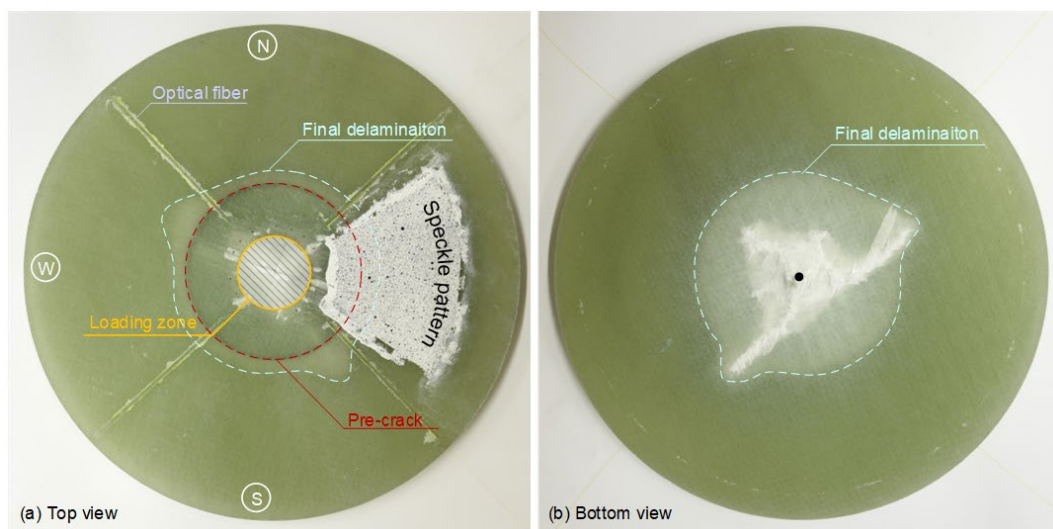
Fig. A1.6. Crack propagation pattern and failure mode of specimen using Set-up #4.
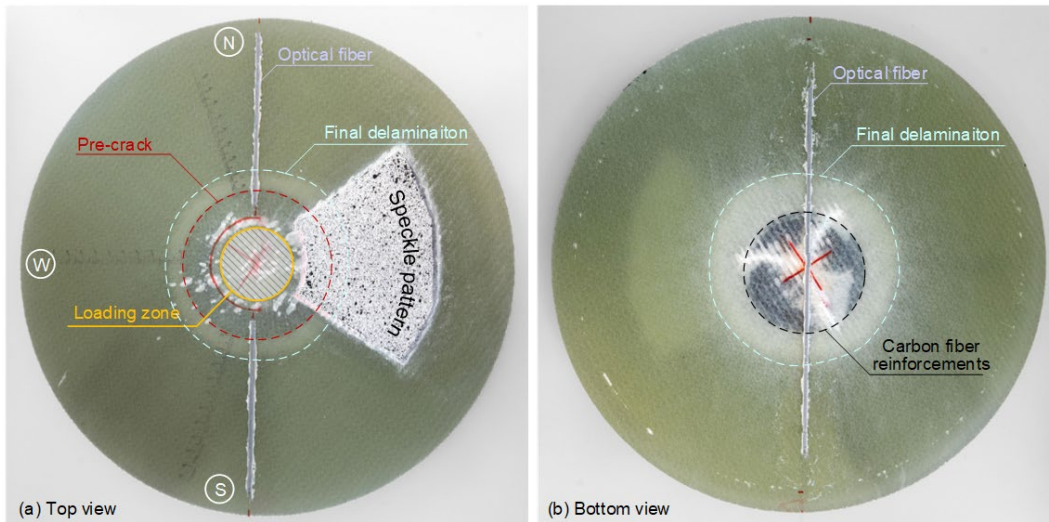
Fig. A1.7. Crack propagation pattern and failure mode of specimen using Set-up #5.
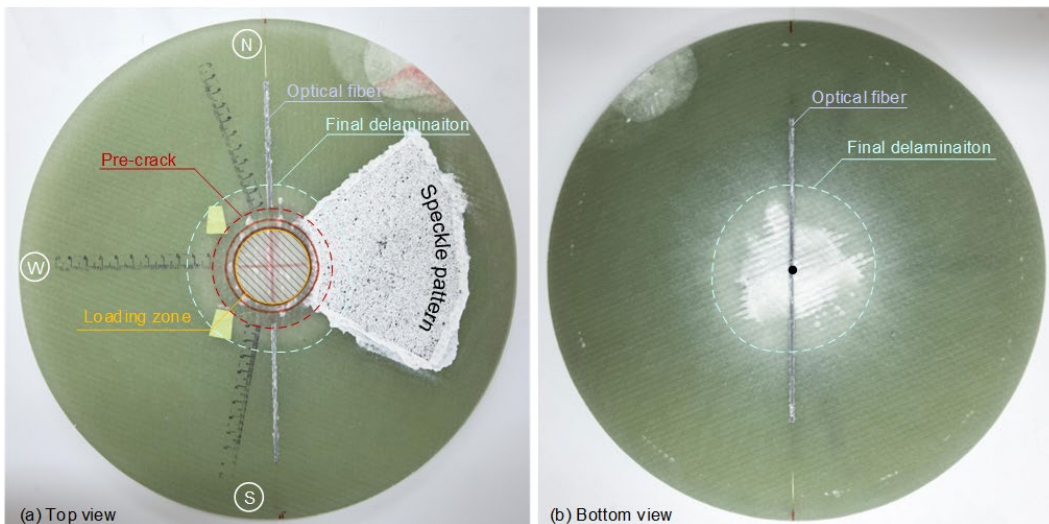
Fig. A1.8. Crack propagation pattern and failure mode of specimen using Set-up #6.
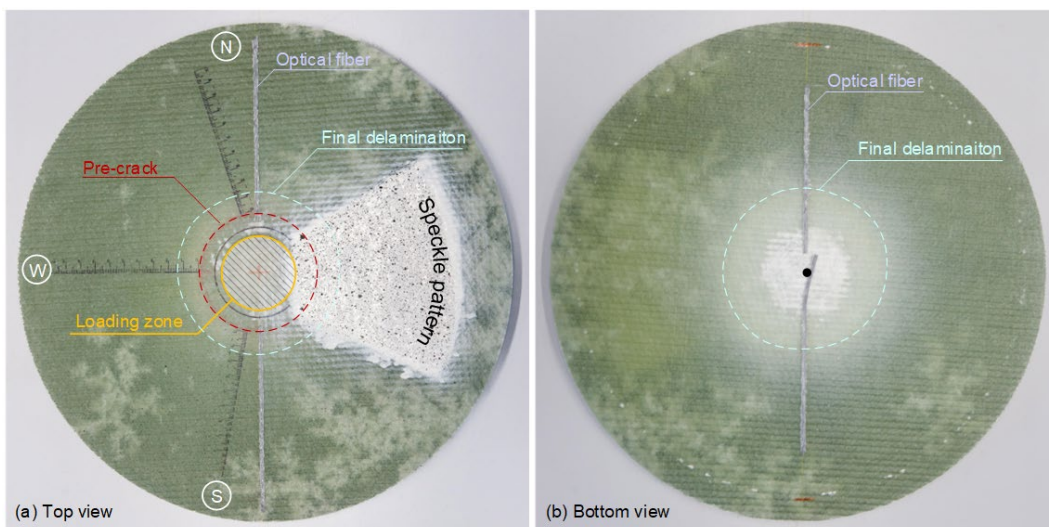
Fig. A1.9. Crack propagation pattern and failure mode of specimen using Set-up #7
(The random white pattern indicates voids resulting from subpar fabrication quality).
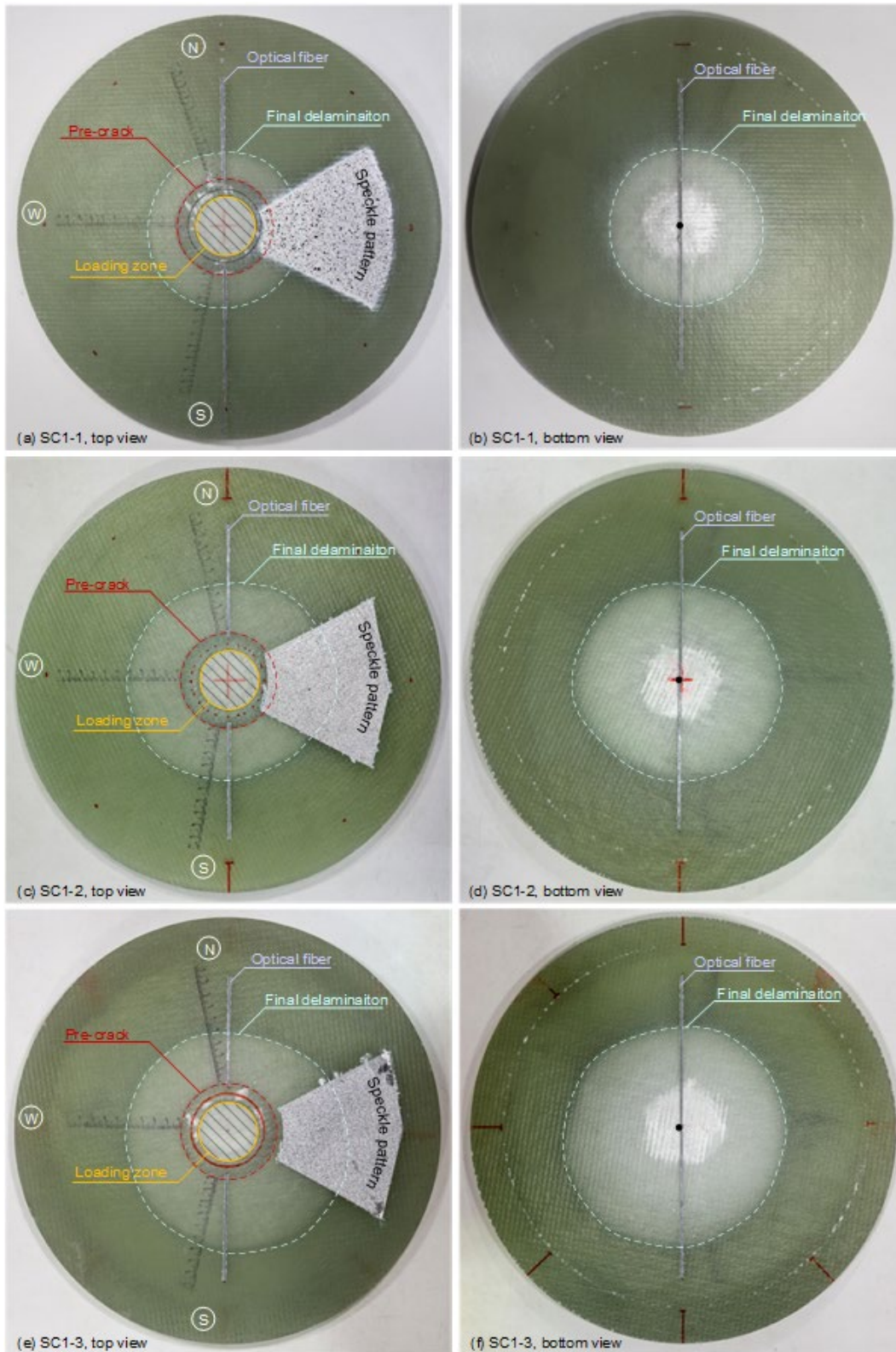
Fig. A1.10. Crack propagation pattern and failure mode of Specimen SC1-1, SC1-2 and SC1-3 (pre-crack radius: 40 mm) using Set-up #8.
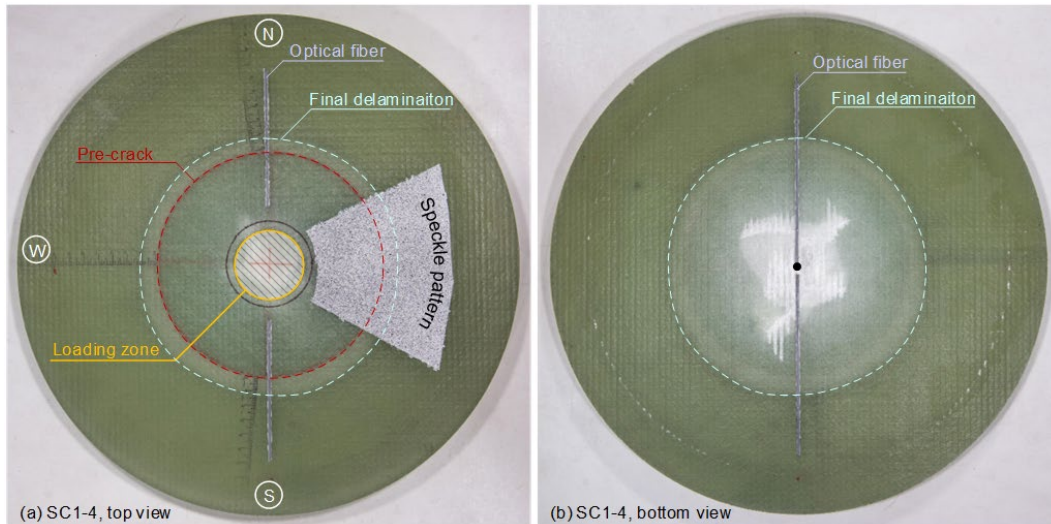
Fig. A1.11. Crack propagation pattern and failure mode of Specimen SC1-4 (pre-crack radius: 80 mm) using Set-up #8.

A1.3 Load, deflection and crack propagation

The load-deflection (load vs machine displacement for Set-up #2) curves from the experiments using Set-ups #2 – 8 are shown in Fig. A1.12 – 15. Crack propagation in the north, west and south directions (N, W and S respectively) in the experiments using Set-ups #3 – 8 is additionally presented in the corresponding figures. Set-up #1 and #2 achieved little crack propagation during loading, and consequently the crack length results are not shown.
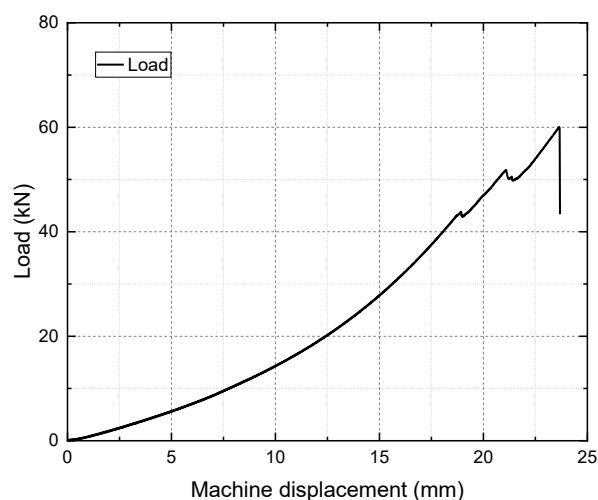
Fig. A1.12. Load vs machine displacement curve for specimen using Set-up #2.
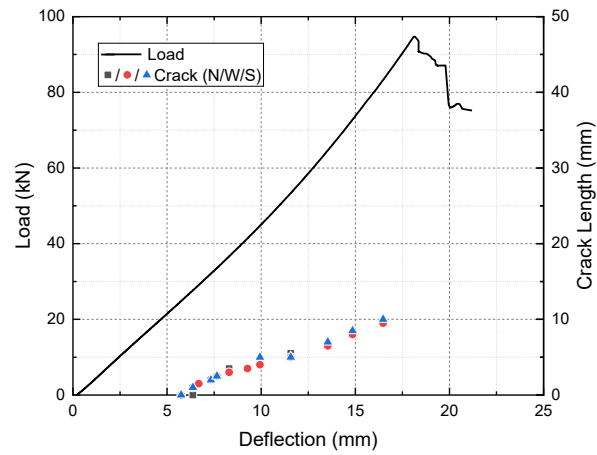
Fig. A1.13. Load and crack length vs deflection curves for specimen using Set-up #3.
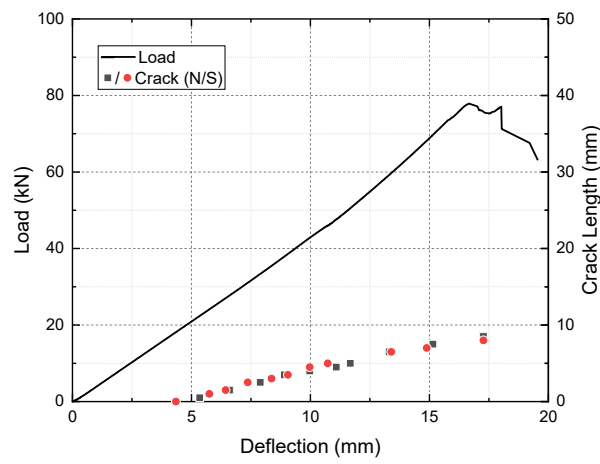
Fig. A1.14. Load and crack length vs deflection curves for specimen using Set-up #4.
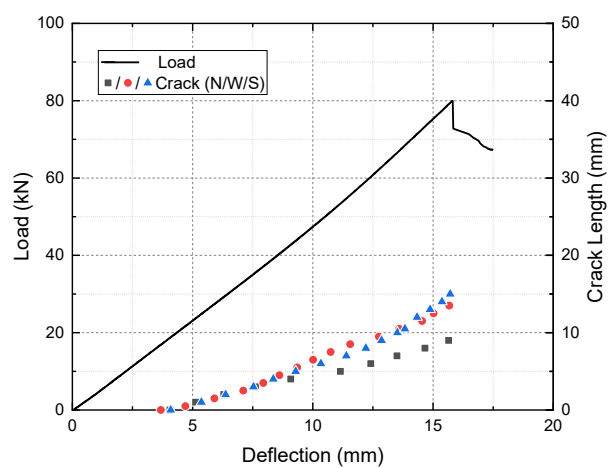
Fig. A1.15. Load and crack length vs deflection curves for specimen using Set-up #5.
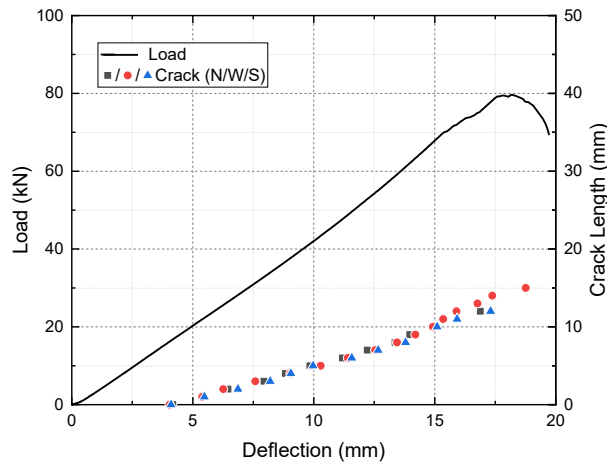
Fig. A1.16. Load and crack length vs deflection curves for specimen using Set-up #6.
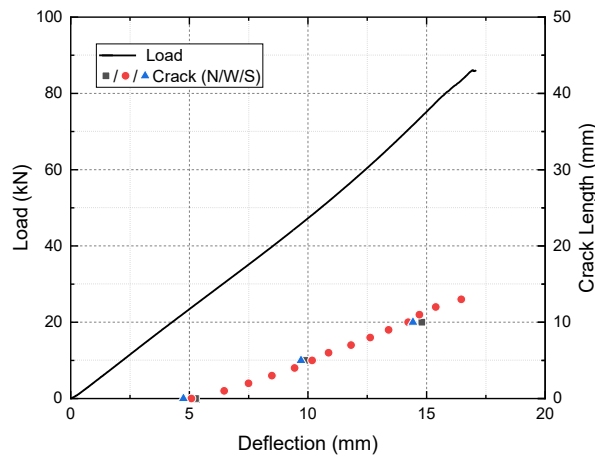
Fig. A1.17. Load and crack length vs deflection curves for specimen using Set-up #7.
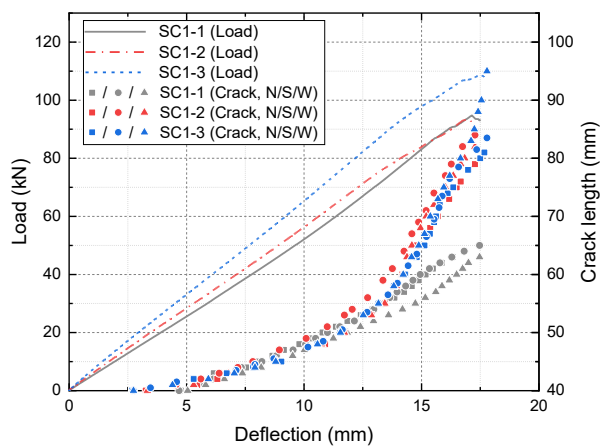
Fig. A1.18. Load and crack length vs deflection curves for Specimen SC1-1, SC1-2 and SC1-3 (pre-crack radius: 40 mm) using Set-up #8.
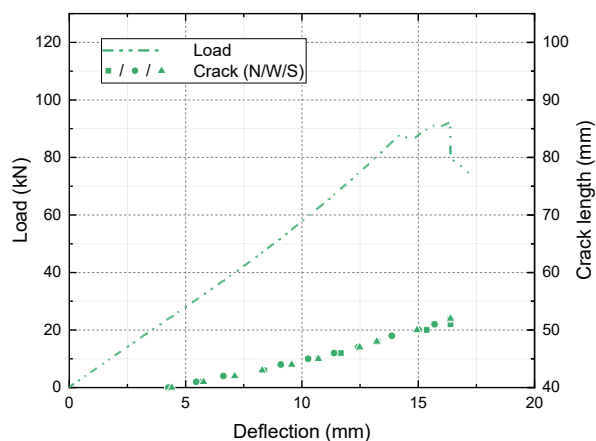
Fig. A1.19. Load and crack length vs deflection curves for Specimen SC1-4 (pre-crack radius: 80 mm) using Set-up #8.

A1.4 Effect of elastic clamping boundary

During the loading process involving Set-up #8, bending deformation was found in the steel frame used for clamping due to insufficient thickness and overlong fixing spans (see Fig. A1.2). Thus, the vertical and rotational displacements along the specimen edge were only partially constrained, as shown in Fig. A1.20.
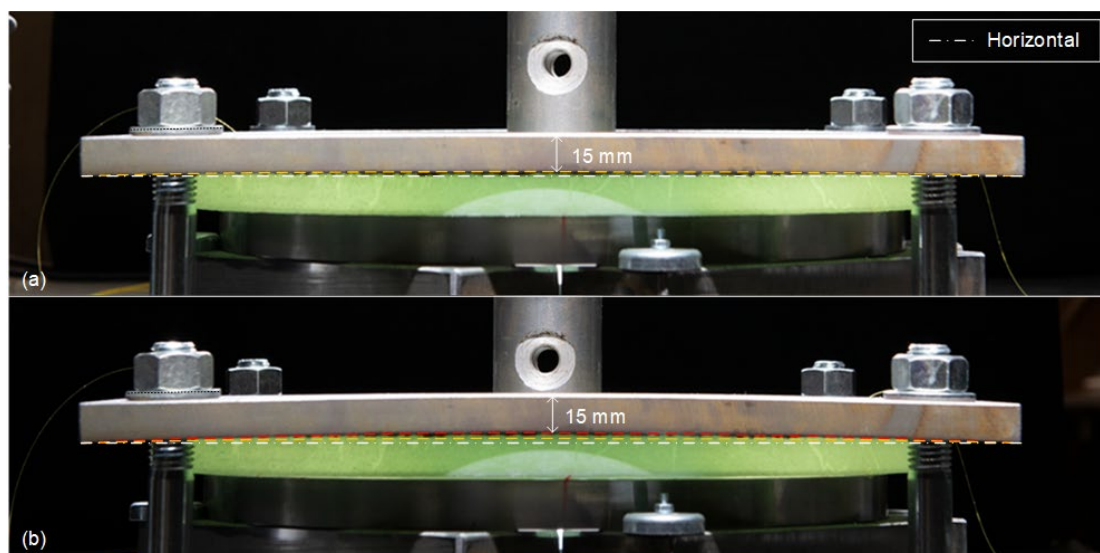
Fig. A1.20. Frame deformation in Set-up #8 at deflections of (a) 2 mm and (b) 14 mm.

Such constraints exhibited several impacts on the experimental results. First of all, compared with a fully SC condition (Set-up #9), the specimens showed lower overall stiffness and consequently slower crack propagation. Secondly, the plate deflections were distributed closer to plate edge due to the rotation (i.e. the deformation was less

intense in the center), and lower stretching was presented since less radial elongations could be found in the delaminated part at the same central deflections. Finally, it resulted in certain softening behavior at crack initiation and early propagation, as shown in see Fig. A1.21.
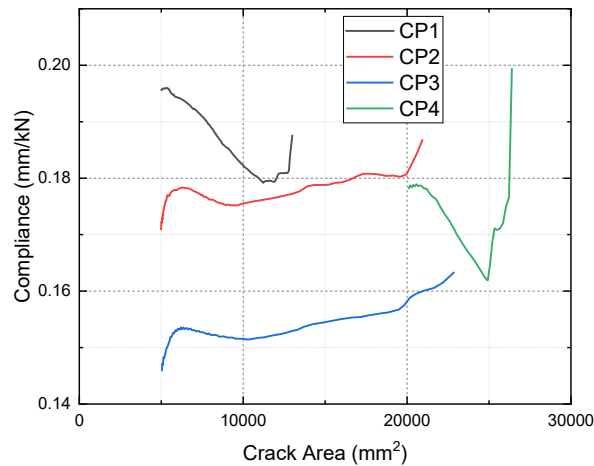
Fig. A1.21. Compliance (δ/P, δ being deflection and P load) vs crack area (calculated using average crack lengths in N, W and S directions) for specimens using Set-up#8.

References

[1]   Wang C, Vassilopoulos AP, Keller T. Two-dimentional Mode-II delamination experiments on glass-fiber composite laminates. Mendeley Data, 2023. doi: 10.17632/p4rc97wd7f.1.

Appendix A2

Supplementary results for 2D Mode-II experiments

A2.1 Introduction

This appendix presents supplementary data and results from the 2D Mode-II delamination experiments described in Chapter 3, including the delamination pattern, failure mode, surface deflection curves at different load levels, and surface radial strain distributions at different crack lengths, for all specimens. Detailed experimental data can be found in Ref. [1].

A2.2 Delamination pattern and failure mode

The delamination pattern and failure mode of all 2D specimens are shown in the following figures:
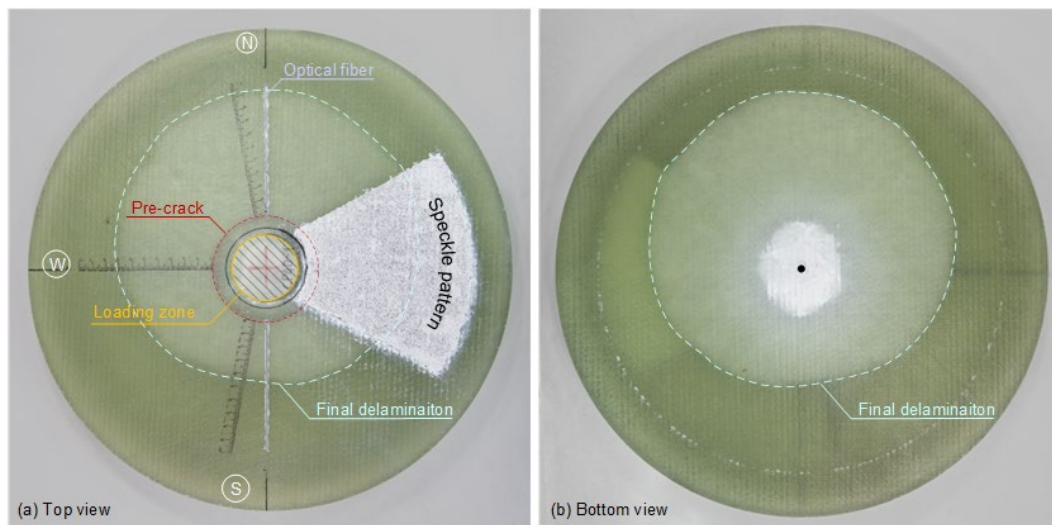
Fig. A2.1. Delamination pattern and failure mode of Specimen CP40-1.
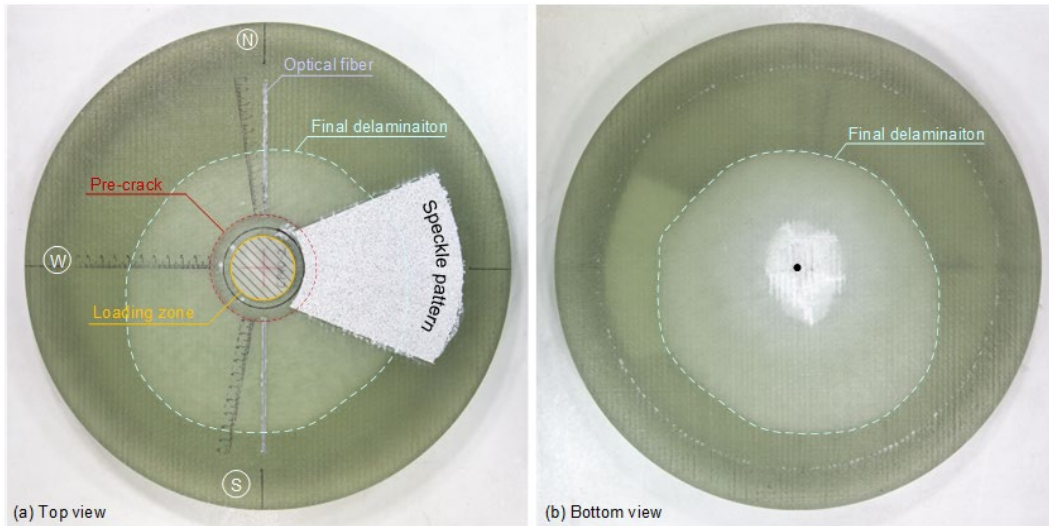
Fig. A2.2. Delamination pattern and failure mode of Specimen CP40-2.
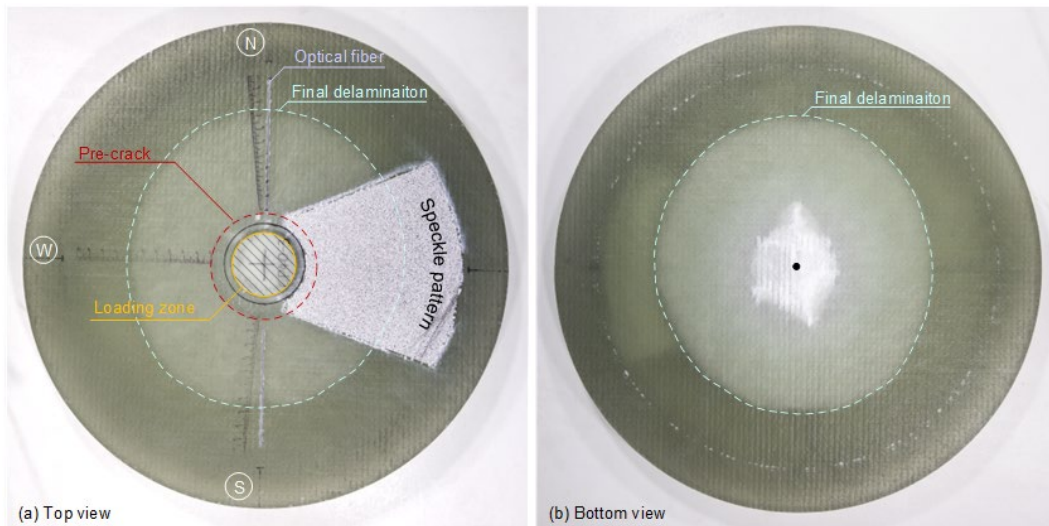
Fig. A2.3. Delamination pattern and failure mode of Specimen CP40-3.
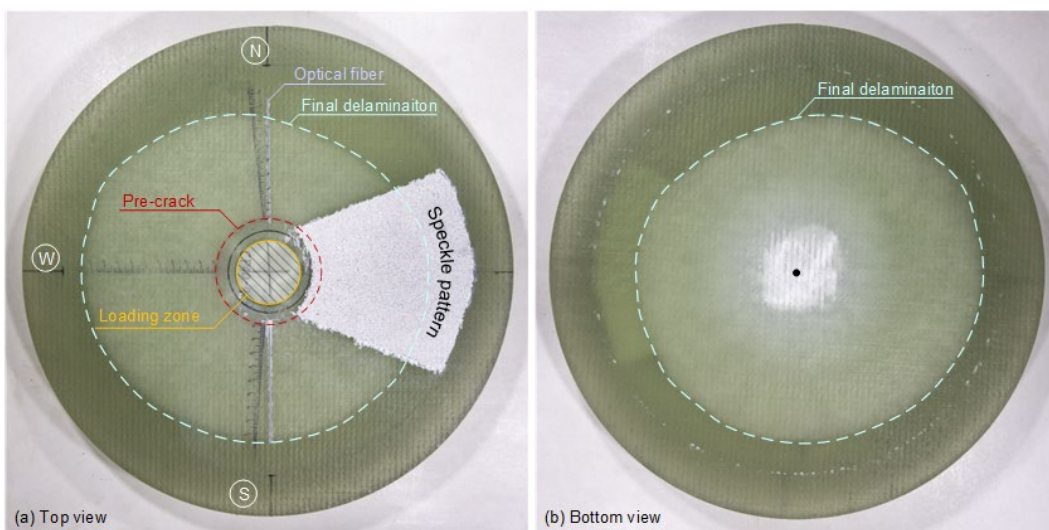
Fig. A2.4. Delamination pattern and failure mode of Specimen CP40-4.
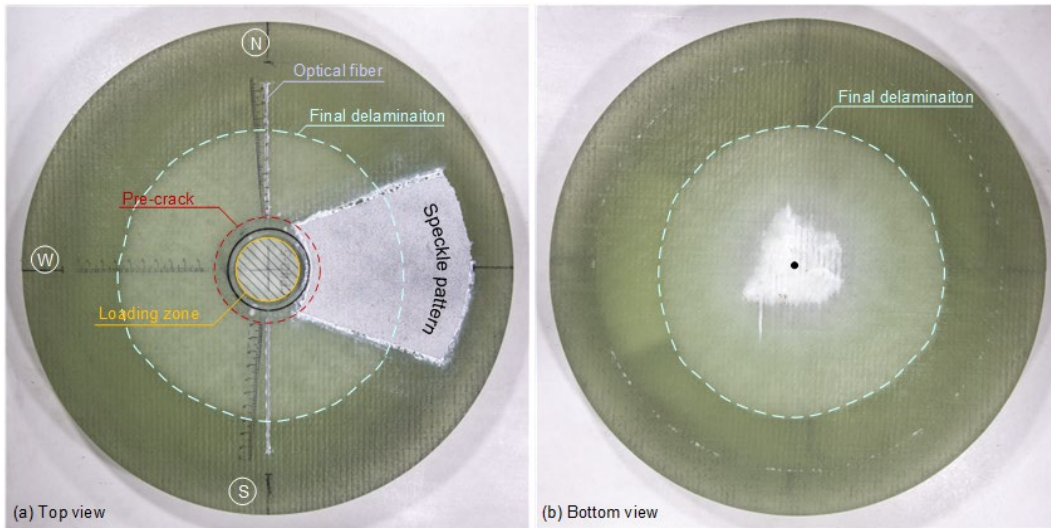
Fig. A2.5. Delamination pattern and failure mode of Specimen CP40-5.
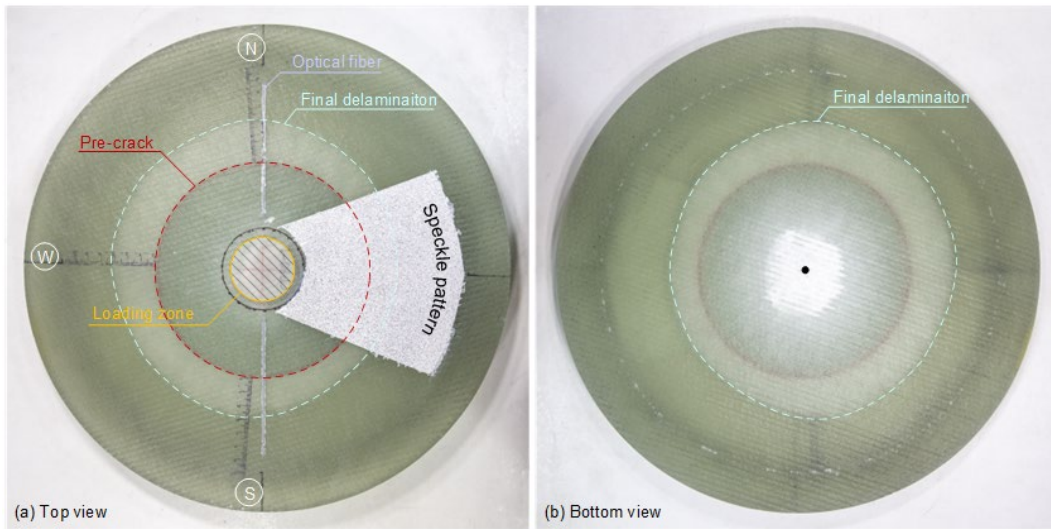
Fig. A2.6. Delamination pattern and failure mode of Specimen CP80-1.
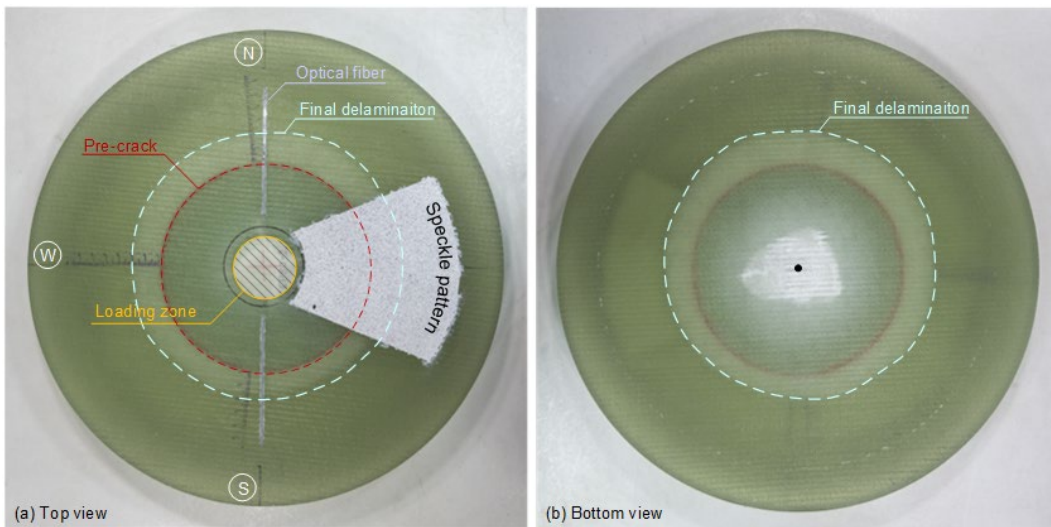
Fig. A2.7. Delamination pattern and failure mode of Specimen CP80-2.
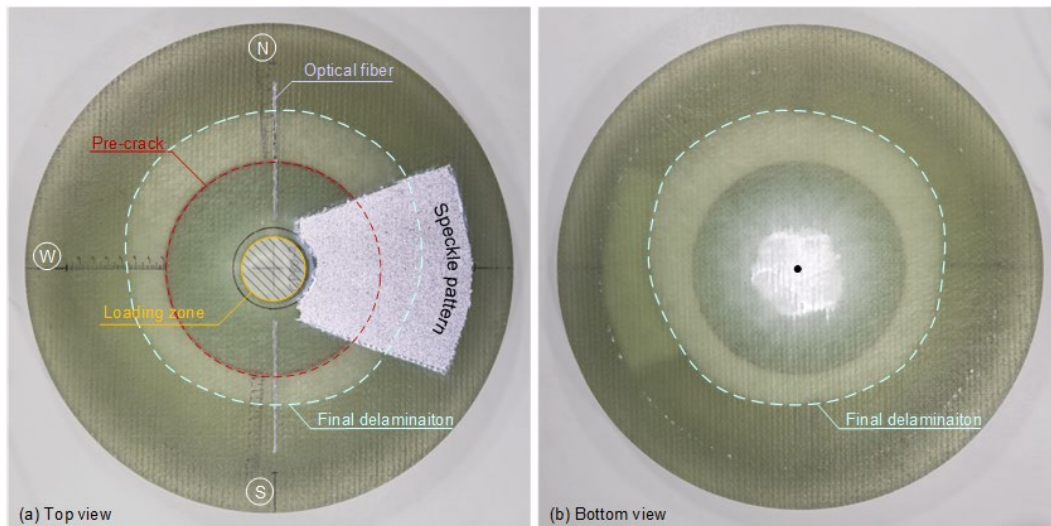
Fig. A2.8. Delamination pattern and failure mode of Specimen CP80-3.

A2.3 Surface deflections

The top-surface defections (w) along radial coordinates (r), measured from the DIC system (VIC-3D from Correlated Solutions, with ± 1.0 μm displacement measurement resolution), were plotted at different load levels (i.e., different plate deflections at bottom center, δ) for all 2D Mode-II delamination specimens, as shown in Fig. A2.9 – 16. The exact crack tip locations are not marked in the figures, considering that the crack lengths in this region, where paintings for DIC analysis blocked direct observation, cannot be deduced from the crack propagation behavior in other directions due to the asymmetric delamination growth in most specimens.
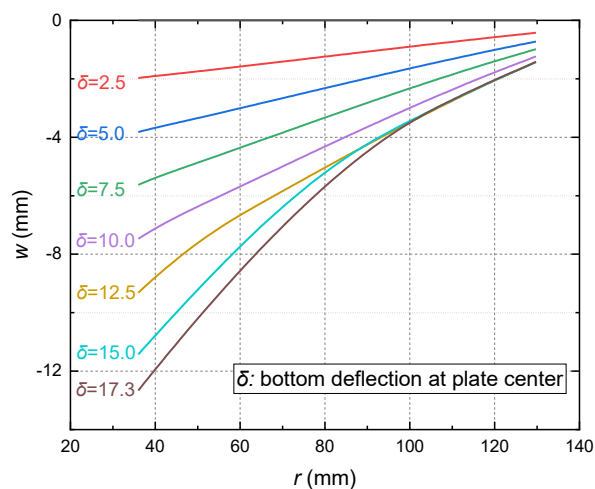
Fig. A2.9. Deflections (w) along radial coordinates (r) for Specimen CP40-1.
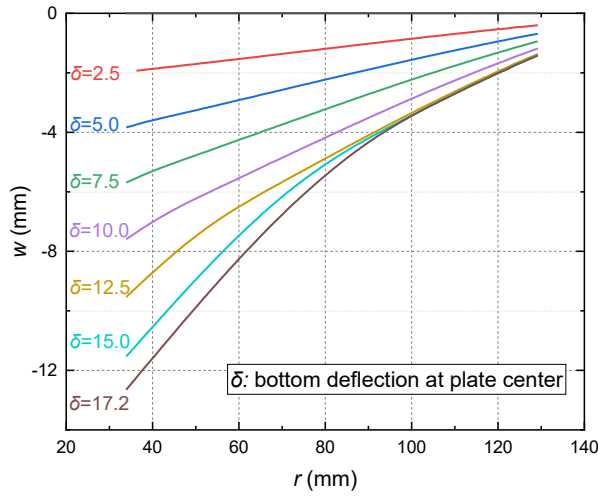
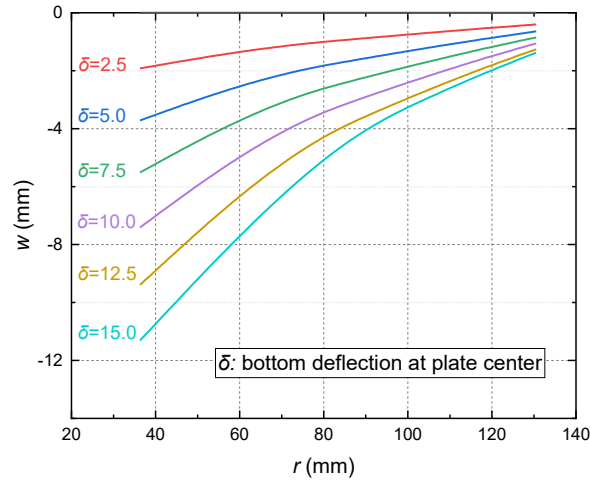Fig. A2.10. Deflections (w) along radial coordinates (r) for Specimen CP40-2.
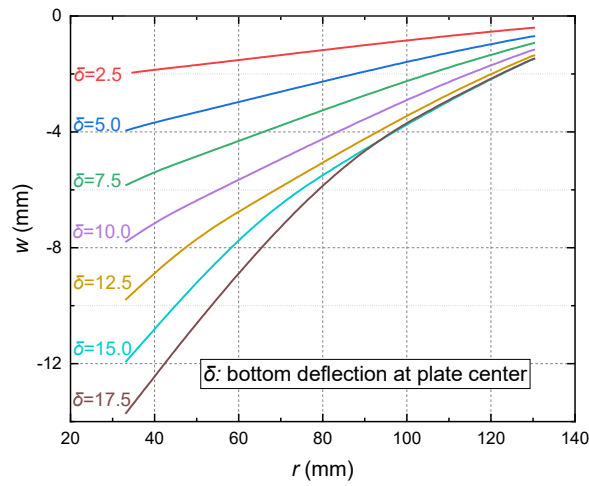
Fig. A2.11. Deflections (w) along radial coordinates (r) for Specimen CP40-3.
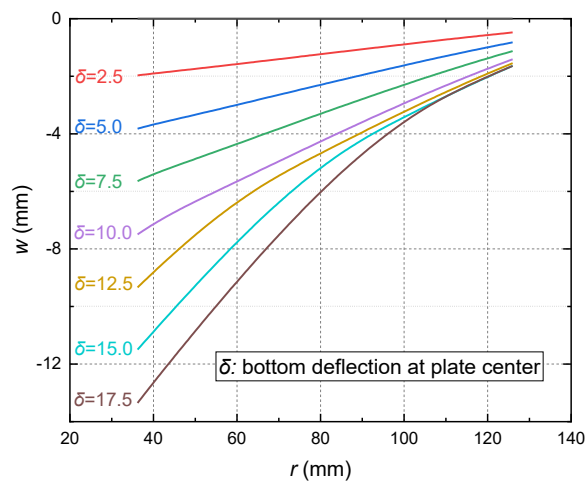
Fig. A2.12. Deflections (w) along radial coordinates (r) for Specimen CP40-4.
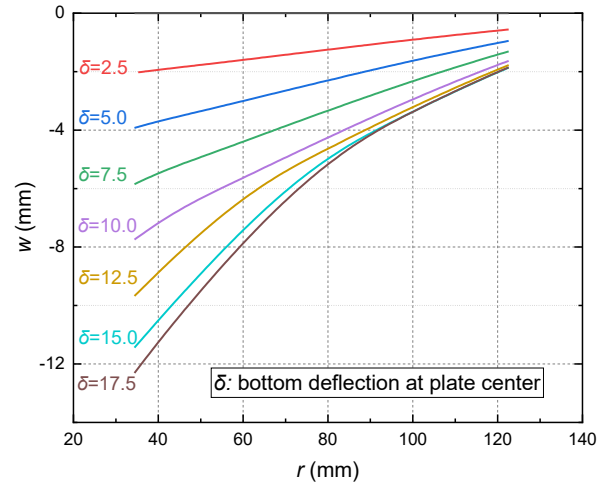
Fig. A2.13. Deflections (w) along radial coordinates (r) for Specimen CP40-5.
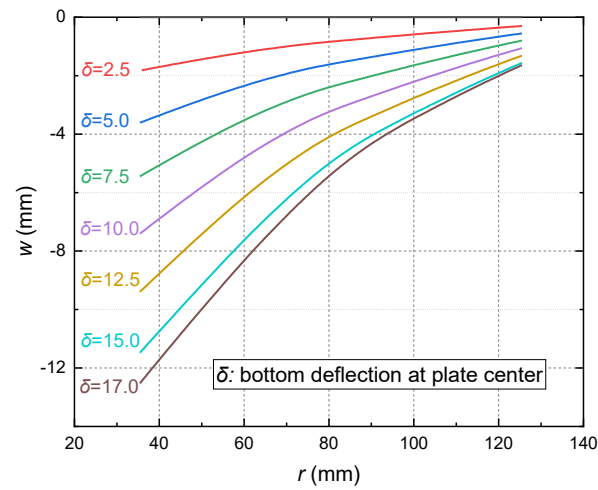
Fig. A2.14. Deflections (w) along radial coordinates (r) for Specimen CP80-1.
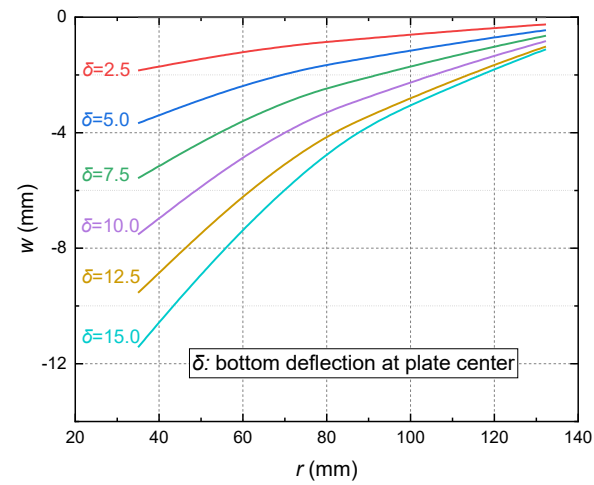
Fig. A2.15. Deflections (w) along radial coordinates (r) for Specimen CP80-2.

Fig. A2.16. Deflections (w) along radial coordinates (r) for Specimen CP80-3.

A2.4 Surface radial strains

The radial strains on the specimens' top surfaces along radial coordinates, measured from the fiber optic system (ODiSI-6100 system from LUNA, with ±25 $\mu\epsilon$ system accuracy and ±25 $\mu\epsilon$ measurement uncertainty), were plotted at different crack lengths for all 2D Mode-II delamination specimens, as shown in Fig. A2.17 – 24. The crack tip locations in the measured directions are marked on the curves.
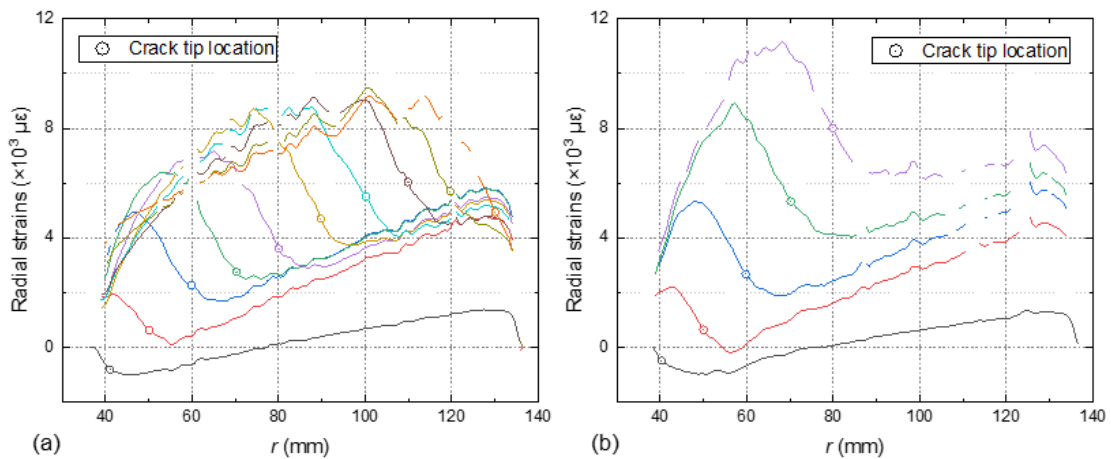
Fig. A2.17. Radial strains along radial coordinates (r) on Specimen CP40-1 top surface at different crack lengths: (a) north (N) direction and (b) south (S) direction.
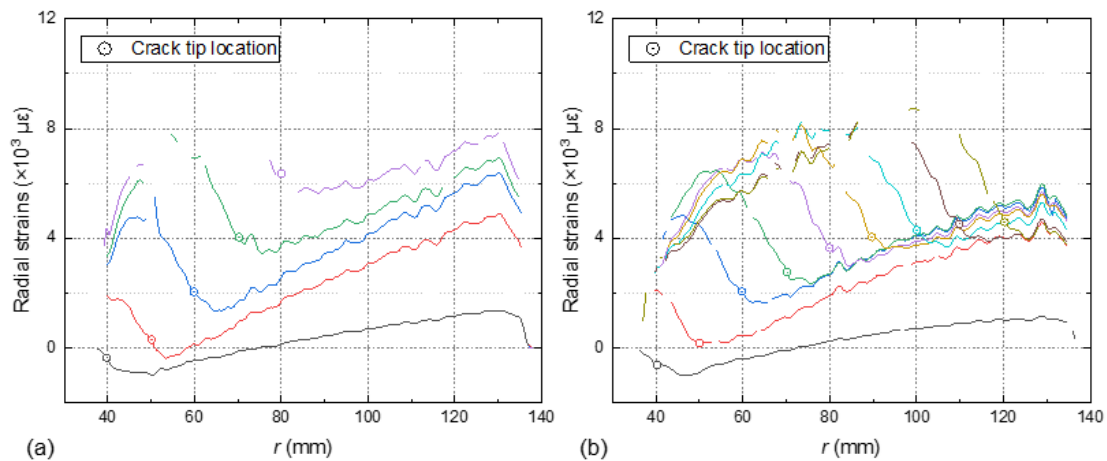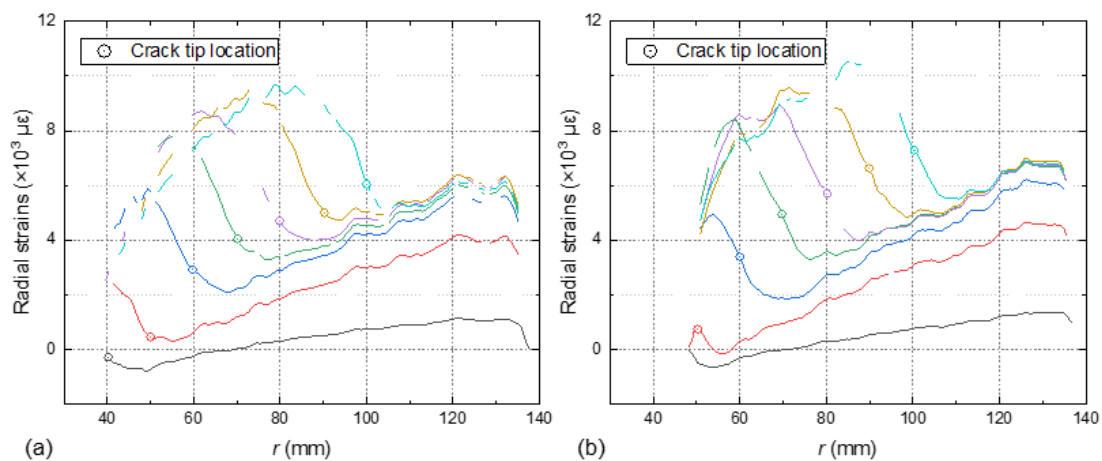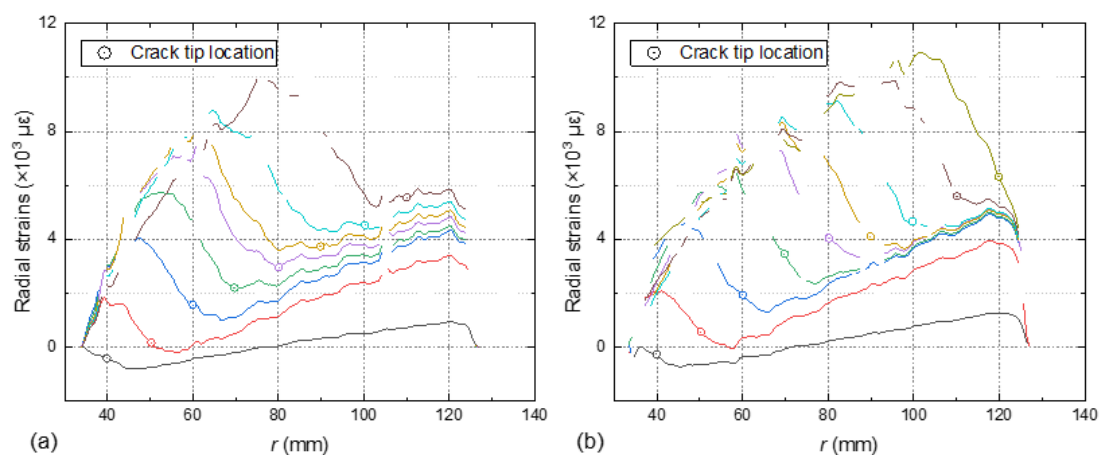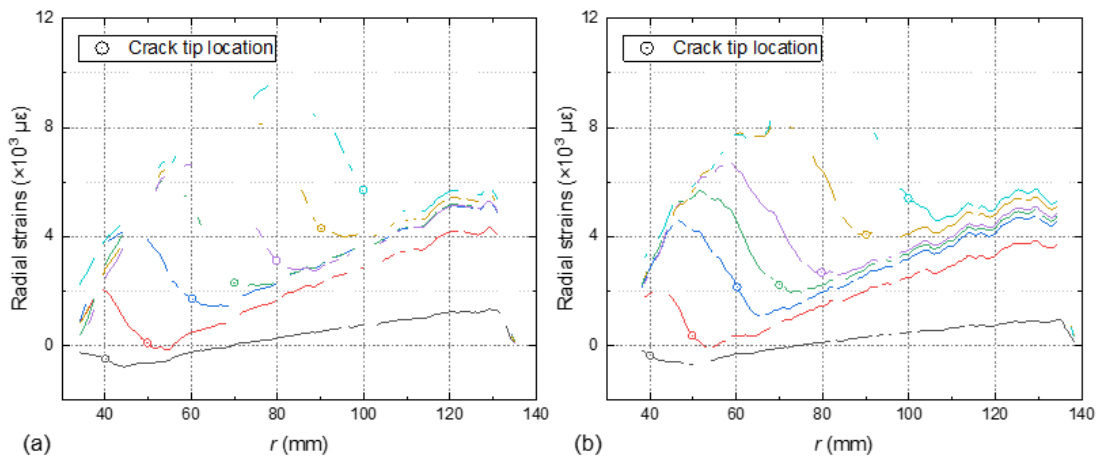
Fig. A2.18. Radial strains along radial coordinates (*r*) on Specimen CP40-2 top surface at different crack lengths: (a) north (N) direction and (b) south (S) direction.

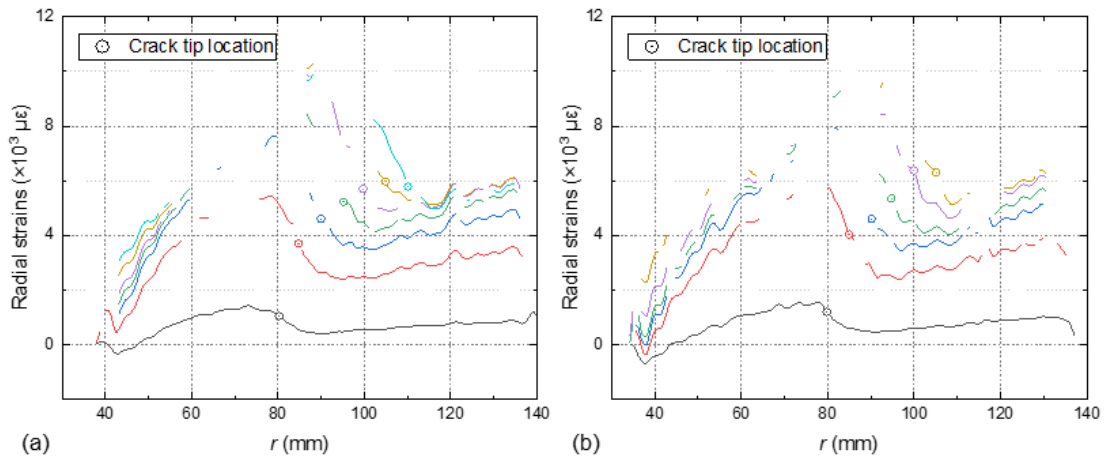
Fig. A2.19. Radial strains along radial coordinates (*r*) on Specimen CP40-3 top surface at different crack lengths: (a) north (N) direction and (b) south (S) direction.

Fig. A2.20. Radial strains along radial coordinates (*r*) on Specimen CP40-4 top surface at different crack lengths: (a) north (N) direction and (b) south (S) direction.

Fig. A2.21. Radial strains along radial coordinates (*r*) on Specimen CP40-5 top surface at different crack lengths: (a) north (N) direction and (b) south (S) direction.

Fig. A2.22. Radial strains along radial coordinates (*r*) on Specimen CP80-1 top surface at different crack lengths: (a) north (N) direction and (b) south (S) direction.
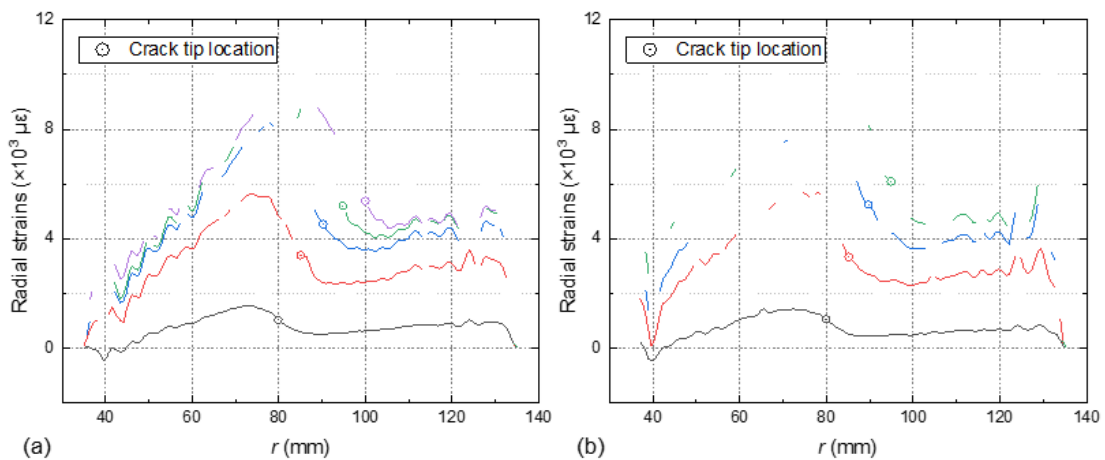

Fig. A2.23. Radial strains along radial coordinates (*r*) on Specimen CP80-2 top surface at different crack lengths: (a) north (N) direction and (b) south (S) direction.
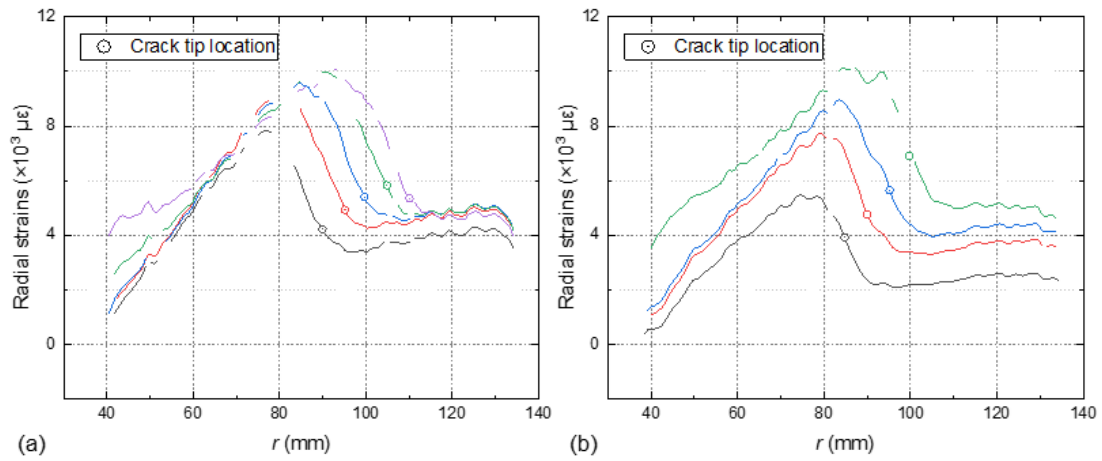
Fig. A2.24. Radial strains along radial coordinates (*r*) on Specimen CP80-5 top surface at different crack lengths: (a) north (N) direction and (b) south (S) direction.

References

[1]   Wang C, Vassilopoulos AP, Keller T. Two-dimentional Mode-II delamination experiments on glass-fiber composite laminates. Mendeley Data, 2023. doi: 10.17632/p4rc97wd7f.1.

Appendix A3

Determination of parallax error for 2D Mode-II specimens

As mentioned in Chapter 3, the measurements of the crack lengths in 2D Mode-II experiments were facilitated by the translucency of the laminates, allowing direct visual observation from above. However, parallax errors were introduced into the crack length measurements due to the difference in depths of the delamination plane and the top surface where the rulers were stamped on.

The parallax errors were compensated using the procedure described as follows. First, initial crack length values, a', in the three ruler directions were read from the video with neglecting the parallax error. Then, the radial and vertical displacements along a radial path in the area of interest were extracted from DIC measurements and correlated with the average a' to obtain the deformation curves of the top surface at certain a'. The corresponding deformation curves of the delamination plane were subsequently determined and plotted together with the top surface curves and crack tip locations for certain a'. According to the position of the camera lens (which was vertically above the ruler in the W direction), the lines of sight for given tip locations could be drawn for the W and N/S direction respectively, as shown in Fig. A1. Finally, the parallax error for each selected a' value can be obtained from the figure by assuming the sections were always perpendicular to the delamination plane (neglecting the additional rotation of sections due to shear). For each specimen, the parallax error was determined every 5-mm delamination growth, and linear interpolated in between. After excluding the parallax error, the measurements were considered as the real crack length, a, and no further iteration procedure for more precise evaluation of parallax error was carried out, since the difference between a' and a was small. Note that the deformation curves of the plate derived from DIC can be markedly different from those in the ruler directions for highly asymmetric cases (see specimen CP40-2 in Fig. 3.5 for example), but such difference (in the vertical displacement and rotation of sections) was again neglected, since the resulted shift in parallax error calculation was insignificant.
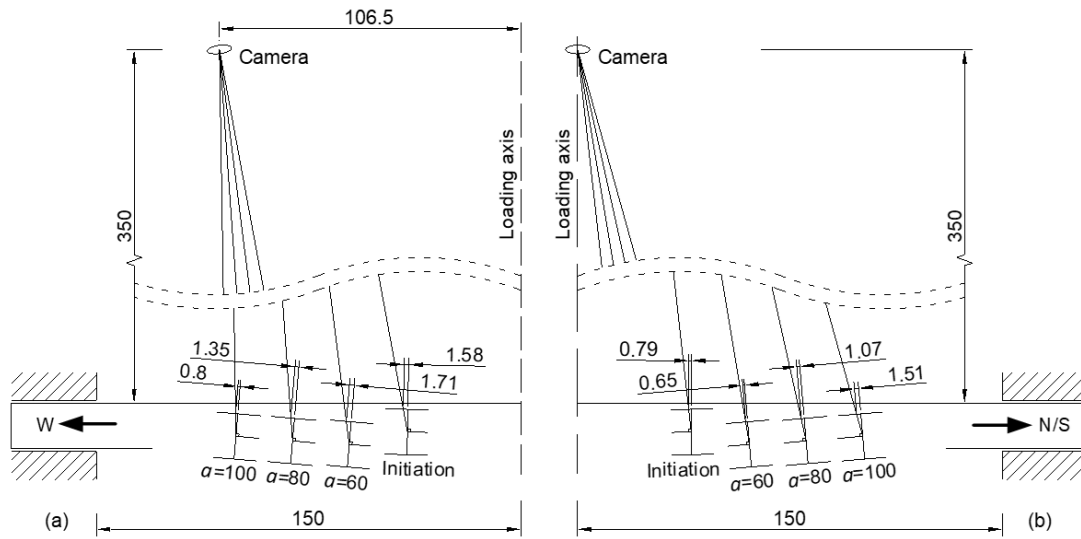
Appendix A3

Fig. A1. Determination of parallax error in specimen CP40-3 along the (a) W and (b) N/S directions (unit: mm).

Appendix A4

Flexural damage process in 2D Mode-II specimens

In 2D Mode-II experiments (Chapter 3), while all plates experienced flexural failure at the bottom center, the progressive damage process had a minimal impact on the structural performance before the abrupt rupture, as evidenced by monitoring videos recorded from below.

Examples of specific damage states in specimen CP40-3 are shown in Fig. A2. The damage onset occurred at a deflection of 12.4 mm, which can be identified by the more contrasting stripe pattern shown in Fig. A2b compared to the undamaged state (Fig. A2a), indicating fiber-matrix interface damage in the outmost layer. Intermittent noise could be heard subsequently. As presented in Fig. 3.7, for specimen CP40-3, the rapid crack propagation stage started at a deflection of around 11.3 mm, which confirms that the tensile damage onset was not responsible for the transition of the stages. Accordingly, the subsequent changes in the structural behavior were considered to be resulted from the delamination growth. The rupture of the outmost layers, as shown in Fig. A2c, took place at a deflection of 16.5 mm accompanied by a loud sound, which corresponds well to the ultimate deflection (16.2 mm). After that, the broken region soon expanded, causing secondary failure in the upper sub-laminate (Fig. 3.6).

A radial path in the area of interest from DIC measurements was selected to extract the top-surface deflections every 10-mm crack propagation. The results for specimen CP40-3 were plotted in Fig. A3. The curves present not only the vertical positions, but also the shape changes of the top surface during the delamination-growth history. The impact of the flexural failure on the structural response can be thus explained as follows. Note that a segment of the curve at the crack length of 100 mm moved upwards compared to that at 90 mm, indicating that the tensile damage at the bottom center was large enough to break the material continuity, releasing a certain extent of the rotation constrains at the center like a hinge, which consequently changed the curvature distribution along the surface. The crack length of 100 mm corresponds to a deflection of 16.4 mm. A further investigation of this phenomenon revealed that the reverse displacement of the plate surface firstly occurred at a deflection of 15.9 mm (corresponding to an average crack length of 95 mm, exactly the point where the crack length plots scattered, see Fig. 3.7), close to the ultimate deflection (16.2 mm). To

conclude, the bottom tensile damage only started to play an important role on the structural behavior after the "hinge" was generated near the flexural failure at a deflection of 15.9 mm.
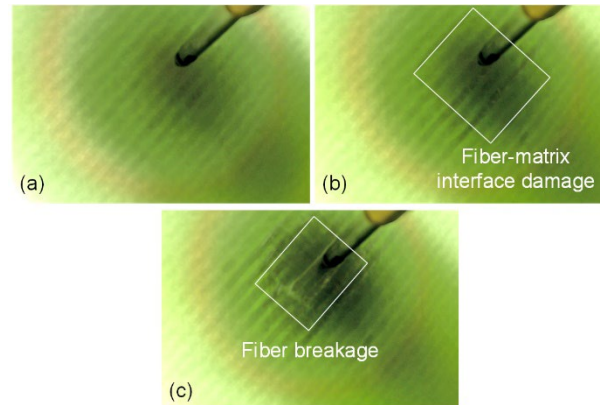

Fig. A2. Video screenshots monitoring bottom damage in specimen CP40-3, taken at (a) undamaged state, (b) damage onset (δ=12.4 mm) and (c) rupture (δ=16.5 mm).
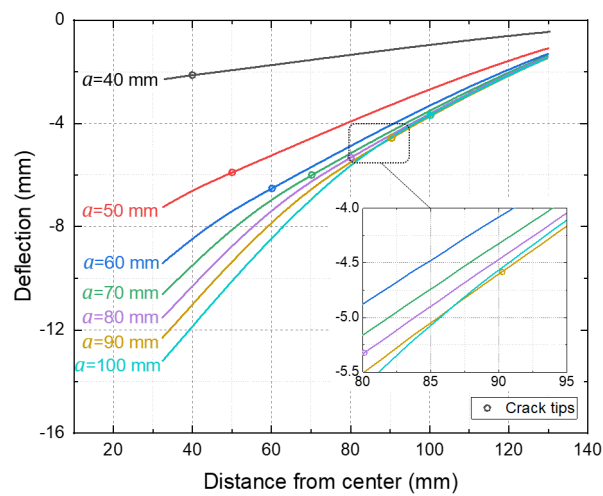

Fig. A3. Deflections vs radial coordinates at different crack propagation states for specimen CP40-3, measured on top surface.

Appendix B1

Constitutive relationships of CFM and MD laminates

The constitutive relationships of the CFM and MD laminates, obtained from tensile tests [1] under displacement control at a rate of 1 mm/min, are shown in Fig. B1.1. According to the figure, both laminates exhibited nonlinearity from an early stage due to progressive damage in the matrix. In the finite element simulations in Chapter 4, this material nonlinearity was modeled as plasticity, input in a tabular form after converting the nominal strain/stress data into true strain/stress data. The failure of the material was not considered for the sake of simplicity, and the laminates were assumed to deform in perfect plasticity (see Fig. B1.1) after material strength was reached near the end of the loading process, whereas in the 2D experiments bending failure could be observed at the bottom center of the plate.
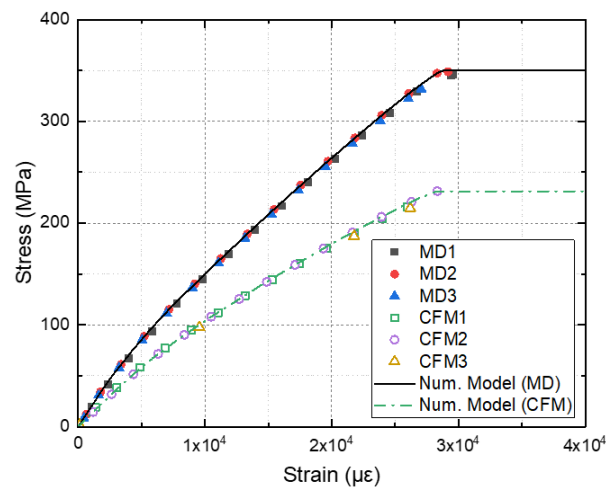

Fig. B1.1. Tensile experimental results for CFM and MD laminates (scatter plots). The curves denote corresponding material models employed in FE simulations.

The thickness of 1D and 2D Mode-II delamination specimens was high, and therefore the shear deformation should be considered for accurate numerical analysis. Double beam shear tests [2] were carried out on the CFM laminates, since CFM layers constituted the major contribution to the thickness of the delamination specimens. A total of five samples (IS1 to IS5) were prepared and loading using a W+B 50-kN universal testing machine under displacement control at a rate of 1 mm/min in

laboratory conditions (23 ± 5 °C and 50 ± 10% RH). The load-displacement results are shown in Fig. B1.2, where the curve of sample IS1 is omitted due to the accidental interruption of the loading. The resulting average interlaminar shear strength and modulus were 47.7 MPa and 0.62 GPa respectively, calculated using the data deduction methods suggested in Ref. [2].
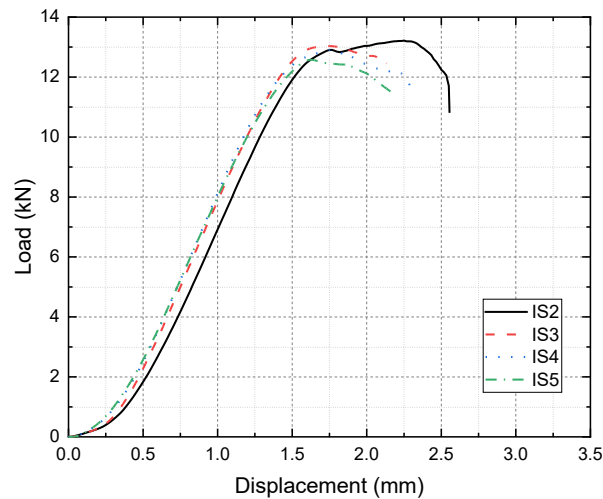

Fig. B1.2. Interlaminar shear test results for CFM laminates.

References

[1]   ISO 527-4:2021(E). Plastics — Determination of tensile properties — Part 4:Test conditions for isotropic and orthotropic fibre-reinforced plastic composites. 2021.

[2]   ISO 19927:2018. Fibre-reinforced plastic composites — Determination of interlaminar strength and modulus by double beam shear test. 2018.

Appendix B2

Iterative fitting of cohesive parameters

This appendix presents example increments during the iterative fitting process for cohesive modeling.

- Following the strategy shown in Fig. 4.10, the whole process started with fitting the 1D experiments, using inputs from the experimental results presented in Fig. 4.6b, i.e., $\{G_{\text{IIc}} = 8.1 \text{ kJ/m}^2, \sigma_m = 29 \text{ MPa}, \delta_2 = 0.19 \text{ mm}, \delta_f = 0.8 \text{ mm}\}$. As shown in Fig. B2.1, to achieve better fitting along the rapid propagation segment of the crack length curves, G_{IIc} was reduced from 8.1 to 6.7 kJ/m^2.
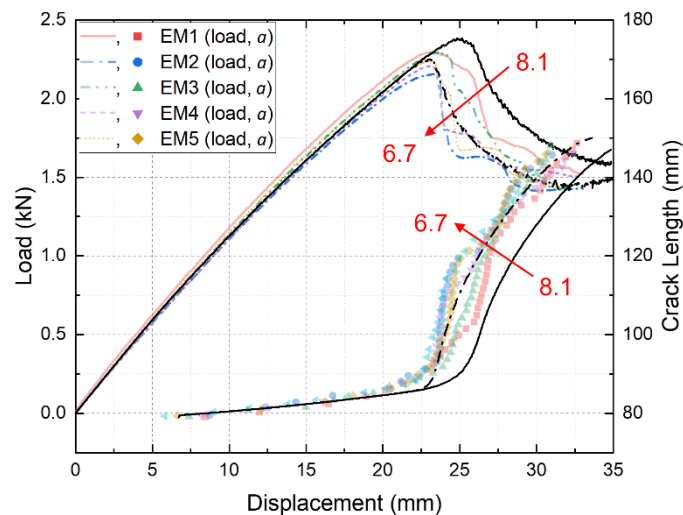

Fig. B2.1. Load and crack length vs displacement curves for 1D experiments, showing effects of fitting parameter G_{IIc}.

- Since the slope of the slow propagation segment in the fitted crack length curve shows reasonable agreement with the experiments, the subsequent adjustment was applied to parameter δ_2. By changing the value of δ_2 from 0.19 to 0.14, the crack length curve near the transition points now achieved a better fit, as shown in Fig. B2.2. However, in this increment, the rapid propagation segment of the crack length curve also shifted slightly, reflecting the coupling effects of parameters G_{IIc} and δ_2.
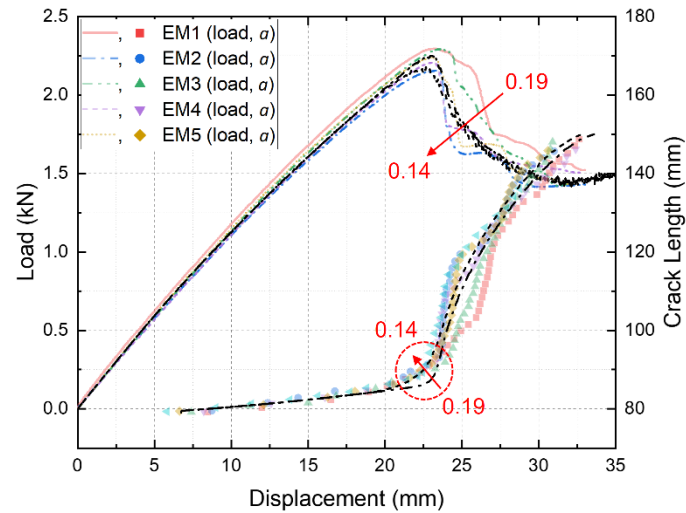
Fig. B2.2. Load and crack length vs displacement curves for 1D experiments, showing effects of fitting parameter δ_2.

- The modeling results also revealed an agreement between the FPZ length (not shown in the figures). Therefore, the adjustment of parameter δ_f was omitted, and the fitting loop went back to the adjustment of parameter G_{IIc}. After a few more loops, good agreement could be reached regarding the whole crack length curves as well as the FPZ length, and that parameter set, $\{G_{IIc} = 7.0$ kJ/m^2, $\sigma_m = 30$ MPa, $\delta_2 = 0.12$ mm, $\delta_f = 0.8$ mm$\}$, can be regarded as definite for the 1D experiments. Then, this parameter set could be employed as the inputs for the 2D experiments (Model 2a and 2b respectively, see Section 4.3.3).

Appendix B3

Microscopic microcracking behavior in Mode-II delamination

This appendix describes the microscopic fracture behavior in the microcracking zone of Mode-II delamination based on the model developed by Lee [1], providing supplementary theoretical derivation related to the findings in Section 4.5.1.
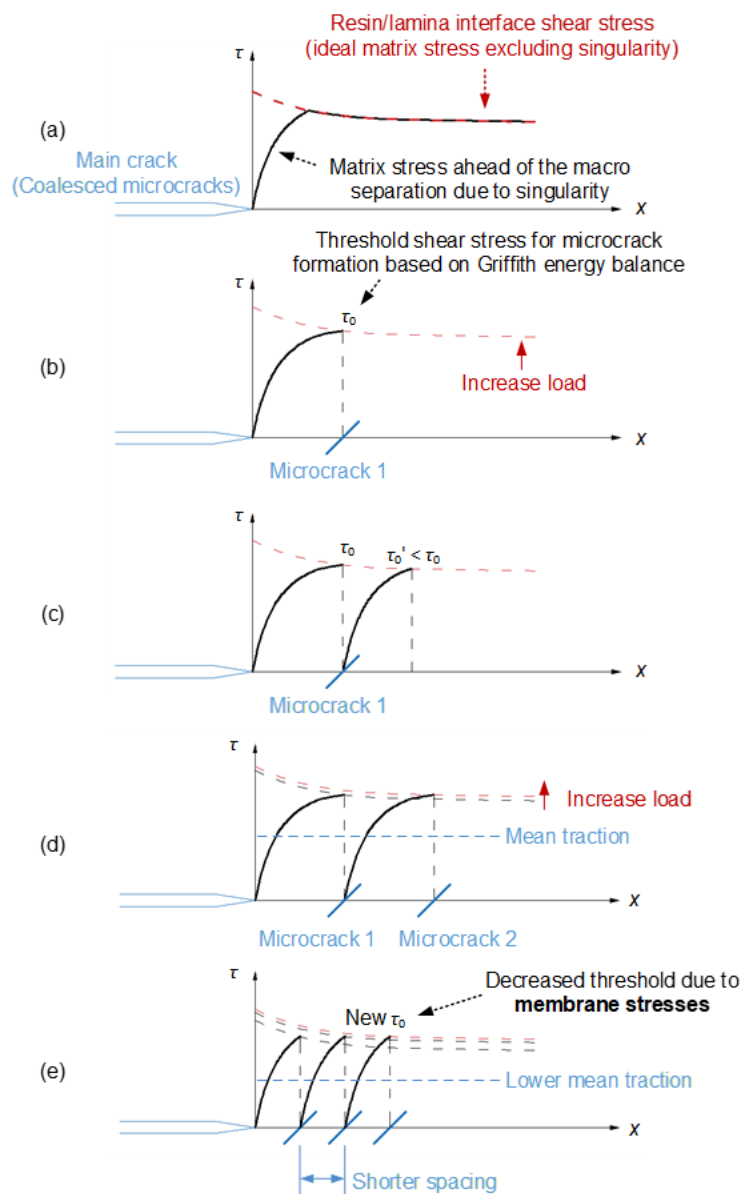

Fig. B3.1. Stress field in microcracking zone of Mode-II delamination.

Lee's model was originally developed to explain the microcracking behavior in ENF specimens, but also applicable to a more general case. The model simplifies the microcracking region in a laminated beam into a thin resin layer between two adherends, i.e., an adhesive joint. Based on simple beam theory and using the superposition principle, the shear stress along the adhesive interface near the main crack tip (the tip of the pre-crack or the macro crack coalesced by multiple microcracks), which is also the theoretical shear stress in the resin layer not considering the stress singularity, decreases exponentially towards the uncracked end. The actual matrix stress is however likely to increase from zero until matches the interfacial shear stress described above, and then follows the same trend, as shown in Fig. B3.1a. As the global loads increase, the exponentially decreasing interfacial stress also increase overall, until the maximum matrix stress reaches a threshold value, τ_0, that leads to the formation of Microcrack 1 (Fig. B3.1b), where τ_0 can be calculated based on the Griffith energy balance using the principal tensile stresses, the layer thickness and the Mode-I fracture toughness of the resin. A similar singular stress field will thus build up from Microcrack 1 and again intersects with the interfacial stress, at a value of τ_0' (Fig. B3.1c). Due to the exponential decreasing trend of the interfacial stress, τ_0' is slightly lower than τ_0, and therefore a new microcrack will not form unless further increasing the loads (Fig. B3.1d). Introducing tensile membrane forces into this system will result in a lower τ_0 for microcrack formation according to the Griffith energy balance. Consequently, microcracks will initiate at lower interfacial stress levels in such cases (i.e., 2D Mode-II delamination scenarios), leading to lower mean matrix stresses (i.e., mean shear traction) over the microcracking zone and shorter microcrack spacing (Fig. B3.1e). Lee also showed that the global G_{II} is inversely related to the mean microcrack spacing for typical fiber polymer composites. These findings coincide with the differences between the 1D and 2D Mode-II cohesive laws, see Fig. 4.9.

References

[1]   Lee SM. Mode II delamination failure mechanisms of polymer matrix composites. J Mater Sci. 1997;32(5):1287–95.

Appendix C

Mode-II delamination in mid-crack beam specimens

C.1 Introduction

This appendix presents a set of new 1D Mode-II delamination experiments and their results, which were not covered in the main chapters of this thesis.

As discussed in Chapter 3, the boundary conditions (BCs) in the 2D Mode-II delamination experiments at the crack wake (i.e., plate center) restricted the rotation and shear sliding of the sub-laminates, unlike standardized beam tests where split beam ends could freely rotate and slide. These differences are considered significant 2D effects affecting delamination behavior.

To further explore the impact of BCs on Mode-II delamination behavior, a series of 1D delamination experiments using mid-crack beam specimens were conducted, bridging the experimental studies using the developed 2D set-up and the 1D ELS set-up. The corresponding experimental data can be found in Ref. [1].

C.2 Experimental program

The same laminate layup and fabrication techniques described in Section 3.2.1 were used. Seven beam specimens were prepared, each measuring $400 \times 40 \times 16.9$ mm (length × width × height). A pre-crack was introduced to each specimen in the middle of the reinforcements during the layup process at the midspan. Table C.1 categorizes the specimens into three groups based on their BCs and pre-crack lengths. Specifically, Specimens SB40-1 and SB40-2 exhibited a pre-crack length of 2×40 mm and both ends were simply supported (SS, see Fig. C.1a). Specimens CB40-1 and CB40-2 also exhibited a pre-crack length of 2×40 mm but both ends were semi-clamped (SC, see Fig. C.1b), allowing longitudinal sliding, which was facilitated by applying Teflon films with graphite lubrication on the specimen surfaces. Lastly, Specimens CB80-1, CB80-2, and CB80-3 also utilised SC boundaries but with the pre-crack length doubled.

Table C.1. Specimen lists for mid-crack beam experiments.

Specimen	BC[a]	Pre-crack length ($2a_0$)
SB40-1, 2	SS	2 × 40 mm
CB40-1, 2	SC	2 × 40 mm
CB80-1, 2, 3	SC	2 × 80 mm

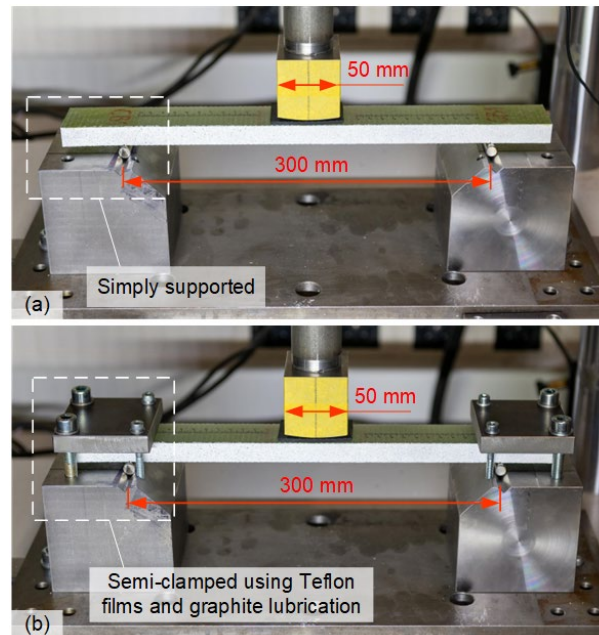[a] The span measured 300 mm for all specimens, except for Specimen SB40-2, which exhibited a span of 240 mm.

Fig. C.1. Experimental set-ups with different BCs: (a) SS (240-mm span for Specimen SB40-2) and (b) SC.

All specimens were loaded at the mid-span using a loading block measuring 50 mm in the longitudinal direction (equal to the loading block diameter in the 2D experiments) and supported at a distance of 300 mm (matching the support diameter in the 2D experiments). An exception was Specimen SB40-2, which had a support distance reduced to 240 mm to promote delamination growth before flexural failure. The bottom surface of the loading block was machined with curvature, and a rubber pad was inserted below it to reduce stress concentration in the specimens.

The experiments were conducted using a W+B 50-kN universal testing machine (±1.0% relative error of accuracy and ±0.5% relative resolution in force measurement) under displacement control at a rate of 1 mm/min in laboratory conditions (23 ± 5 °C and 50 ± 10% RH). The front lateral surfaces of the specimens were sprayed white with a random black speckle pattern to be monitored by a DIC system (VIC-3D from

Correlated Solutions, with ± 1.0 μm displacement measurement resolution) to measure the beam deflection at the mid-span and the strains. Rulers were stamped on the beam top surfaces on both half-spans, and crack propagation along the rulers was recorded by two video cameras from above for determination of the crack length (visual measurement with ± 1.0 mm accuracy).

C.2 Experimental results and discussion

C.2.1 Failure mode

The failure modes of the specimens are shown in Fig. C.2 – 8. Specimens SB40-1 and SB40-2 experienced significant flexural failure before achieving substantial crack propagation (Fig. C.2 & 3). The shorter support distance of Specimen SB40-2 (240 mm vs 300 mm) did not result in more propagation. Specimens CB40-1 and CB40-2 exhibited unstable delamination growth (jump growth) at early stages in one of the half-spans due to the short pre-crack length (Fig. C.4 & 5). In contrast, Specimens CB80-1, CB80-2, and CB80-3 displayed stable crack growth initially, thanks to the longer pre-crack length. However, they also experienced unstable growth in both half-spans during further loading (Fig. C.6, 7 & 8).
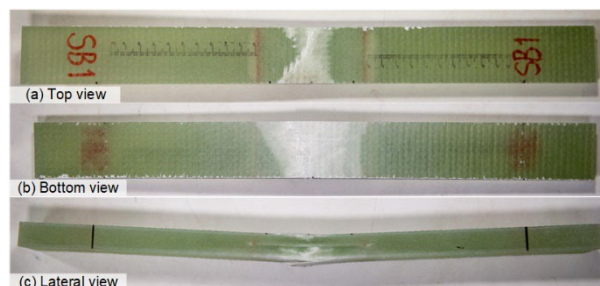

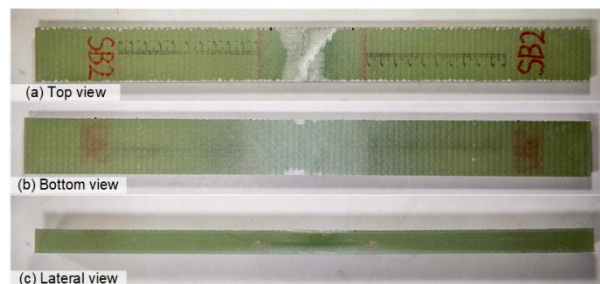Fig. C.2. Failure mode of Specimen SB40-1.
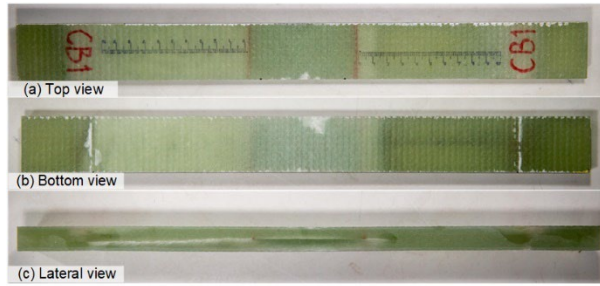

Fig. C.3. Failure mode of Specimen SB40-2.

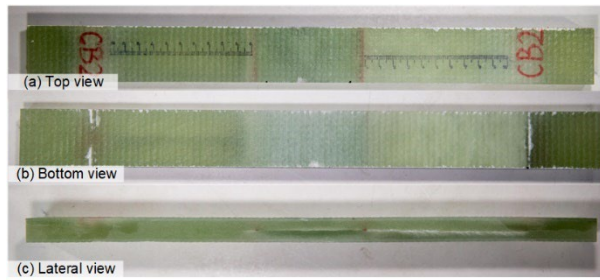Fig. C.4. Failure mode of Specimen CB40-1.

Fig. C.5. Failure mode of Specimen CB40-2.
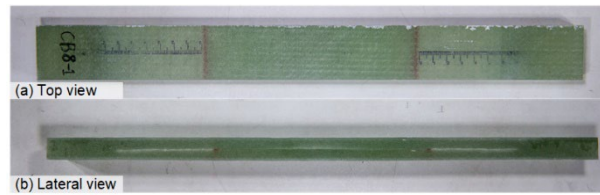

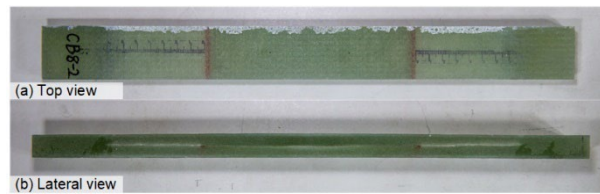Fig. C.6. Failure mode of Specimen CB80-1.
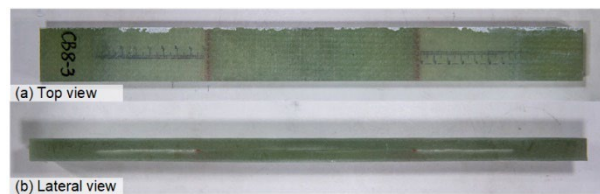

Fig. C.7. Failure mode of Specimen CB80-2.

Fig. C.8. Failure mode of Specimen CB80-3.

C.2.2 Load, deflection and crack propagation

The load versus deflection curves for all specimens are presented in Fig. C.9 – 11. Specimen SB40-2 exhibited larger flexural stiffness than Specimen SB40-1 due to the shorter span. The semi-clamped BC for Specimens CB40-1 and CB40-2 achieved higher stiffness and ultimate loads. However, stable crack propagation in the specimens with a 2 × 40 mm pre-crack was very limited, i.e., less than ~5 mm, therefore the crack length results for these specimens are not shown. Crack propagation in specimens CB80-1 and CB80-2 was stable and symmetric in the two half-spans in the first 10-mm length, after which the propagation rates deviated in the two half-spans, and the propagation in the right side became unstable. Specimen CB80-3 exhibited symmetric crack propagation in the two half-spans, which turned into unstable almost at the same time. In summary, unstable crack propagation only occurred in specimens with the SC boundary, leading to significant load drops.
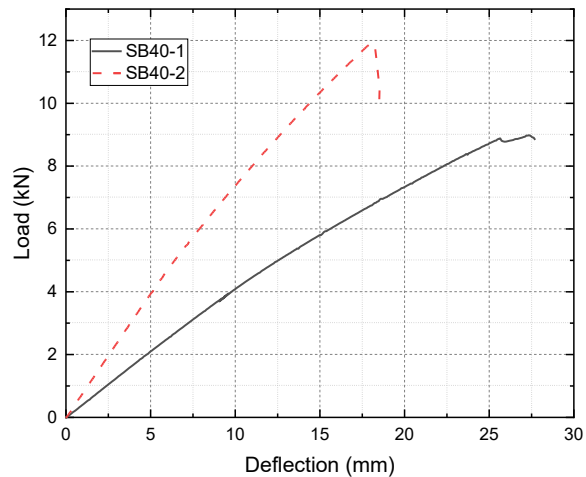

Fig. C.9. Load-deflection curves for Specimens SB40-1 (300-mm span) and SB40-2 (240-mm span).

Fig. C.10. Load-deflection curves for Specimens CB40-1 and CB40-2.
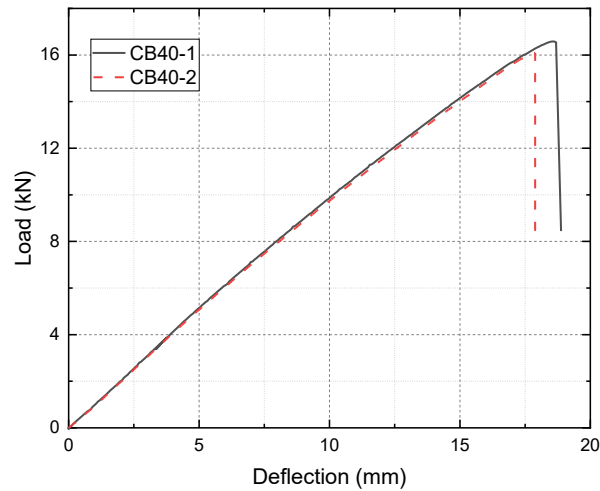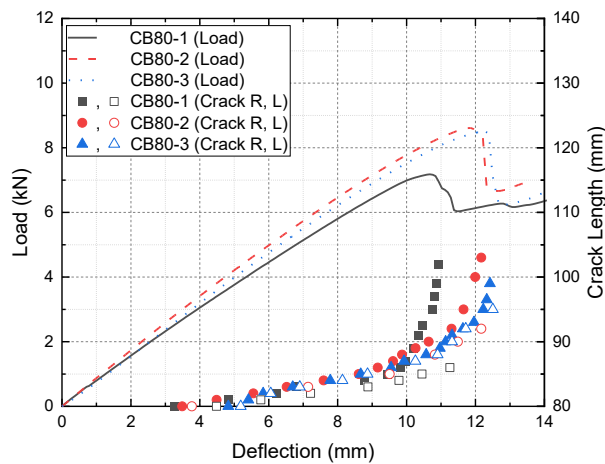

Fig. C.11. Load and crack length vs deflection curves for Specimens CB80-1, CB80-2 and CB80-3, "L" and "R" denoting crack propagation in the left and right half-spans respectively.

References

[1]   Wang C, Vassilopoulos AP, Keller T. Dataset for Mode-II delamination experiments on mid-crack beam specimens. Mendeley Data, 2023. doi: 10.17632/w28d65mwbb.1.

Curriculum Vitae

Congzhe WANG

Birth date: June 20,1993
Nationality: Chinese

E-mail: congzhe.wang@epfl.ch
Phone: +41 21 693 32 18

Website: https://www.linkedin.com/in/congzhe-wang/
                   https://people.epfl.ch/congzhe.wang?lang=en

Address:
EPFL ENAC IIC CCLAB
BP 2120 (Bâtiment BP)
Station 16
CH-1015 Lausanne
Switzerland

Doctoral assistant in Civil Engineering specializing in Composite Materials and Structures. Proficient in experimental characterization of engineering materials and data analysis. Demonstrated expertise in Finite Element Analysis through research and consultancy projects. Committed to driving progress in Advanced Structural Materials and Systems for a more sustainable future.

Education

2019 – 2023	**PhD** in Civil Engineering
	École Polytechnique Fédérale de Lausanne (EPFL), Switzerland
	Title: *Two-dimensional quasi-static delamination growth in composite laminates under Mode-I and Mode-II conditions*
	Supervisor: Prof. Thomas Keller & Anastasios P. Vassilopoulos
2015 – 2018	**MEng** in Architectural and Civil Engineering
	Tongji University, China
	Title: *Local stability and fatigue performance of pultruded GFRP bridge deck profiles*
	Supervisor: Prof. Yuqing Liu
2011 – 2015	**BEng** in Civil Engineering
	Tongji University, China

Research

2019 – 2023	Investigated the fracture behavior of composite materials as part of a SNSF (Swiss National Science Foundation) project titled "*Fatigue and fracture simulation methods for engineering structures made of polymeric composites*".

- Designed and executed novel experiments, comparing the results with standard tests.
- Conducted sophisticated nonlinear finite element analysis, incorporating novel cohesive models scripted through user subroutines.
- Collaborated with a multidisciplinary team for the development of CCFatigue, a database analysis software.

2015 – 2018	Collaborated with two fellow PhD students on an extensive project titled "*Research on key technologies of design and rapid construction of FRP composite bridges*", funded by the Ministry of Transport of the People's Republic of China.

- Executed comprehensive tests to assess the durability and mechanical properties of pultruded glass-fiber composite samples and web-flange joints.
- Carried out static and fatigue experiments on pultruded bridge-deck profiles.
- Performed nonlinear finite element analysis to evaluate the static and buckling behavior of bridge decks under wheel loads.

2016 (Summer)	Participated in a consulting project to validate and optimize the designs of two steel-concrete composite bridges.

- Established numerical models for detailed simulations of the bridges at construction and service stages, considering various load scenarios according to relevant codes.
- Optimized the bridge designs through parametric studies.

Publications

Selected journal papers:

[1] Wang C, Vassilopoulos AP, Keller T. Experimental investigation of two-dimensional Mode-II delamination in composite laminates. *Composites Part A: Applied Science and Manufacturing*. 2023; 173:107666.

[2] Wang C, Vassilopoulos AP, Keller T. Numerical modeling of two-dimensional delamination growth in composite laminates with in-plane isotropy. *Engineering Fracture Mechanics*. 2021; 250:107787.

[3] Wang C, Vassilopoulos AP, Keller T. Numerical investigation of two-dimensional Mode-II delamination growth in composite laminates. (submitted)

Teaching

2021 – 2023	**Teaching assistant**
	École Polytechnique Fédérale de Lausanne (EPFL), Switzerland

- Assisted in the master course "*Advanced Composites in Engineering Structures*" by Prof. Anastasios P. Vassilopoulos.
- Guided master projects, titled "*Design and manufacture of composite skateboards*", directed by Prof. Anastasios P. Vassilopoulos.

Training

2022 (Winter)	"*Teaching Science and Engineering*"

- Completed an online training on edX platform.

2022 (Summer)	"*Management of Innovation and Technology Transfer*"

- Completed a training program at EPFL Innovation Park, Switzerland.

Skills

- Finite Element Analysis (FEA)
- Design of Experiments (DOE)
- Data Analysis
- Mechanics
- Fracture Analysis

- Composite Materials and Structures
- Composites Manufacturing
- Structural Design and Optimization
- Computer-aided Design (CAD)
- Computer-aided Engineering (CAE)

Supplement

Conferences papers:

[1]   **Wang C**, Vassilopoulos AP, Keller T. Two-dimensional Mode-II delamination growth in composite laminates. *The 23rd International Conference on Composite Materials (ICCM 23)*. 2023; Belfast, UK.

[2]   **Wang C**, Vassilopoulos AP, Keller T. Two-dimensional Mode-II delamination growth in composite laminates with in-plane isotropy. *Proceedings of the 20th European Conference on Composite Materials (ECCM 2022): Composites Meet Sustainability*. 2022; 1: 371–378.

[3]   **Wang C**, Vassilopoulos AP, Keller T. Numerical investigation of two-dimensional Mode I crack propagation in quasi-isotropic GFRP laminates. *1st Virtual ESIS TC4 Conference on Fracture of Polymers, Composites and Adhesives*. 2021.

[4]   **Wang C**, Xin H, Zuo Y, Du A, Liu Y. Experimental study of pultruded GFRP bridge deck with double cells. *Proceedings of the 8th International Conference on Fibre-Reinforced Polymer (FRP) Composites in Civil Engineering (CICE 2016)*. 2016: 624–629.

Coauthored journal papers:

[1]   Sun Y, Liu Y, **Wang C**, Zuo Y, Xin H. Web buckling mechanism of pultruded GFRP bridge deck profiles subjected to concentrated load. *Structures*. 2021; 34: 3789–3805.

[2]   Xin H, Mosallam A, Liu Y, **Wang C**, He J. Experimental and numerical investigation on assessing local bearing behavior of a pultruded GFRP bridge deck. *Composite Structures*. 2018; 204: 712–730.

[3]   Xin H, Mosallam A, Liu Y, **Wang C**. Hygrothermal aging effects on axial behaviour of pultruded web–flange junctions and adhesively bonded build-up bridge members. *Journal of Reinforced Plastics and Composites*. 2018; 37(1): 13–34.

[4]   Xin H, Mosallam A, Liu Y, **Wang C**, Zhang Y. Impact of hygrothermal aging on rotational behavior of web-flange junctions of structural pultruded composite members for bridge applications. *Composites Part B: Engineering*. 2017; 110: 279–97.

[5]   Xin H, Mosallam A, Liu Y, **Wang C**, Zhang Y. Analytical and experimental evaluation of flexural behavior of FRP pultruded composite profiles for bridge deck structural design. *Construction and Building Materials*. 2017; 150: 123–149.

[6]   Xin H, Mosallam A, Liu Y, Xiao Y, He J, **Wang C**, Jiang Z. Experimental and numerical investigation on in-plane compression and shear performance of a pultruded GFRP composite bridge deck. *Composite Structures.* 2017; 180: 914–932.

[7]   Xin H, Liu Y, Mosallam A, Zhang Y, **Wang C**. Hygrothermal aging effects on flexural behavior of pultruded glass fiber reinforced polymer laminates in bridge applications. *Construction and Building Materials*. 2016; 127: 237–247.